Computational Study of EM Properties of Composite Materials

Xin Xu
(M.Sc., National Univ. of Singapore; B.Sc., Jilin Univ.)

A THESIS SUBMITTED
FOR THE DEGREE OF DOCTOR OF PHILOSOPHY
DEPARTMENT OF PHYSICS
NATIONAL UNIVERSITY OF SINGAPORE
2006

Acknowledgements

I would like to thank my supervisor, Associate Professor Feng Yuan Ping, who has guided and encouraged me patiently throughout the course of my work.

I would also like to thank Professor Lim Hock, who had given me the opportunity to do my Ph.D. in Temasek Laboratories.

I am greatly indebted to my colleges in Temasek Laboratories: Dr. Mattitsine for his help on measuring my samples; Mr. Gan Yeow Beng and Dr. Wang Chao-Fu for their illuminating comments and advice; Dr. Xu Yuan, Dr. Wang Xiande and Dr. Yuan Ning for their help on developing dyadic Green's functions for stratified medium; Dr. Kong Lingbing, Dr. Liu Lie, Dr. Li Zhengwen and Mr. Lin Guoqing for their help on many experimental aspects.

A special thanks goes to my project leader, Dr. Qing Anyong. I could not have finished this dissertation without his constant guidance and advice. He also taught me the Differential Evolution Strategies and his Dynamic Differential Evolution Strategies.

Contents

Summary

Efficient methods are developed to study the electromagnetic properties of composite materials with spherical, spheroidal and fiber inclusions.

Spheres and fibers have the simplest shapes and are most commonly used as inclusions for fabricating composite materials. The electromagnetic properties of composite materials can be engineered by changing the properties of the inclusions or hosts. The simulated composites with these simply shaped inclusions are good models for many real composite materials with similar but arbitrarily shaped inclusions. The study also provides a starting point for simulating composites with more complexly shaped inclusions. The work in this thesis has mainly the following contributions:

1. An approach combining T-matrix method, statistical Configurational averaging technique, and Quasi-crystalline approximation (TCQ) is formulated according to a similar one that is proposed by Varadan et al. [1]. The differential evolution strategies (DES) is successfully applied to solve the governing equation obtained with TCQ method efficiently and accurately. The method is validated using published experimental results.

2. With the combination of DES and TCQ, two propagation modes are observed numerically for composites with large, aligned spheroidal inclusions when the propagation direction is along the particle symmetry axis.

3. A novel method combining the method of moment and Monte Carlo simula-

tion with configurational averaging technique and stationary phase integral method is proposed to calculate the transmission and reflection coefficients of fiber composite material slabs. The method is experimentally validated.

Composites with spherical inclusions are studied first. TCQ method is formulated following the approach of Varadan et al. [1] with a corrected vector spherical wave translational addition theorems. The governing eigen equation, or equivalently, the dispersion equation of effective propagation constant, is derived. By defining an appropriate objective function in terms of the effective propagation constant, determination of the effective propagation constant is transformed into an optimization problem. To ensure the accuracy and efficiency of solution, DES instead of Muller's method is applied to solve the optimization problem. Good agreements between numerical and reported experimental results are obtained. The relationship between the effective wave number, volume concentration, size of the inclusion particle, are numerically studied. The existence of attenuation peak is numerically confirmed.

The TCQ model and the DES algorithm is further extended to study composites with spheroidal inclusions. For composite materials with aligned spheroidal inclusion, different anisotropy is observed for different size of inclusions. Composite materials with smaller aligned spheroidal inclusion particles behave like an uniaxial material. When the inclusion particles are larger, the composite materials have two separate propagation modes even if the wave propagates along the particle symmetry axis. In addition, both modes are propagation direc-

tion dependent and their dependency looks similar. This agrees well with the propagation characteristics of plane waves in a general nonmagnetic anisotropic material. The anisotropic properties disappear if the spheroidal inclusions are randomly oriented. It is also noticed that the composite materials with larger aligned inclusion particles are effectively quite lossy.

A numerical method is proposed to calculate the transmission and reflection coefficients of fiber composite material slabs. It combines the method of moment and Monte Carlo simulation with configurational averaging technique and stationary phase integral method. Results for composite materials with low concentration of small spherical inclusions agree well with that by the Maxwell-Garnett theory. The properties of fiber composite materials with respect to the concentration, electrical contact and various fiber properties are studied both numerically and experimentally. Good agreements have been obtained. The experimental and numerical results may be used to validate other numerical or theoretical methods or as a guidance for composite materials design.

The methods proposed in this thesis can be used more widely to simulate composites with inclusions of similar shapes as sphere, spheroid or fiber. Hopefully, the numerical simulation can help to expedite the design process of new composite materials.

List Of Abbreviations

Abbreviation	**Details**
ASAP	antenna scatterers analysis program
DES	differential evolution strategies
EFA	effective field approximation
EFIE	electric field integral equation
EM	electromagnetic
EMT	effective medium theory
FDTD	finite difference time domain
FEM	finite element method
HC	hole correction
MoM	method of moment
MST	multiple scattering theory
NEC	numerical electromagnetics code
PY	Percus-Yevick
QCA	quasi-crystalline approximation
SC	self-consistent
SDEMT	scale dependent effective medium theory
TCQ	T-matrix method, statistical configurational averaging technique, and quasi-crystalline approximation
TEM	transverse electromagnetic
VSM	vector spectral-domain method
2D	two-dimensional
3D	Three-dimensional

List of Figures

List of Tables

List Of Publications

Journal Papers

1. **X. Xu**, A. Qing, Y. B. Gan, and Y. P. Feng, An Experimental Study on Electromagnetic properties of Random Fiber Composite Materials, *Microwave Opt. Technol. Lett.*, Vol.49, No. 1, pp185-190, Jan. 2007

2. A. Qing, **X. Xu**, and Y. B. Gan, Anisotropy of composite materials with inclusion with orientation preference, *IEEE Trans. Antennas Propagat.*, vol. 53, no. 2, pp. 737-744, 2005

3. **X. Xu**, A. Qing, Y. B. Gan, and Y. P. Feng, Effective properties of fiber composite materials, *J. Electromag. Waves Appli.*, Vol. 18, No. 5, pp649-662, 2004

4. A. Qing, **X. Xu**, and Y. B. Gan, Effective permittivity tensor of Composite Material with aligned spheroidal inclusion, *J. Electromag. Waves Appli.*, vol. 18, no. 7, pp. 899-910, 2004

5. Xian Ning Xie, Hong Jing Chung, Hai Xu, **Xin Xu**, Chorng Haur Sow, and Andrew Thye Shen Wee, Probe-Induced Native Oxide Decomposition and Localized Oxidation on 6H-SiC (0001) Surface: An Atomic Force Microscopy Investigation, *J. Am. Chem. Soc.*, 126 (24), 7665 -7675, 2004.

6. X. Wang, C. F. Wang, Y. B. Gan, **X. Xu** and L.W. Li, Computation of scattering cross section of targets situated above lossy half space, *Electro. Lett.*, Vol. 39, No. 8, pp683-684, April, 2003

7. **X. Xu**, Y. P. Feng, Excitons in coupled quantum dots, *J. Phys. Chem. Solids.,* Vol. 64, No. 11, pp. 2301-2306, Nov. 2003

8. **X. Xu**, Y. P. Feng, Quantum Confinement and Excitonic Effects in Vertically Coupled Quantum Dots, *Key Engineering Materials*, Vol. 227, pp.171-176, 2002

9. T. S. Koh, Y. P. Feng, **X. Xu** and H. N. Spector, Excitons in semiconductor quantum discs, *J. Phys. Condensed Matter.,* Vol. 13, No 7, pp.1485-1498, Feb. 2001

Conference Papers

10. **X. Xu**, A. Qing, Y. B. Gan, and Y. P. Feng, Effect of Electrical Contact in Fiber Composite Materials, *PIERS 2004*, August 28-31, 2004, Nanjing, China

11. A. Qing, Y. B. Gan, and **X. Xu**, A correction of the vector spherical wave function translational addition theorems, *PIERS 2003*, Jan. 7-10, 2003, Singapore

12. A. Qing, Y. B. Gan, and **X. Xu**, Electromagnetic scattering of two perfectly conducting spheres using T-matrix method and corrected vector spherical wave functions translational addition theorems, *PIERS 2003*, Jan. 7-10, 2003, Singapore

14. A. Qing, **X. Xu**, and Y. B. Gan, Effective wave number of composite materials with oriented randomly distributed inclusions, *2003 IEEE AP-S Int. Symp.*, June 22-27, 2003, Columbus, Ohio, vol. 4, pp. 655-658

13. **X. Xu**, A. Qing, Y. B. Gan, and Y. P. Feng, Effective parameters of fiber composite materials, *ICMAT 2003*, pp. 32-35, December 7-12, 2003, Singapore

Chapter 1

Introduction

1.1 Background

As the development of technologies, the requirements on the material properties can easily go beyond what can be obtained with the existing materials. The design of new materials becomes a critical research. One of the designing methods is to mix two or more kinds of materials together to form composite materials. A composite material generally consists of a matrix, also called host, and fillers, also known as reinforcement or inclusions. Composite materials have flexibility and manageable properties that change with their components' ratio, distribution, shape, size and intrinsic properties. The flexibility of composite material has made it a very popular choice in many applications.

In principle, the desired properties of composite materials can be achieved experimentally through trial and error laboratory synthesis and subsequent analysis. This approach is very time and money consuming so that non-optimal design is commonplace. It is very important to have a good method to analyze the experimental data and predict results for further experiments. Mathematical modeling and simulation that makes use of computational power is an ideal choice for guiding the engineering design problems. It has played a significant and complementary role to the laboratory development of composite materials. The modeling of electromagnetic (EM) properties of the composite materials is widely carried out by many researchers [5–7]. The accurate modeling of composite materials is important for not only the design of new composite materials but also the study of natural composites, such as snow and foliage, which is very important for remote sensing [8–10].

Both simplified models and direct computations have been applied to study composite materials with inclusions of simple shapes. The simplified models include the effective medium theory (EMT) and its extensions [6, 11, 12], the week and strong fluctuation theory [13–17] and multiple scattering method with quasi-crystalline approximation (QCA) [18]. These methods are simple due to their simplification in modeling the random system and the inclusion. As a result, their precision and applicability are very limited. A more precise method is the TCQ method [1]. The derivation of this method is a very complicated due to the expansion and translation operations with the vector spherical waves. The translational addition theorems used in the original derivation [1] has some errors. The solution method for the governing equation of the TCQ method also needs improvements on its efficiency and accuracy. Another method that makes use of T-matrix method is to combine it with Monte Carlo simulation [19–21]. This method can be very precise provided that the simulated system is big enough. This requirement is often difficult to be met with the current available computational resources. As long as T-matrix method is used, the simulation is limited to dealing with spherical inclusions or those with small aspect ratio. Numerical methods are more flexible in dealing with inclusions of arbitrary shape. However, the current numerical methods used to simulate composites [5, 22–26] are also facing the problem of limited computational resources. It is still a challenge to provide algorithms that can model the properties of composites precisely even with simple inclusions such as spheres and fibers, which are the commonly used inclusions.

1.2 Overview

1.2.1 Applications of Composite Materials

Composites can have high stiffness, high strength, light weight, good stability and, usually, low cost. They have been employed in many applications. The following will discuss some EM related applications.

One of its applications is EM shielding. The quality of a material for EM shielding is quantified by its shielding effectiveness which is the ratio of the received power on the opposite side of the shield when it is illuminated by electromagnetic radiation. Most of these composites consist of conductive fibers, such as metal fibers [3] and carbon fibers [2, 27–29].

Another application of composite materials is to make tunable devices. It has been demonstrated that the microwave effective permittivity of some composite materials has a strong dependence on inclusion's magnetic structure which can be changed by the external magnetic field or stress [30–32]. One particular interest of these materials is to make sensors to monitor the stress or field strength. The properties of some composites can also change with respect to other factors, such as temperature [33] and electric field strength [34].

Negative material, which is primarily in the form of composite, is a very hot topic in both theoretical and experimental research [35–40]. These composite materials, normally with periodically arranged inclusions, shows negative refraction index. It has been shown that these negative refraction index can be derived by assuming that both the permittivity and permeability are negative [36]. Many interesting phenomenon, such as phase reversal and super resolution, can be observed or expected. Now, most of the research in this area is focused on the theoretical prediction and numerical calculations. To the best knowledge of the author, negative materials with random inclusions have not been realized either theoretically or experimentally.

Many EM wave attenuators are made of composite materials [41–45]. The composite materials help to absorb the in-coming EM wave and transform the energy into heat. The quality of these materials is normally evaluated in terms of attenuation loss and bandwidth. The weight and shape are also of concern during the design process.

1.2.2 Synthesis of Composite Materials

For microwave applications, the inclusions are normally of fiber or powder form. The properties of the composite materials are mainly governed by that of the inclusions. The design of inclusions with desired properties is an interesting and difficult subject in materials science. In this thesis, only readily-made materials that are available in the market are used as inclusions. So the synthesis procedures discussed here do not involve chemical reactions. Some commonly used methods to manipulate hosts and inclusions are discussed here.

Some composites are made of very long fibers. These fibers are woven together to from a fabric like layer and sandwiched into or pasted onto other supporting panels. There may involve compressing, heating in a curing process. The layer of woven fibers is normally very dense and mostly applied for EM shielding where the microwaves are prevented from transmitting through the fiber layer. Sketches of such woven fabrics are shown in Figs. 1-1 and 1-2 for Haness Satin weave [2] and knitted weave [3], respectively. The Haness Satin weave in Fig. 1-1 is a 3×1 weave, where 3 strands are crossed over before going under 1 perpendicular strand [46]. The knitted weave in Fig. 1-2 can be produced by a knitting machine.

Composites with random fiber or powders are normally made by mechanical mixing. Both host materials, usually polymers, and inclusions are mixed together and the mixture is stirred mechanically. The composite with evenly distributed inclusions can be either shaped by poring into a mold or applied onto some surfaces by painting or spray.

In laboratory, only a small amount of samples are needed. Manual manipulation is of advantage. Most of the samples shown in this thesis are hand made.

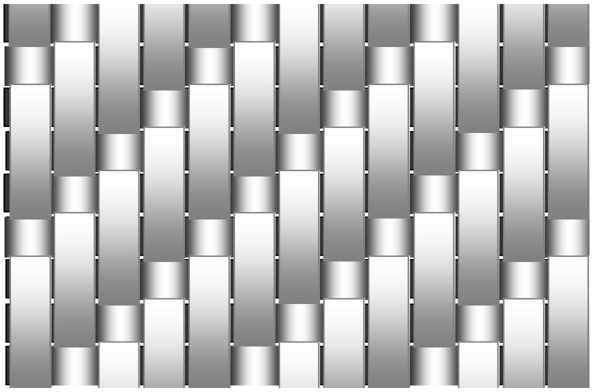

Figure 1-1: The Haness Satin weave [2].

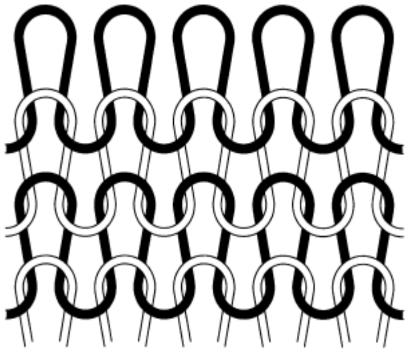

Figure 1-2: Knitted fabric used for EM shielding [3].

1.2.3 Measurement of Composite Materials

In order to measure the permittivity and permeability of a given material, a sample is placed on the path of propagating EM wave, either in free space, transmission line or a waveguide. The reflection and transmission coefficients are measured with a network analyzer. Then, the sample permittivity and permeability can be calculated from the transmission and reflection coefficients. A few commonly used measurement methods are introduced here.

Free Space Measurement

Free space measurements are the most frequently used measurement method in our study. The measurement set-up is shown in Fig. 1-3. Electromagnetic wave propagates from the transmitter into the receiver through the sample holder (which is normally made of Styrofoam) and the sample. The lenses at the opening of both antennas help to create quasi-plane-wave at the place where the sample resides. The absorber has an opening area. Most of the energy is focused in this region to illuminate the sample. The absorber absorbs EM wave from transmitter that otherwise illuminates the edge of the sample. The transmitted signal is collected by a vector network analyzer and the transmitted field strength is measured to calculate the transmission coefficients. This method allows a broad-band measurement of the complex permittivity and permeability of dielectric plates in millimeter-wave range. For experiment set-up used to measure my samples, the reflection and transmission coefficients of the device are measured between 2-18 GHz. The measurement error in transmission coefficient is about 10%, which is the relative error of the measured transmission coefficient.

Coaxial Line Method

Coaxial line method is another broad-band measurement method that is able to measure the complex permittivity and permeability of solid materials. The samples to be analyzed must be prepared in torus shape and with the right

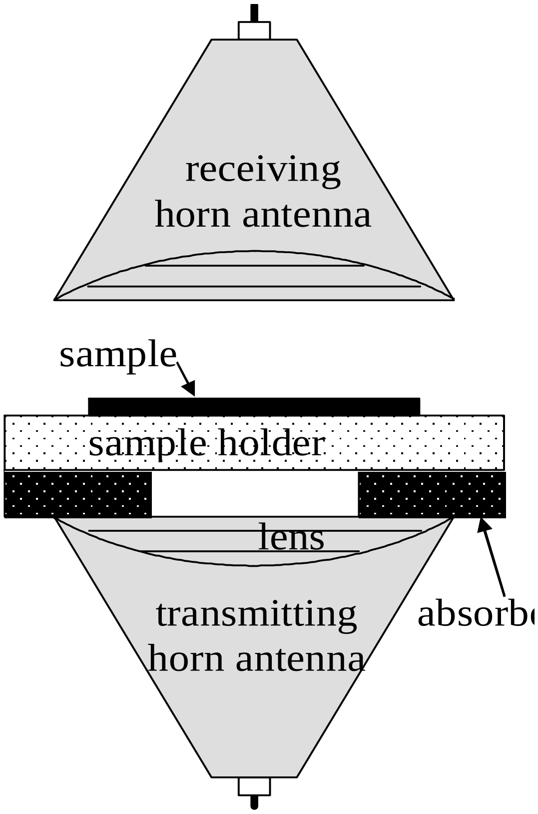

Figure 1-3: Set-up for free space measurement method.

size in order to fit well with the coaxial line as illustrated in Fig. 1-4. The electromagnetic analysis of the fixture is based on the transmission line theory: it assumes that only one TEM (transverse electromagnetic) mode is propagating along the line [47]. According to this hypothesis, the material must totally fill in the line cross section. The measurement can be carried out from a few Mega Hertz to a few Giga Hertz with an error about 5% (relative error in S parameters).

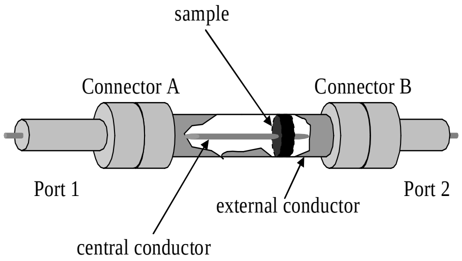

Figure 1-4: Coaxial line measurement fixture setup.

Stripline Method

Stripline method is also a broad-band measurement method. The samples to be tested are either rectangular plates or thin films. They are put (or mounted) on a dielectric holder. This method is based on the determination of the S parameters of a 3-plate transmission micro-strip line that contains the material to be tested (See Fig. 1-5). These S parameters are measured using a vector network analyzer. The method avoids the sample machining problems. This is important especially in the characterization of ferromagnetic materials. These materials are sometimes fragile and difficult to be machined. In addition, the stripline method is well suited to the characterization of rectangular and thin films [48]. This method can work in the frequency range from hundreds of kilo-Hertz up to Giga Hertz.

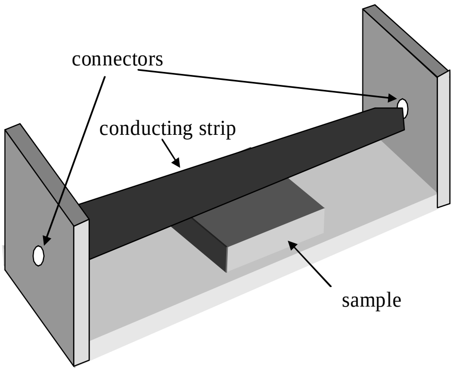

Figure 1-5: Stripline measurement fixture.

Cavity Method

There are also measurement methods that are designed to measure the properties of materials at a specific frequency. These methods make use of the resonance behavior of the fixture. The sample is used as a perturbation to the fixture so that the resonance frequency and the resonant quality factor of the fixture are different before and after the sample is inserted. One of these kinds of methods is resonant cavity method. The resonator cavity has a cylindrical shape and a circular section. The cylindrical sample is placed at the position where the field is the strongest and quasi-constant. The dielectric constant and the loss tangent are calculated from the variation of resonant frequency and the change in the cavity quality factor. Micro-strip stub method is another single-frequency resonant measurement method. It enables one to characterize solid and isotropic dielectric materials in the form of rectangular plates or thick layers.

1.2.4 Analysis of Composite Materials

Effective Medium Theory

The interaction between EM wave and matter happens in such a large range that it is impossible to be treated in a single framework. In microwave frequency range, the classical Maxwell's equations are enough to deal with most of the problems. There are two versions of Maxwell's equations. One of them describes the fundamental interactions of charged particles, such as electrons and nucleus, and propagating waves. These equations are microscopic in the sense that the response of all the charged matter to the fields is treated explicitly. These equations are too difficult to be applied to simulate materials due to the large number of particles needed to be considered. It is also unnecessary for many of the problems, including ours, to be treated from atomic level. The other version of Maxwell's equations is to define phenomenological functions, such as index of refraction or conductivity, to account for the complicated long-range interactions among vast number of particles in the atomic scale. These phenomenological functions averaged out any inhomogeneity that is in the atomic scale. These functions are also experimental quantities that can be easily measured. They have been used to characterize existing materials and newly designed materials. One of such quantities is the permittivity of a material, ε. It can be related to the microscopic quantity α_j, the polarizability of a molecule, by the well known Clausius-Mossotti [49] relation, which is expressed written as

$$\frac{\varepsilon - 1}{\varepsilon + 2} = \frac{4\pi}{3} \sum_j N_j \alpha_j. \tag{1.1}$$

If the polarizability α_j can be obtained for a molecule of a material. The permittivity (dielectric constant) of the material can be readily obtained from Eq. (1.1).

Composite materials introduce inhomogeneties in a much larger scale as compared to that in pure materials, which is in the atomic or molecule scale. However, if the component particles of a composite material can be treated as big 'molecules', Eq. (1.1) can be used to relate the effective permittivity of the composite with the polarizability of the big 'molecules'. For those big 'molecules' with spherical shape, the polarizability is [11]

$$\alpha = \left(\frac{\varepsilon_1 - 1}{\varepsilon_1 + 2} \right) a^2, \tag{1.2}$$

where ε_1 is the dielectric constant of the material in the big 'molecule' and a is its radius. Upon substituting Eq. (1.2) into Eq. (1.1), we have [11]

$$\frac{\varepsilon-1}{\varepsilon+2}=c_1\left(\frac{\varepsilon_1-1}{\varepsilon_1+2}\right), \tag{1.3}$$

where c_1 is the volume fraction of the component particles. Equation (1.3) is the first traditional static EMT, Maxwell-Garnett theory [50]. It relates the effective permittivity of the composite material with the permittivity of its component. When there are more components, Eq. (1.3) is extended by adding more terms on the right hand side for each component.

One of the shortcomings of the Maxwell-Garnett formula is that it is asymmetric upon exchanging the host and inclusions while keeping the respective volume fraction unchanged. It also fails to yield a critical threshold and cannot be generalized to multi-inclusion composite material.

Bruggeman [11] made a significant improvement to the Maxwell-Garnett theory to form a symmetrical EMT. He introduced a hypothesis that there should be zero average flux deviations due to all the inclusions. For a two-component composite material with the concentration of each component denoted by c_1 and c_2, respectively, the hypothesis can be written as

$$c_1\Delta\Phi_1+c_2\Delta\Phi_2=0, \tag{1.4}$$

where $\Delta\Phi_1$ and $\Delta\Phi_2$ are the electric flux deviation due to the inclusions embedded in a homogenous medium. The corresponding Bruggeman's EMT is

$$c_1\left(\frac{\varepsilon_1-\varepsilon}{\varepsilon_1+2\varepsilon}\right)+(1-c_1)\left(\frac{\varepsilon_2-\varepsilon}{\varepsilon_2+2\varepsilon}\right)=0 \tag{1.5}$$

Both of these theories (see Ref. [11] for a recent review) and some variations of them are primarily for static or quasi-static problems, which do not include the frequency dependence of scattering effects. Unfortunately, most problems of concern are at finite frequencies and the frequency dependence of the materials' properties are very important. Stroud and Pan [51] extended the static EMT to a Dynamic Effective Medium Theory (DEMT) by a self-consistent scheme. They have shown that the effective permittivity of a metal-dielectric composite can be obtained by

$$\langle S(\theta = 0)\rangle = 0. \tag{1.6}$$

where the angle bracket means volume average, $S(\theta = 0)$ is the forward scattering amplitude of a particle supposed to be imbedded in the effective medium and it is a function of the effective permittivity. Eq. (1.6) means that the average forward scattering amplitude vanishes if we assume that all the inclusions in the composites are embedded in the effective medium. This formulation shows that the anomalous absorption by metal-dielectric composites can be partly accounted for. Bohren and Huffman [52] pointed out that a better choice over (1.6) is

$$\langle S(\theta = 0)\rangle = \langle S(\theta = 180)\rangle = 0. \tag{1.7}$$

Equation (1.7) can be used to solve the permittivity and permeability at the same time. The resultant DEMT consists of terms accounting for the effect of frequency and radius of the scatterers, besides the term in Bruggeman EMT. Chýlek and Srivastava [12] made further extension to consider the size distribution of inclusion particle.

Scale dependent effective medium theory (SDEMT) [6] has been developed to analyze the fiber-filled composite materials. With some fitting parameters, it is shown that the percolation threshold for fiber-filled composites obtained by SDEMT is in agreement with experiments. It can also fit the experimental effective permittivity results very well [53]. However, the fitting parameters change from sample to sample. It is difficult to use SDEMT to predict the properties of composite materials.

The effective properties of composite materials have also been analyzed by other EMT like methods: EFA (Effective Field Approximation, Foldy's approximation). The above is only a brief introduction to the popular effective medium theories. For more details, please refer to the monographs by Choy [11] and Sihvola [54].

Weak and Strong Fluctuation Theory

Random media is a natural form of composite material. The scattering properties of such media, such as vegetation and snow, are very important in remote sensing. When the random fluctuating part of the medium permittivity can be assumed to be small, the weak fluctuation theory can be applied. Tatarskii [13] investigated the effects of the unbounded turbulent atmosphere in 1971. Zuniga and Kong [14] studied the active remote sensing of random media in 1980. Weak fluctuation theory fails when the permittivity fluctuation is larger or the fractional volume of scatterers is higher. The strong fluctuation theory has to be applied to overcome these difficulties. It has been used to calculate the wave scattering from volume scattering mediums [15–17].

Multiple Scattering Method

Composites with inclusions of high density and large permittivity can hardly be dealt with by either EMTs or the fluctuation theories. The scattering and multiple scattering effects is important in dense composites. The theory that considers these effects explicitly is called multiple scattering theory (MST). In MST, the excitation field of a scatterer, which sits in a collection of scatters, is the total field of the external incident field and the field scattered by all the other scatterers. After being excited by this excitation field, the scatterer also scatters a portion of field into the medium and the scattered field further acts as part of the excitation field to other scatterers. The multiply scattered field and the external incident field forms the total field that exist inside the system. The total field satisfies the boundary conditions at the interfaces between the host and inclusion. The infinite scattering hierarchy requires infinite hierarchy of equations for discrete random media.

The QCA was first introduced by Lax [18] to break the infinite hierarchy of equations that results in studies of the coherent field in discrete random media. It simply states that the conditional average of a field with the position of one scatterer held fixed is equal to the conditional average with two scatterers held fixed. The QCA has met with great success for a range of concentrations from sparse to dense and for long and intermediate wavelengths.

In QCA, the pair distribution function, which constitutes a second-order spatial correlation among the scatterers, must be specified. Common approximations for the pair distribution function are the hole correction and the Percus-Yevick (PY) pair distribution function [55]. These analytical techniques are suitable for composites with spherical inclusions. In many practical cases of interest, however, spherical inclusion is not a good model [56, 57]. More sophisticated methods that take into account of the shape anisotropy effect have to be found to calculate the proper pair correlation functions for other shapes of inclusions.

T-matrix method

T-matrix method [58, 59] is a method to calculate the scattered field due to a scatterer when the incident field is known. Using T-matrix method, Roussel et. al. [19] computed the reflection coefficient of a two-dimensional (2D) array of dielectric and magnetic fibers of arbitrary cross section. Wu and Whites [20] calculated the effective permittivity of a finite collection of 2D dielectric cylinders that are suspended in free space. Three-dimensional (3D) random scatterers have been calculated with T-matrix method combined with Monte Carlo simulation by Siqueira [21].

Numerical Method

The methods mentioned above are limited by the shape of the inclusions. They are hardly applicable to composites with inclusions that have large aspect ratios, such as disks and fibers. Numerical methods such as finite difference time domain (FDTD) method [22], finite element method (FEM) [5, 23, 24], and the method of moment (MoM) [25, 26] have been applied to simulate composite materials with non-spherical shape inclusions.

Composite materials with conductive fibers are of great practical interests, due to their unique properties. For example, high permittivity composites can be fabricated using low concentrations of fibers, and the dielectric dispersion curve can be 'shaped' by using fibers with different properties. A good introduction to the method of moment and numerical simulation of fiber (or thin wire) structures is given by Harrington [60]. Popular computer programs include ASAP (Antenna Scatterers Analysis Program) developed by Richmond [61] and NEC (Numerical Electromagnetics Code) developed by the Lawrence Livermore National Laboratory [62]. Nguyen and Maze-Mèrceur [26] used the MoM to simulate fiber composites and showed reasonable agreements with experiments and EMT theory. Liu et al. [24] used HFSS software, which is based on FEM, to study fiber filled composites. Good agreements between simulation and measurement results are presented for fiber composites with concentration less than 0.63 fibers/ cm^2 (about 250 fibers in an area of 20×20 cm^2).

1.3 Objective and Scope

This thesis investigates the EM properties of composites with spherical, spheroidal and fiber inclusions within the microwave frequency range. TCQ methods are used to simulate composites with spherical and spheroidal inclusions. Combined MoM and Monte Carlo methods are developed to deal with fiber composite materials. The numerical methods are validated with published and experimental results. The validated methods are then applied to study the relationship between effective electromagnetic properties of composites with the properties of host medium and that of the inclusion, such as the shape, size, permittivity and conductivity.

The necessary mathematical knowledge and numerical techniques are given in Chapter 2. The T-matrix method, DES and MoM are introduced.

The TCQ method is reformulated in Chapter 3. The governing eigen equation, or equivalently, the dispersion equation of effective propagation constant, is firstly derived. By defining an appropriate objective function in terms of the effective propagation constant, determination the effective propagation constant is transformed into an optimization problem. To ensure the accuracy and efficiency of solution, DES instead of Muller's method is applied to solve the optimization problem. Good agreements between numerical and published experimental results are obtained. The relationship between the effective wave number, volume concentration, size and aspect ratio of the inclusion particle, are numerically studied. The existence of attenuation peak is numerically confirmed.

The TCQ model and the DES algorithm are further applied to analyze the effective electromagnetic properties of composite materials with spheroidal inclusions in Chapter 4. Different anisotropic properties are observed for composite materials with small and large aligned spheroidal inclusion particles. While composite materials with small aligned inclusion particles behave like uniaxial material, composite materials with larger aligned inclusion particles have two separate propagation modes even if the wave propagates along the particle symmetry axis. In addition, both modes are propagation direction dependent and the dependent relationship look similar. This agrees well with the propagation characteristics of plane waves in a general nonmagnetic anisotropic material. The anisotropic properties disappear once the spheroidal inclusions are randomly oriented.

Fiber composites are considered in Chapter 5. A numerical method is proposed by combining MoM and Monte Carlo simulation with configurational averaging technique and stationary phase integral method. MoM and Monte Carlo simulation are use to calculate the configurationally averaged scattering amplitude of the inclusions. Configurational averaging technique and stationary phase integral method are used to derive the relationship between the effective transmission/reflection coefficients and the averaged scattering amplitudes for composite slabs. The properties of fiber composite materials with respect to the concentration, electrical contact and various fiber properties are studied both numerically and experimentally. Good agreements have been obtained.

Finally, the conclusions and discussion for future works are given in Chapter 6.

Chapter 2

Some Mathematical and Numerical Techniques

2.1 T-matrix Method

The T-matrix method was initially proposed by P. C. Waterman [58, 59] as a technique to compute electromagnetic scattering from single, homogeneous, arbitrary shaped dielectric/perfectly conducting scatterer. Due to its high numerical accuracy and efficiency, the T-matrix method is one of the most powerful and widely used tools for rigorously computing this class of electromagnetic scattering problems and has been widely used in many practical applications [8].

The basic idea of the T-matrix method is to expand the incident field, the internal field (or equivalently, the surface currents), and the scattered field using vector spherical wave functions. The scattered field expansion coefficients and the incident field expansion coefficients are related by the transition matrix, i.e., the T-matrix. The scattering problem is solved in two successive steps. In the first step, the scattered field expansion coefficients are obtained from the incident field expansion coefficients through the T-matrix. In the second step, the scattered field and other subsequent quantities, such as the bi-static scattering cross section, are calculated using the known scattered field expansion coefficients.

Waterman developed the T-matrix method based on the Huygens principles [63] (or extended boundary condition, Schelkunoff equivalent current method, Ewald-Oseen extinction theorem, and null-field method). In addition, in the traditional formulation of T-matrix, dielectric and perfectly conducting scatterers are dealt with separately, and therefore the relation between them is not well-established.

Here, an alternative formulation of the T-matrix method which is based on the electromagnetic equivalence principle [64, 65] is presented. The equivalence principle applies to both dielectric and perfectly conducting body. With the formulation for dielectric body, it is shown in the following sections that the formulation for ferfectly conducting body is a natural simplification of what is obtained for dielectric body. The present formulation is found to be more natural, and more importantly, the relationship between the T-matrix for dielectric body and that for perfectly conducting body appears to be more intuitive.

Figure 2-1 depicts a homogeneous dielectric particle embedded in (infinite) host medium with permittivity $\varepsilon_h = \varepsilon_0\varepsilon_{hr}$ and permeability $\mu_h = \mu_0\mu_{hr}$. The permittivity and permeability of the particle are $\varepsilon_p = \varepsilon_0\varepsilon_{pr}$ and $\mu_p = \mu_0\mu_{pr}$, respectively. The surface S of the particle is assumed to be piecewise continuous and is represented by a local shape function $F(\theta,\phi)$. The whole space is divided into two regions by the particle surface, region I outside S and region II inside S.

2.1.1 T-matrix for General Scatterer

According to electromagnetic equivalence theory [64, 65], we have

$$\mathbf{E}^{inc}(\mathbf{r}) + \mathbf{E}^{s}(\mathbf{r}) = \begin{cases} \mathbf{E}_I(\mathbf{r}), & \mathbf{r} \text{ outside S} \\ 0, & \mathbf{r} \text{ inside S} \end{cases}, \tag{2.1}$$

$$\mathbf{H}^{inc}(\mathbf{r}) + \mathbf{H}^{s}(\mathbf{r}) = \begin{cases} \mathbf{H}_I(\mathbf{r}), & \mathbf{r} \text{ outside S} \\ 0, & \mathbf{r} \text{ inside S} \end{cases}, \tag{2.2}$$

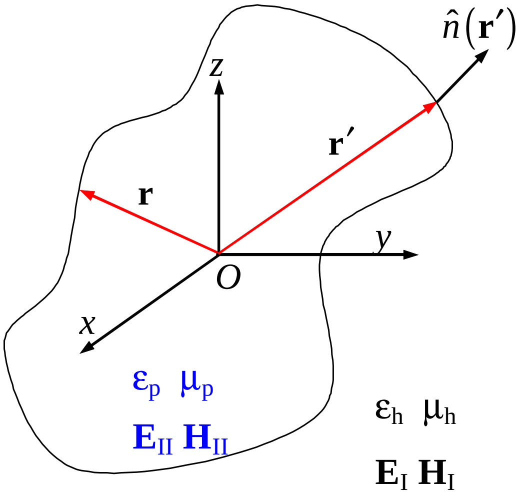

Figure 2-1: A Particle in Host Medium

where

$$\mathbf{E}^s(\mathbf{r}) = -\nabla_{\mathbf{r}} \times \mathbf{F}_h(\mathbf{r}) - \frac{1}{i\omega\varepsilon_h}\nabla_{\mathbf{r}} \times \nabla_{\mathbf{r}} \times \mathbf{A}_h(\mathbf{r}), \tag{2.3}$$

$$\mathbf{H}^s(\mathbf{r}) = \nabla_{\mathbf{r}} \times \mathbf{A}_h(\mathbf{r}) - \frac{1}{i\omega\mu_h}\nabla_{\mathbf{r}} \times \nabla_{\mathbf{r}} \times \mathbf{F}_h(\mathbf{r}), \tag{2.4}$$

$$\mathbf{A}_h(\mathbf{r}) = \iint_S \mathbf{J}_s(\mathbf{r}')\, G_h(\mathbf{r},\mathbf{r}')\, d\mathbf{r}', \tag{2.5}$$

$$\mathbf{F}_h(\mathbf{r}) = \iint_S \mathbf{M}_s(\mathbf{r}')\, G_h(\mathbf{r},\mathbf{r}')\, d\mathbf{r}', \tag{2.6}$$

$$\mathbf{J}_s(\mathbf{r}') = \hat{n}(\mathbf{r}') \times \mathbf{H}_I(\mathbf{r}') = \hat{n}(\mathbf{r}') \times \mathbf{H}_{II}(\mathbf{r}'), \tag{2.7}$$

$$\mathbf{M}_s(\mathbf{r}') = \mathbf{E}_I(\mathbf{r}') \times \hat{n}(\mathbf{r}') = \mathbf{E}_{II}(\mathbf{r}') \times \hat{n}(\mathbf{r}'), \tag{2.8}$$

$$G_h(\mathbf{r},\mathbf{r}') = \frac{\exp(ik_h|\mathbf{r}-\mathbf{r}'|)}{4\pi|\mathbf{r}-\mathbf{r}'|}, \tag{2.9}$$

$$k_h^2 = \omega^2 \varepsilon_h \mu_h. \tag{2.10}$$

The subscript h means that the quantity involved is related to the constitutive parameters of the host medium.

Now, consider a point $\mathbf{r}$ inside S. Substitute Eqs. (2.5) and (2.6) into Eq. (2.3), then substitute Eq. (2.3) into Eq. (2.1), we have

$$\begin{aligned}\mathbf{E}^{inc}(\mathbf{r}) = \; & \nabla_{\mathbf{r}} \times \iint_S \mathbf{M}_s(\mathbf{r}') \cdot \bar{\bar{\mathbf{I}}} G_h(\mathbf{r}, \mathbf{r}') \, d\mathbf{r}' \\ & + \frac{1}{i\omega\varepsilon_h} \nabla_{\mathbf{r}} \times \nabla_{\mathbf{r}} \times \iint_S \mathbf{J}_s(\mathbf{r}') \cdot \bar{\bar{\mathbf{I}}} G_h(\mathbf{r}, \mathbf{r}') \, d\mathbf{r}' \end{aligned}, \tag{2.11}$$

where $\bar{\bar{\mathbf{I}}} G_h(r, r')$ is the dyadic Green's function.

It can be shown that, if we restrict our attention to the field points $\mathbf{r}$ inside S which satisfy $r_{\min} < r'$ where r' runs over S, we have

$$\begin{aligned}\bar{\bar{\mathbf{I}}} G_h(\mathbf{r}, \mathbf{r}') = \frac{ik_h}{\pi} \sum_{n=1}^{\infty} \sum_{m=-n}^{n} \sigma_{mn} \left[\tilde{\mathbf{M}}_{mn}^I(\mathbf{r}') \, Rg\mathbf{M}_{mn}^I(\mathbf{r}) + \tilde{\mathbf{N}}_{mn}^I(\mathbf{r}') \, Rg\mathbf{N}_{mn}^I(\mathbf{r}) \right] \\ + \text{irrotational term} \end{aligned}, \tag{2.12}$$

where σ_{mn} is the normalization factor,

$$\sigma_{mn} = \frac{(2n+1)}{4n(n+1)} \frac{(n-m)!}{(n+m)!}. \tag{2.13}$$

$\mathbf{M}_{mn}^I$and $\mathbf{N}_{mn}^I$ are the outgoing vector spherical wave functions of degree n and order m in region I, with reference to the particle center, the overhead tilde $\sim$ implies complex conjugate with respect to the azimuthal component, Rg stands for regular part.

In addition, the incident field (finite at the origin) can also be expanded as,

$$\mathbf{E}^{inc}(\mathbf{r}) = \sum_{n=1}^{\infty} \sum_{m=-n}^{n} \sigma_{mn} \left[a_{mn} Rg\mathbf{M}_{mn}^I(\mathbf{r}) + b_{mn} Rg\mathbf{N}_{mn}^I(\mathbf{r}) \right], \tag{2.14}$$

where a_{mn} and b_{mn} are the incident field expansion coefficients. Substitute Eqs. (2.14) and (2.12) into Eq. (2.11) and equating the coefficients of $Rg\mathbf{M}_p^I(\mathbf{r})$ and $Rg\mathbf{N}_p^I(\mathbf{r})$ gives

$$a_{mn} = \frac{ik_h^2}{\pi} \iint\limits_S \mathbf{M}_s(\mathbf{r}') \cdot \tilde{\mathbf{N}}_{mn}^I(\mathbf{r}')\, d\mathbf{r}' + \frac{k_h^2}{\pi}\sqrt{\frac{\mu_h}{\varepsilon_h}} \iint\limits_S \mathbf{J}_s(\mathbf{r}') \cdot \tilde{\mathbf{M}}_{mn}^I(\mathbf{r}')\, d\mathbf{r}', \quad (2.15)$$

$$b_{mn} = \frac{ik_h^2}{\pi} \iint\limits_S \mathbf{M}_s(\mathbf{r}') \cdot \tilde{\mathbf{M}}_{mn}^I(\mathbf{r}')\, d\mathbf{r}' + \frac{k_h^2}{\pi}\sqrt{\frac{\mu_h}{\varepsilon_h}} \iint\limits_S \mathbf{J}_s(\mathbf{r}') \cdot \tilde{\mathbf{N}}_{mn}^I(\mathbf{r}')\, d\mathbf{r}'. \quad (2.16)$$

Substituting Eqs. (2.7) and (2.8) into Eqs. (2.15) and (2.16) leads to

$$\begin{aligned} a_{mn} = {} & \frac{ik_h^2}{\pi} \iint\limits_S \tilde{\mathbf{N}}_{mn}^I(\mathbf{r}') \times \mathbf{E}_{II}(\mathbf{r}') \cdot \hat{n}(\mathbf{r}')\, d\mathbf{r}' \qquad (2.17) \\ & + \frac{k_h^2}{\pi}\sqrt{\frac{\mu_h}{\varepsilon_h}} \iint\limits_S \mathbf{H}_{II}(\mathbf{r}') \times \tilde{\mathbf{M}}_{mn}^I(\mathbf{r}') \cdot \hat{n}(\mathbf{r}')\, d\mathbf{r}', \end{aligned}$$

$$\begin{aligned} b_{mn} = {} & \frac{ik_h^2}{\pi} \iint\limits_S \tilde{\mathbf{M}}_{mn}^I(\mathbf{r}') \times \mathbf{E}_{II}(\mathbf{r}') \cdot \hat{n}(\mathbf{r}')\, d\mathbf{r}' \qquad (2.18) \\ & + \frac{k_h^2}{\pi}\sqrt{\frac{\mu_h}{\varepsilon_h}} \iint\limits_S \mathbf{H}_{II}(\mathbf{r}') \times \tilde{\mathbf{N}}_{mn}^I(\mathbf{r}') \cdot \hat{n}(\mathbf{r}')\, d\mathbf{r}', \end{aligned}$$

where we have used the vector identity,

$$\mathbf{A} \cdot (\mathbf{B} \times \mathbf{C}) = \mathbf{B} \cdot (\mathbf{C} \times \mathbf{A}) = \mathbf{C} \cdot (\mathbf{A} \times \mathbf{B}). \quad (2.19)$$

Now, expand the internal fields (finite at particle center) as

$$\mathbf{E}_{II}\left(\mathbf{r}'\right) = \sum_{n'=1}^{\infty} \sum_{m'=-n'}^{n} c_{m'n'} Rg\mathbf{M}_{m'n'}^{II}\left(\mathbf{r}'\right) + d_{m'n'} Rg\mathbf{N}_{m'n'}^{II}\left(\mathbf{r}'\right), \tag{2.20}$$

$$\begin{aligned}\mathbf{H}_{II}\left(\mathbf{r}'\right) = & \frac{1}{i\omega\mu_p}\nabla_{\mathbf{r}'} \times \mathbf{E}_{II}\left(\mathbf{r}'\right) \\ & = -i\sqrt{\frac{\varepsilon_p}{\mu_p}} \sum_{n'=1}^{\infty} \sum_{m'=-n'}^{n'} c_{m'n'} Rg\mathbf{N}_{m'n'}^{II}\left(\mathbf{r}'\right) + d_{m'n'} Rg\mathbf{M}_{m'n'}^{II}\left(\mathbf{r}'\right)\end{aligned}, \tag{2.21}$$

where $c_{m'n'}$ and $d_{m'n'}$ are the internal field expansion coefficients. Substituting Eqs. (2.20) and (2.21) into Eqs. (2.17) and (2.18), we obtain a matrix equation

$$\begin{aligned}&\begin{bmatrix} \mathbf{a}_{mn} \\ \mathbf{b}_{mn} \end{bmatrix} \\ &= i \begin{bmatrix} \mathbf{K}_{mnm'n'} + \sqrt{\frac{\varepsilon_p\mu_h}{\varepsilon_h\mu_p}}\mathbf{J}_{mnm'n'} & \mathbf{L}_{mnm'n'} + \sqrt{\frac{\varepsilon_p\mu_h}{\varepsilon_h\mu_p}}\mathbf{I}_{mnm'n'} \\ \mathbf{I}_{mnm'n'} + \sqrt{\frac{\varepsilon_p\mu_h}{\varepsilon_h\mu_p}}\mathbf{L}_{mnm'n'} & \mathbf{J}_{mnm'n'} + \sqrt{\frac{\varepsilon_p\mu_h}{\varepsilon_h\mu_p}}\mathbf{K}_{mnm'n'} \end{bmatrix} \cdot \begin{bmatrix} \mathbf{c}_{m'n'} \\ \mathbf{d}_{m'n'} \end{bmatrix},\end{aligned} \tag{2.22}$$

where

$$\mathbf{I}_{mnm'n'} = \frac{k_h^2}{\pi} \iint_S \tilde{\mathbf{M}}_{mn}^{I}\left(\mathbf{r}'\right) \times Rg\mathbf{M}_{m'n'}^{II}\left(\mathbf{r}'\right) \cdot \hat{n}\left(\mathbf{r}'\right) d\mathbf{r}', \tag{2.23}$$

$$\mathbf{J}_{mnm'n'} = \frac{k_h^2}{\pi} \iint_S \tilde{\mathbf{M}}_{mn}^{I}\left(\mathbf{r}'\right) \times Rg\mathbf{N}_{m'n'}^{II}\left(\mathbf{r}'\right) \cdot \hat{n}\left(\mathbf{r}'\right) d\mathbf{r}', \tag{2.24}$$

$$\mathbf{K}_{mnm'n'} = \frac{k_h^2}{\pi} \iint_S \tilde{\mathbf{N}}_{mn}^{I}\left(\mathbf{r}'\right) \times Rg\mathbf{M}_{m'n'}^{II}\left(\mathbf{r}'\right) \cdot \hat{n}\left(\mathbf{r}'\right) d\mathbf{r}', \tag{2.25}$$

$$\mathbf{L}_{mnm'n'} = \frac{k_h^2}{\pi} \iint_S \tilde{\mathbf{N}}_{mn}^{I}\left(\mathbf{r}'\right) \times Rg\mathbf{N}_{m'n'}^{II}\left(\mathbf{r}'\right) \cdot \hat{n}\left(\mathbf{r}'\right) d\mathbf{r}'. \tag{2.26}$$

Consider the fields scattered by the particle,

$$\mathbf{E}^s(\mathbf{r}) = -\frac{1}{i\omega\varepsilon_h}\nabla_{\mathbf{r}}\times\nabla_{\mathbf{r}}\times\iint\limits_S \mathbf{J}_s(\mathbf{r}')\cdot\bar{\bar{\mathbf{I}}}G_h(\mathbf{r},\mathbf{r}')\,d\mathbf{r}' \\ -\nabla_{\mathbf{r}}\times\iint\limits_S \mathbf{M}_s(\mathbf{r}')\cdot\bar{\bar{\mathbf{I}}}G_h(\mathbf{r},\mathbf{r}')\,d\mathbf{r}'. \tag{2.27}$$

For the case $\mathbf{r}' < r$, we have

$$\bar{\bar{\mathbf{I}}}G_h(\mathbf{r},\mathbf{r}') = \frac{ik_h}{\pi}\sum_{n=1}^{\infty}\sum_{m=-n}^{n}\sigma_{mn}\left[Rg\tilde{\mathbf{M}}_{mn}^I(\mathbf{r}')\,\mathbf{M}_{mn}^I(\mathbf{r}) + Rg\tilde{\mathbf{N}}_{mn}^I(\mathbf{r}')\,\mathbf{N}_{mn}^I(\mathbf{r})\right] \\ +\text{irrotational term} \quad . \tag{2.28}$$

Therefore,

$$\mathbf{E}^s(\mathbf{r}) = \sum_{n=1}^{\infty}\sum_{m=-n}^{n} f_{mn}\sigma_{mn}\mathbf{M}_{mn}^I(\mathbf{r}) + g_{mn}\sigma_{mn}\mathbf{N}_{mn}^I(\mathbf{r}), \tag{2.29}$$

where f_{mn} and g_{mn} are the scattered fields expansion coefficients,

$$f_{mn} \\ = -\frac{k_h^2}{\pi}\sqrt{\frac{\mu_h}{\varepsilon_h}}\iint\limits_S \mathbf{J}_s(\mathbf{r}')\cdot Rg\tilde{\mathbf{M}}_{mn}^I(\mathbf{r}')\,d\mathbf{r}' - \frac{ik_h^2}{\pi}\iint\limits_S \mathbf{M}_s(\mathbf{r}')\cdot Rg\tilde{\mathbf{N}}_{mn}^I(\mathbf{r}')\,d\mathbf{r}', \tag{2.30}$$

$$g_{mn} \\ = -\frac{k_h^2}{\pi}\sqrt{\frac{\mu_h}{\varepsilon_h}}\iint\limits_S \mathbf{J}_s(\mathbf{r}')\cdot Rg\tilde{\mathbf{N}}_{mn}^I(\mathbf{r}')\,d\mathbf{r}' - \frac{ik_h^2}{\pi}\iint\limits_S \mathbf{M}_s(\mathbf{r}')\cdot Rg\tilde{\mathbf{M}}_{mn}^I(\mathbf{r}')\,d\mathbf{r}'. \tag{2.31}$$

In a matrix form,

$$\begin{bmatrix}\mathbf{f}_{mn}\\ \mathbf{g}_{mn}\end{bmatrix} = -\mathbf{B}\cdot\begin{bmatrix}\mathbf{c}_{m'n'}\\ \mathbf{d}_{m'n'}\end{bmatrix}, \tag{2.32}$$

where

$$\mathbf{B} = -i\begin{bmatrix} Rg\mathbf{K}_{mnm'n'} + \sqrt{\frac{\varepsilon_p\mu_h}{\varepsilon_h\mu_p}}Rg\mathbf{J}_{mnm'n'} & Rg\mathbf{L}_{mnm'n'} + \sqrt{\frac{\varepsilon_p\mu_h}{\varepsilon_h\mu_p}}Rg\mathbf{I}_{mnm'n'} \\ Rg\mathbf{I}_{mnm'n'} + \sqrt{\frac{\varepsilon_p\mu_h}{\varepsilon_h\mu_p}}Rg\mathbf{L}_{mnm'n'} & Rg\mathbf{J}_{mnm'n'} + \sqrt{\frac{\varepsilon_p\mu_h}{\varepsilon_h\mu_p}}Rg\mathbf{K}_{mnm'n'} \end{bmatrix}. \tag{2.33}$$

Now, define

$$\mathbf{A} = i\begin{bmatrix} \mathbf{K}_{mnm'n'} + \sqrt{\frac{\varepsilon_p\mu_h}{\varepsilon_h\mu_p}}\mathbf{J}_{mnm'n'} & \mathbf{L}_{mnm'n'} + \sqrt{\frac{\varepsilon_p\mu_h}{\varepsilon_h\mu_p}}\mathbf{I}_{mnm'n'} \\ \mathbf{I}_{mnm'n'} + \sqrt{\frac{\varepsilon_p\mu_h}{\varepsilon_h\mu_p}}\mathbf{L}_{mnm'n'} & \mathbf{J}_{mnm'n'} + \sqrt{\frac{\varepsilon_p\mu_h}{\varepsilon_h\mu_p}}\mathbf{K}_{mnm'n'} \end{bmatrix}, \tag{2.34}$$

Hence

$$\begin{bmatrix} \mathbf{f}_{mn} \\ \mathbf{g}_{mn} \end{bmatrix} = \mathbf{B}\cdot\begin{bmatrix} \mathbf{c}_{m'n'} \\ \mathbf{d}_{m'n'} \end{bmatrix} = \mathbf{B}\cdot\mathbf{A}^{-1}\cdot\begin{bmatrix} \mathbf{a}_{\mu\nu} \\ \mathbf{b}_{\mu\nu} \end{bmatrix} = \mathbf{T}\cdot\begin{bmatrix} \mathbf{a}_{\mu\nu} \\ \mathbf{b}_{\mu\nu} \end{bmatrix}. \tag{2.35}$$

$\mathbf{T} = \mathbf{B}\cdot\mathbf{A}^{-1}$is the desirable transition matrix, i.e., the T-matrix. A fundamental feature of the above T-matrix is that it depends only on the physical and geometrical characteristics (size, shape, permittivity, and permeability) of the particle itself, and is completely independent on the incident field, its location and orientation.

2.1.2 T-matrix for Perfect Electric Conductor

The electromagnetic equivalence principle shown in Eqs. (2.1) and (2.2) also holds for perfectly conducting particle inclusions. However, the internal electromagnetic fields, and the surface magnetic current vanish while the surface electric current exists in region I only. Therefore, for perfectly conducting inclusions, we have

$$\mathbf{E}^s(\mathbf{r}) = -\frac{1}{i\omega\varepsilon_h}\nabla\times\nabla\times\mathbf{A}_h(\mathbf{r}), \tag{2.36}$$

$$\mathbf{H}^s(\mathbf{r}) = \nabla\times\mathbf{A}_h(\mathbf{r}), \tag{2.37}$$

$$\mathbf{A}_h(\mathbf{r}) = \iint\limits_S \mathbf{J}_s(\mathbf{r}')\,G_h(\mathbf{r},\mathbf{r}')\,d\mathbf{r}', \tag{2.38}$$

$$\mathbf{J}_s(\mathbf{r}') = \hat{n}(\mathbf{r}')\times\mathbf{H}_I(\mathbf{r}'), \tag{2.39}$$

The same process can be applied to formulate the T-matrix. The unique feature here is to assume the surface electric current expansion as

$$\begin{aligned}\mathbf{J}_s(\mathbf{r}') &= \hat{n}(\mathbf{r}')\times\mathbf{H}_I(\mathbf{r}') \\ &= -i\sqrt{\frac{\varepsilon_h}{\mu_h}}\hat{n}(\mathbf{r}')\times\sum_{n'=1}^{\infty}\sum_{m'=-n'}^{n'} c_{m'n'}Rg\mathbf{N}^I_{m'n'}(\mathbf{r}') + d_{m'n'}Rg\mathbf{M}^I_{m'n'}(\mathbf{r}')\end{aligned}\ . \tag{2.40}$$

It is easy to show that the same relations exist between incident field expansion coefficients, the surface current expansion coefficients, and the scattered field expansion coefficients, while the corresponding matrices are simplified as

$$\mathbf{A} = i\begin{bmatrix}\mathbf{J}_{mnm'n'} & \mathbf{I}_{mnm'n'} \\ \mathbf{L}_{mnm'n'} & \mathbf{K}_{mnm'n'}\end{bmatrix}, \tag{2.41}$$

$$\mathbf{B} = -i\begin{bmatrix}Rg\mathbf{J}_{mnm'n'} & Rg\mathbf{I}_{mnm'n'} \\ Rg\mathbf{L}_{mnm'n'} & Rg\mathbf{K}_{mnm'n'}\end{bmatrix}. \tag{2.42}$$

2.2 Differential Evolution Strategies (DES)

DES [66] is a very simple but powerful stochastic global optimizer. It has been proven a very good global optimizer for function optimization [66, 67]. DES has been applied to electromagnetic inverse problems [67–69], composite materials

[70], antennas [71] and a lot of other mathematical and engineering fields.

Similar to the genetic algorithms, DES also operates on a population with N_{POP} individuals. Each individual is a symbolic representation of the N_{PAR} optimization parameters.

The block diagram of differential evolution strategy is shown in Fig. 2-2. After initialization, the algorithm goes into genetic evolution. Every new individual (baby), $\mathbf{y}^{n+1,i}$, where $i = 1, \cdots, N_{POP}$, is generated and selected by the three operations, namely, mutation, crossover and selection.

The mutator generates a trial vector, $\mathbf{v}^{n+1,i}$, according to the following operation:

$$(v_j)^{n+1,i} = (x_j)^{n,opt} + C_m \left[(x_j)^{n,p_1} - (x_j)^{n,p_2} \right] \qquad j = 1, \cdots, N_{PAR}, \tag{2.43}$$

where the superscript *opt* refers to the optimal individual in the nth generation. $p_1 \in [1, N_{POP}]$ and $p_2 \in [1, N_{POP}]$ are two random integer. *opt*, p_1 and p_2 should always be different from each other. The real constant C_m is the mutation intensity.

The trial vector $\mathbf{v}^{n+1,i}$ is used to mate (crossover) with the corresponding mother individual, $\mathbf{x}^{n,i}$, to give birth to a child, $\mathbf{y}^{n+1,i}$, in the following way

$$(y_j)^{n+1,i} = \begin{cases} (v_j)^{n+1,i} & \text{if } \gamma_j \leq C_c \\ (x_j)^{n,i} & \text{otherwise} \end{cases} \tag{2.44}$$

where γ_j is a real random number uniform in the range [0,1] and the real constant C_c is the probability of crossover.

In the case that no evolution happens ($\mathbf{y}^{n+1,i}$ is exactly the same as $\mathbf{x}^{n,i}$), a randomly chosen gene of the child, $\mathbf{y}^{n+1,i}$, will be replaced by the corresponding gene of the mating partner, $\mathbf{v}^{n+1,i}$.

Finally, a competition (selection) goes on between the child, $\mathbf{y}^{n+1,i}$, and its parent, $\mathbf{x}^{n,i}$. The fitter individual qualifies to be a member of the next generation. The next round of genetic evolution then begins.

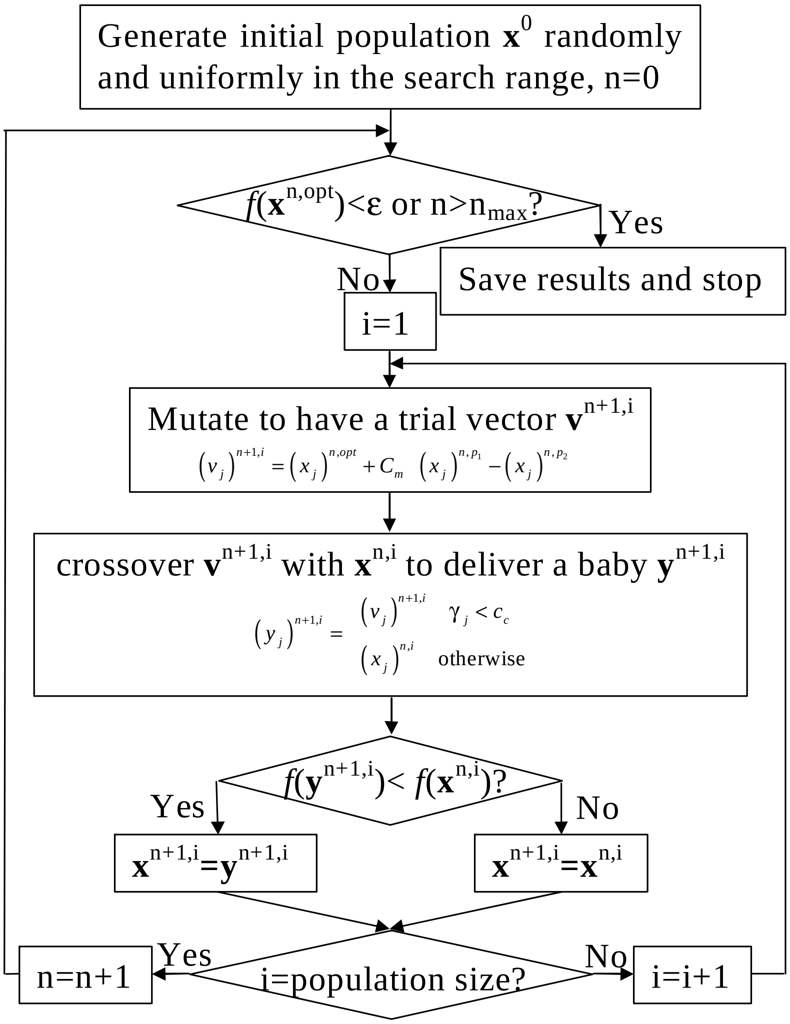

Figure 2-2: Block diagram of differential evolution strategy (ε: convergence threshold for minimization problem, γ: random number uniformly distributed in [0,1], C_m: mutation intensity, C_c: crossover probability).

In DES as shown in Fig. 2-2, the generation of the population is well defined and the population evolutes uniformly. The status of the population is updated only after the whole population evolutes to the next generation regardless of the change in population status due to the evolution of an individual. Therefore, DES responds to the population progress after a time lag. Inevitably, it results in slower convergence.

The dynamic differential evolution strategy (DDES) as shown in Fig. 2-3 inherits all of the basic genetic operators of DES, i.e., mutation, crossover, and mother-child competition. However, DDES updates the optimal individual dynamically. A mother, $\mathbf{x}^i$, will be replaced by her new-born baby, $\mathbf{y}^i$, if the new-born baby is better than her. The fitter baby will be used immediately in the following evolutions. There is also an additional competition between a new-born competitive baby and the current optimal individual. The current optimal will be replaced by the new-born competitive baby if the new-born competitive baby is better than the current optimal. The updated optimal will be used in the following evolutions immediately.

In DDES, the trial vectors are always generated using the newly updated population including the newly updated optimal individual. Consequently, DDES updates the population dynamically and responds to any improvement immediately.

As shown in Fig. 2-3, the generation indices n and $n+1$ do not show up in the evolution process of DDES. This indicates that all genetic operations are executed over individuals in the current population. There is only one population whose individuals are continuously updated by their competitive children. Although there is still a flag n representing the current generation, it is only used for the purpose of result reporting.

Apparently, only one population is needed and saved in DDES. Remember that DES need to save the parent generation while generating the child generation. Consequently, memory requirement of DDES is halved.

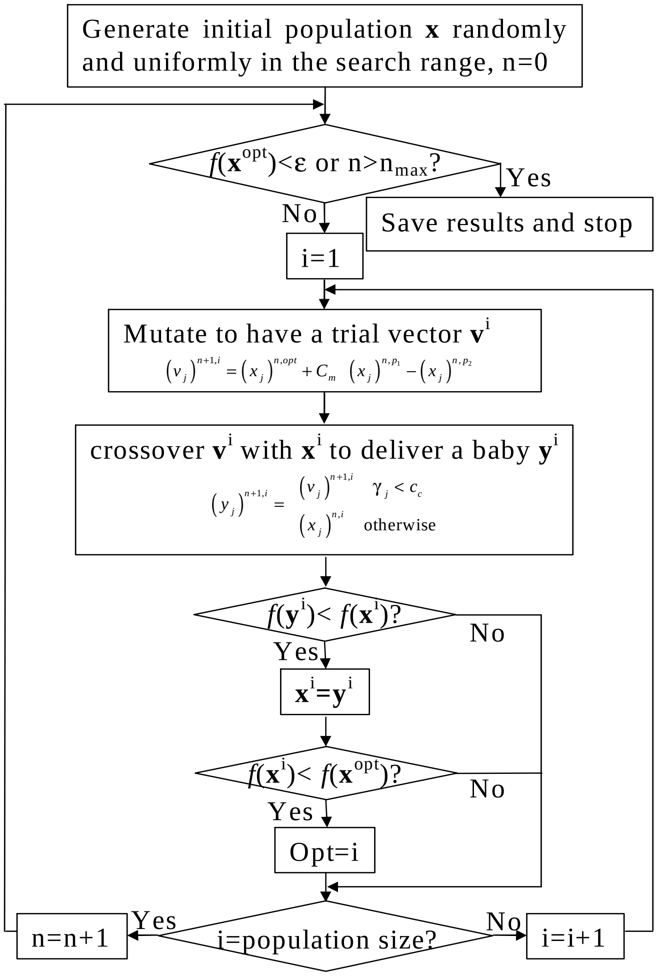

Figure 2-3: Block diagram of dynamic differential evolution strategy (ε: convergence threshold for minimization problem, γ: random number uniformly distributed in [0,1], C_m: mutation intensity, C_c: crossover probability).

2.3 Method of Moment for Thin Wires

The MoM treatment of EM scattering by thin wire structures has been described by many researchers [60, 61, 65, 72–74]. There are some MoM source codes, dealing with the problem of EM scattering by thin wire structures, available on the Internet, such as NEC [62] and ASAP [75]. We have followed some of these theories and developed our own codes in order to meet our own specific requirements. In this chapter, we will present the details of the MoM formulation used in our codes.

MoM takes the current distribution on the thin wires as unknown and solves for it. The current on a thin wire is approximated by line current flowing along its axis. Because the current distribution can normally be approximated by a few piece-wise continuous basis functions, MoM is very efficient in solving thin wire problems.

2.3.1 Integral Equation with Thin Wire Approximation

Let's assume a thin wire in free space is illuminated by a plane wave (time factor $e^{j\omega t}$ is assumed and suppressed)

$$\mathbf{E}^{inc}\left(\mathbf{r}\right) = \mathbf{E}_0 e^{-j\beta\hat{k}\cdot\mathbf{r}}, \tag{2.45}$$

where β is the propagation constant of free space, $\beta = \omega\sqrt{\varepsilon_0\mu_0}$, $\omega = 2\pi f$ is the angular frequency, $\hat{k}$ is the unit propagation vector. The scattered field at any field point $\mathbf{r}$ due to the volume current distribution $\mathbf{J}\left(\mathbf{r}'\right)$ on the wire is given by

$$\mathbf{E}^{sca}(\mathbf{r}) = -j\beta\eta_0 \int\limits_V \overline{\overline{\mathbf{G}}}\left(\mathbf{r}-\mathbf{r}'\right)\cdot\mathbf{J}\left(\mathbf{r}'\right)d\mathbf{r}', \tag{2.46}$$

where $\eta_0 = \sqrt{\mu_0/\varepsilon_0}$ is the intrinsic impedance of free space. The integral is over the volume of the wire. The free space dyadic Green's function is

$$\overline{\overline{\mathbf{G}}}\left(\mathbf{r}-\mathbf{r}'\right)=\left(\overline{\overline{\mathbf{I}}}+\frac{\nabla\nabla}{\beta^2}\right)G\left(\mathbf{r}-\mathbf{r}'\right), \tag{2.47}$$

where $G\left(\mathbf{r}-\mathbf{r}'\right)=\frac{e^{-j\beta|\mathbf{r}-\mathbf{r}'|}}{4\pi|\mathbf{r}-\mathbf{r}'|}$ is the free space Green's function.

The thin wire ($\beta a << 1$) approximation states:

- There are only axial currents in the wire. Transverse currents can be neglected.
- The currents do not depend on ϕ variation.
- The boundary condition need to be satisfied only along the wire axis.

Based on the thin wire approximation, the integral in Eq. (2.46) can be approximated by a line integral along the wire axis. It becomes

$$\mathbf{E}^{sca}(\mathbf{r})=j\beta\eta_0\int\limits_l\left(\overline{\overline{\mathbf{I}}}+\frac{\nabla\nabla}{\beta^2}\right)G\left(\mathbf{r}-\mathbf{r}'\right)\cdot\mathbf{I}\left(\mathbf{r}'\right)ds', \tag{2.48}$$

where $\mathbf{I}\left(\mathbf{r}'\right)$ is the total current along the wire axis which can be expressed as a integral of the axial current density over the cross section of the wire, s' is a parameter specifying the source point running on the wire axis.

The boundary condition for a perfect conducting wire is

$$\hat{n}\left(\mathbf{r}\right)\times\left[\mathbf{E}^{inc}\left(\mathbf{r}\right)+\mathbf{E}^{sca}\left(\mathbf{r}\right)\right]\Big|_{\text{on wire surface}}=0, \tag{2.49}$$

where $\hat{n}\left(\mathbf{r}\right)$ is the unit normal vector to the wire surface at $\mathbf{r}$. Alternatively, the boundary condition can be enforced along the direction of wire axis as

$$\hat{p}\cdot\left[\mathbf{E}^{inc}\left(\mathbf{r}\right)+\mathbf{E}^{sca}\left(\mathbf{r}\right)\right]\Big|_{\text{on wire surface}}=0, \tag{2.50}$$

where the unit vectors $\hat{p}$ is the axial direction of the wire where the field point resides. If the wire has finite conductivity, the boundary condition can be approximated by

$$\hat{p} \cdot \left[\mathbf{E}^{inc}(\mathbf{r}) + \mathbf{E}^{sca}(\mathbf{r})\right]\Big|_{\text{on wire surface}} = \hat{p} \cdot Z_S \mathbf{J}_S(\mathbf{r}), \tag{2.51}$$

where Z_S is the surface impedance of the wire and $\mathbf{J}_S$ the surface current density on the wire surface.

Electric field integral equation (EFIE) for the scattering problem can be readily obtained by substituting Eqs. (2.45) and (2.48) into Eq. (2.50) or (2.51). The result can be written as:

$$\hat{p} \cdot \left[\mathbf{E}_0 e^{-j\beta\hat{k}\cdot\mathbf{r}} - j\beta\eta_0 \int\limits_l \left(\bar{\bar{\mathbf{I}}} + \frac{\nabla\nabla}{\beta^2}\right) G(\mathbf{r}-\mathbf{r}') \cdot \mathbf{I}(\mathbf{r}')\, ds'\right] = \hat{p}\cdot Z_S \mathbf{J}_S(\mathbf{r}), \tag{2.52}$$

on wire surface, where $Z_s = 0$ for PEC wires. Equation (2.52) is also valid for multiple wires.

2.3.2 Method of Moment

MoM [60] is used to transform Eq. (2.52) into matrix equation that is solved numerically. Wires are segmented into piecewise linear segments, which conform to the original wires as much as possible (Fig. 2-4).

Each segment is called a monopole. Each pair of the adjacent monopoles forms a dipole. Each dipole has two end nodes and one terminal node. The total axial currents are approximated by a summation of weighted basis functions carried by the staggered dipoles (Fig. 2-5).

$$\mathbf{I}(s) \cong \sum_{n=1}^{N} I_n \mathbf{B}_n(s). \tag{2.53}$$

The weight I_n is the magnitude of the current at the terminal of the dipole n. The basis function $\mathbf{B}_n(s)$ is the distribution of the current on the nth dipole. We have chosen the piecewise sinusoidal function for $\mathbf{B}_n(s)$, which is given by

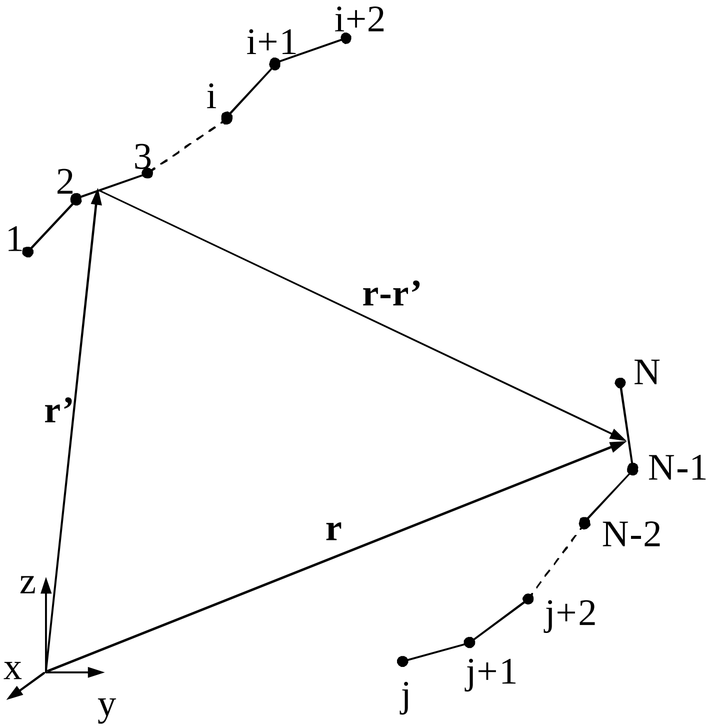

Figure 2-4: Bent wires are approximated by piece-wise linear segments.

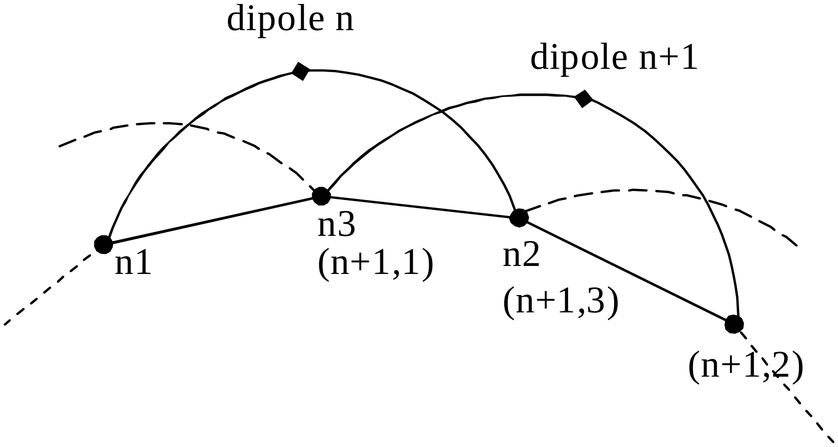

Figure 2-5: Definition of dipoles.

$$\mathbf{B}_n(s) = \begin{cases} \dfrac{\sin\beta(s - s_{n1})}{\sin\beta\Delta_{n1}}\hat{p}_{n1} & s_{n1} < s < s_{n3} \\ \dfrac{\sin\beta(s_{n2} - s)}{\sin\beta\Delta_{n2}}\hat{p}_{n2} & s_{n3} < s < s_{n2} \\ 0 & \text{otherwise} \end{cases}, \tag{2.54}$$

where $\hat{p}_{n1}$ and $\hat{p}_{n2}$ are the unit direction of the monopoles, Δ_{n1} and Δ_{n2} are the length of the monopoles, s is a local coordinate running along the dipole axis from one end s_{n1} through the terminal s_{n3} to the other end s_{n2}. Note that $n1$ and $n2$ are used to denote the nodes in s_{n1} and s_{n2}. Mean while, they are used to denote the monopoles in $\hat{p}_{n1}$, $\hat{p}_{n2}$, Δ_{n1} and Δ_{n2}. The choice of this basis function is essential to the following derivation. Our method of solving the stratified medium problem depends on the properties of this basis function.

With this current expansion, the scattered field from a wire can be written as

$$\begin{aligned} \mathbf{E}^{sca}(\mathbf{r}) &= j\beta\eta_0 \sum_{n=1}^{N} I_n \int\limits_{l_n} \left(\bar{\bar{\mathbf{I}}} + \frac{\nabla\nabla}{\beta^2}\right) G(\mathbf{r} - \mathbf{r}') \cdot \mathbf{B}_n(\mathbf{r}')\, ds' , \\ &= \sum_{n=1}^{N} I_n \mathbf{E}_n^{sca}(\mathbf{r}) \end{aligned} \tag{2.55}$$

Substituting Eq. (2.55) into Eq. (2.50) or Eq. (2.51) and using the same basis functions as testing functions, we can obtain a series of scalar equations:

$$\begin{aligned} &\sum_{n=1}^{N} I_n \int\limits_{l_m} -\mathbf{B}_m(s) \cdot \mathbf{E}_n^{sca}(\mathbf{r}) ds + \sum_{n=1}^{N} I_n \frac{Z_s}{2\pi a} \int\limits_{l_m} \mathbf{B}_m(s) \cdot \mathbf{B}_n(s)\, ds \\ &= \int\limits_{l_m} \mathbf{B}_m(s) \cdot \mathbf{E}_0 e^{-j\beta\hat{k}\cdot\mathbf{r}} ds \end{aligned} . \tag{2.56}$$

In matrix form, Eq. (2.56) is

$$\mathbf{Z} \cdot \mathbf{I} = \mathbf{V}, \tag{2.57}$$

where

$$Z_{mn} = -\int\limits_{l_m} \mathbf{B}_m\left(s\right) \cdot \mathbf{E}_n^{sca}(\mathbf{r}) ds + \frac{Z_s}{2\pi a} \int\limits_{l_m} \mathbf{B}_m\left(s\right) \cdot \mathbf{B}_n\left(s\right) ds, \tag{2.58}$$

$$V_m = \int\limits_{l_m} \mathbf{B}_m\left(s\right) \cdot \mathbf{E}_0 e^{-j\beta\hat{k}\cdot\mathbf{r}} ds. \tag{2.59}$$

Equation (2.57) can be solved numerically.

2.3.3 Scattered Field

After the electric current distribution on the wires is obtained, the scattered electric fields and other quantities can be calculated. In the far-field region, the scattered field has transverse components only. If the wave is propagating in the direction determined by the spherical coordinates (θ, ϕ), the transverse unit vector can be found as

$$\hat{u}_\phi = \frac{\hat{z} \times \hat{k}}{\left|\hat{z} \times \hat{k}\right|} = -\sin\phi\hat{x} + \cos\phi\hat{y}, \tag{2.60}$$

$$\hat{u}_\theta = \frac{\hat{u}_\phi \times \hat{k}}{\left|\hat{u}_\phi \times \hat{k}\right|} = \cos\theta\cos\phi\hat{x} + \cos\theta\sin\phi\hat{y} - \sin\theta\hat{z}. \tag{2.61}$$

Under the far-zone approximation, we have

$$\begin{aligned} \mathbf{E}_s^{sca}\left(r,\theta,\phi\right)\big|_{\,r\to\infty} &= -jk\eta_0 \sum_{n=1}^{N} \hat{p}_n I_n \int_{l_n} B_n\left(s\right) \frac{e^{-j\beta|\mathbf{r}-\mathbf{r}'|}}{4\pi\left|\mathbf{r}-\mathbf{r}'\right|} ds \\ &\cong -jk\eta_0 \frac{e^{-j\beta r}}{4\pi r} \sum_{n=1}^{N} I_n \left(\hat{p}_{n1} e^{j\beta\mathbf{r}'_{n1}\cdot\hat{r}} P_{n1}^t + \hat{p}_{n2} e^{j\beta\mathbf{r}'_{n2}\cdot\hat{r}} P_{n2}^t\right) \;, \\ &= \frac{e^{-j\beta r}}{r} C_0 A\left(\theta,\phi\right) \end{aligned} \tag{2.62}$$

where

$$P_{n1}^{t}=\int_{0}^{\Delta_{n1}}\frac{\sin\left(\beta s\right)}{\sin\left(\beta\Delta_{n1}\right)}e^{j\beta s\hat{p}_{n1}\cdot\hat{r}}ds, \tag{2.63}$$

$$P_{n2}^{t}=\int_{0}^{\Delta_{n2}}\frac{\sin\left(\beta s\right)}{\sin\left(\beta\Delta_{n2}\right)}e^{-j\beta s\hat{p}_{n2}\cdot\hat{r}}ds. \tag{2.64}$$

$$C_0=\frac{-jk\eta_0}{4\pi}, \tag{2.65}$$

$$A\left(\theta,\phi\right)=\sum_{n=1}^{N}I_n\left(\hat{p}_{n1}e^{j\beta\mathbf{r'}_{n1}\cdot\hat{r}}P_{n1}^{t}+\hat{p}_{n2}e^{j\beta\mathbf{r'}_{n2}\cdot\hat{r}}P_{n2}^{t}\right). \tag{2.66}$$

The transverse component of the fields can be obtained by projecting the vector fields onto the transverse unit vectors $\hat{u}_\phi$ and $\hat{u}_\theta$. The scattering cross section is defined as

$$\sigma\left(\theta,\phi;\theta^{inc},\phi^{inc}\right)=\lim_{r\to\infty}4\pi r^2\frac{\left|\mathbf{E}^{sca}\left(\theta,\phi\right)\right|^2}{\left|\mathbf{E}^{inc}\left(\theta^{inc},\phi^{inc}\right)\right|^2}, \tag{2.67}$$

which has an unit of area. Substituting Eq. (2.62) into Eq. (2.67) and considering unit strength incident wave, Eq. (2.67) becomes

$$\sigma\left(\theta,\phi;\theta^{inc},\phi^{inc}\right)=4\pi\left|C_0A\left(\theta,\phi\right)\right|^2. \tag{2.68}$$

In dB format

$$\sigma_{dB}\left(\theta,\phi;\theta^{inc},\phi^{inc}\right)=10\log\left[4\pi\left|C_0A\left(\theta,\phi\right)\right|^2\right]. \tag{2.69}$$

2.3.4 Surface Impedance of a Wire

The surface impedance of a finite length wire is to be approximated by that of a infinite length wire with the same material and radius [72]. Let the conductivity and dielectric constant of the wire be σ and ε_w, respectively. The total current density within the wire is the sum of the conduction current and the displacement current

$$\mathbf{J} = \sigma \mathbf{E} + j\omega \left(\varepsilon_w - \varepsilon_0\right) \mathbf{E} = j\omega \left(\varepsilon_w + \frac{\sigma}{j\omega} - \varepsilon_0\right) \mathbf{E}. \tag{2.70}$$

On the other hand, we can also think that the wire has a complex dielectric constant $\varepsilon_w' = \varepsilon_w + \dfrac{\sigma}{j\omega}$ and the current is totally displacement current. The electric field in the wire with dielectric constant ε_w' satisfies

$$\nabla \times \nabla \times \mathbf{E} + \beta_w^2 \mathbf{E} = 0, \tag{2.71}$$

where $\beta_w = \omega\sqrt{\varepsilon_w' \mu_0}$ is the propagation constant within the wire. Substitute Eq. (2.70) into Eq. (2.71), we have

$$\nabla \times \nabla \times \mathbf{J} + \beta_w^2 \mathbf{J} = 0. \tag{2.72}$$

In the thin infinite wire, $\mathbf{J}$ has, approximately, only axial component J_p and varies only with ρ. Equation (2.72) is reduced to

$$\frac{1}{\rho}\frac{\partial}{\partial \rho}\rho J_p\left(\rho\right) + \beta_w^2 J_p\left(\rho\right) = 0. \tag{2.73}$$

The solution to Eq. (2.73) is

$$J_p\left(\rho\right) = \left. J\right|_{\rho=a} \frac{J_0\left(\beta_w \rho\right)}{J_0\left(\beta_w a\right)}, \tag{2.74}$$

where $\left. J\right|_{\rho=a}$ is the current density on the surface of the wire and $J_0\left(\cdot\right)$ is the Bessel function of order 0. By requiring the total current to be I, we have

$$\left. J\right|_{\rho=a} = \frac{\beta_w I}{2\pi a}\frac{J_0\left(\beta_w a\right)}{J_1\left(\beta_w a\right)}. \tag{2.75}$$

According to Eq. (2.70), the field on the surface of the wire is

$$E_z = \frac{\beta_w}{j\omega\left(\varepsilon_w' - \varepsilon_0\right)}\frac{J_0\left(\beta_w a\right)}{J_1\left(\beta_w a\right)}\frac{I}{2\pi a}. \tag{2.76}$$

Comparing Eq. (2.76) with the right hand side of Eq. (2.51), we have

$$Z_s = \frac{\beta_w}{j\omega\left(\varepsilon_w' - \varepsilon_0\right)} \frac{J_0\left(\beta_w a\right)}{J_1\left(\beta_w a\right)}. \tag{2.77}$$

In another form

$$Z_s = \frac{\beta_w}{\sigma} \frac{J_0\left(\beta_w a\right)}{J_1\left(\beta_w a\right)}, \tag{2.78}$$

where we have taken $\varepsilon_w = \varepsilon_0$.

2.3.5 Coated Wire

If the wire is coated by a dielectric material with complex permittivity ε_c, the volume equivalence theorem gives

$$\mathbf{J} = j\omega\left(\varepsilon_c - \varepsilon_0\right)\mathbf{E}. \tag{2.79}$$

The outer radius of the coating layer is denoted by b. If the wire is highly conductive, the electric field near the wire surface is essentially in the radial direction, and it can be approximated for the field in the coating layer if b is small enough. The radial electric field can be denoted by

$$E_\rho\left(\rho, s\right) = \frac{-\hat{\rho} I'\left(s\right)}{2\pi j\omega\varepsilon_c \rho}, \tag{2.80}$$

where $I'\left(s\right)$ is the derivative of $I\left(s\right)$ with respect to s. Substitute Eq. (2.80) into Eq. (2.79), we have

$$J_\rho\left(\rho, s\right) = -\frac{\left(\varepsilon_c - \varepsilon_0\right)\hat{\rho} I'\left(s\right)}{2\pi\rho\varepsilon_c}. \tag{2.81}$$

For an electrically coated wire, each expansion mode $B_n\left(s\right)\hat{p}$ has associated with it a shell of radial electric current J_ρ. It will contribute to the impedance matrix element by

$$\Delta Z_{mn}^e = -\int\limits_m\int 2\pi\rho J_{\rho m}\left(\rho, s\right) E_{\rho n}\left(\rho, s\right) d\rho ds \quad , \tag{2.82}$$

where

$$E_{\rho n}(\rho, s) = \frac{-\hat{\rho} B_n'(s)}{2\pi j\omega\varepsilon_0\rho}. \tag{2.83}$$

Note the different permittivity used in Eqs. (2.83) and (2.80), since the coating dielectric material has been replaced by the equivalent current. Substitute Eqs. (2.81) and (2.83) into Eq. (2.82), we have

$$\Delta Z_{mn}^e = -\frac{\eta(\varepsilon_c/\varepsilon_0 - 1)\ln(b/a)}{2\pi j\beta\varepsilon_c/\varepsilon_0} \int\limits_{l_m} B_m'(s)\, B_n'(s)\, ds. \tag{2.84}$$

Now consider a wire that is coated with a magnetic material with complex permeability μ_c. Within the coating layer, the magnetic field that caused by the total current I distributed in the wire is given by

$$H_\phi(\rho) = \frac{I\hat{\phi}}{2\pi\rho}. \tag{2.85}$$

The magnetization vector has the same direction as the magnetic field. The intensity is given by

$$M_\phi(\rho) = (\mu_c/\mu_0 - 1)\, H_\phi(\rho). \tag{2.86}$$

The magnetization vector will give rise to a magnetization current in the magnetic coating layer, whose intensity is given by

$$\mathbf{J}^m = \nabla \times \mathbf{M}. \tag{2.87}$$

Carry out the curl operation, we have

$$J_\rho = -\partial M_\phi/\partial s. \tag{2.88}$$

Making use of the Stokes' theorem, we know that the magnetization current is

$$I_z^m = \begin{cases} (\mu_c/\mu_0 - 1)\, I & \text{at } \rho = a \\ -(\mu_c/\mu_0 - 1)\, I & \text{at } \rho = b \end{cases} .$$

For a magnetically coated wire, each expansion mode $B_n(s)\,\hat{p}$ has associated with it two layers of magnetization current I_z^m. The magnetization current can only generate local field since they are in the opposite direction. It will contribute to the impedance matrix element approximately by [73, 74]

$$\Delta Z_{mn}^m = \frac{j\beta\eta\,(\mu_c/\mu_0 - 1)\ln(b/a)}{2\pi} \int\limits_{l_m} B_m(s)\, B_n(s)\, ds. \tag{2.89}$$

With Eqs. (2.84) and (2.89), Eq. (2.58) is

$$Z_{mn} = -\int\limits_{l_m} \mathrm{B}_m(s)\cdot \mathrm{E}_n^{sca}(\mathrm{r})\, ds \tag{2.90}$$

$$-\frac{\eta\,(\varepsilon_c/\varepsilon_0 - 1)\ln(b/a)}{2\pi j\beta\varepsilon_c/\varepsilon_0} \int\limits_{l_m} \mathrm{B}'_m(s)\cdot \mathrm{B}'_n(s)\, ds \tag{2.91}$$

$$+\left(\frac{j\beta\eta\,(\mu_c/\mu_0 - 1)\ln(b/a)}{2\pi} + \frac{Z_s}{2\pi a}\right) \tag{2.92}$$

$$\times \int\limits_{l_m} \mathrm{B}_m(s)\cdot \mathrm{B}_n(s)\, ds \tag{2.93}$$

2.3.6 Properties of Sinusoidal Functions

It has been shown that the sinusoidal distribution of currents is obtained on an infinitely thin perfectly conducting wire. The piecewise sinusoidal distribution of currents is also a good approximation to the real current distribution on a finite thin wire. Piecewise sinusoidal functions or its modifications are widely used as the basis functions to describe the current distribution. The favorable property of the sinusoidal current is that the field radiated by this current can be obtained analytically. The derivation of analytical field expression makes use of the fact that the sinusoidal current satisfies the differential equation

$$\frac{d^2 I(\hat{z})}{d\hat{z}^2} = -\beta^2 I(\hat{z}). \tag{2.94}$$

The field radiated by such a current filament in free space can be written as

$$\begin{aligned} &E_z(\rho, \phi, z) \\ &= \frac{1}{4\pi j\omega\varepsilon}\left[I'(z_1)\frac{e^{-j\beta r_1}}{r_1} - I'(z_2)\frac{e^{-j\beta r_2}}{r_2} + I(z_1)\frac{\partial}{\partial z}\frac{e^{-j\beta r_1}}{r_1} - I(z_2)\frac{\partial}{\partial z}\frac{e^{-j\beta r_2}}{r_2}\right]. \end{aligned} \tag{2.95}$$

$$E_\rho(\rho, \phi, z) = \frac{1}{4\pi j\omega\varepsilon\rho}\left[\begin{array}{l} I'(z_2)\, e^{-j\beta r_2}\cos\theta_2 - I'(z_1)\, e^{-j\beta r_1}\cos\theta_1 \\ +I(z_1)\left(j\beta\cos^2\theta_1 - \dfrac{\sin^2\theta_1}{r_1}\right)e^{-j\beta r_1} \\ -I(z_2)\left(j\beta\cos^2\theta_2 - \dfrac{\sin^2\theta_2}{r_2}\right)e^{-j\beta r_2} \end{array}\right]. \tag{2.96}$$

Assume a piece-wise sinusoidal distribution of current flowing on a thin dipole as given by Eq. (2.54), the coordinate are shown in Fig. 2-6.

We can write

$$B_n(s_{n1}) = B_n(s_{n2}) = 0 \tag{2.97}$$

$$B_n(s_{n3}) = 1 \tag{2.98}$$

$$B_n'(s_{n1}) = \frac{\beta}{\sin\beta\Delta_{n1}}; B_n'(s_{n2}) = \frac{-\beta}{\sin\beta\Delta_{n2}} \tag{2.99}$$

$$B_n'(s_{n3-}) = \frac{\beta\cos\beta\Delta_{n1}}{\sin\beta\Delta_{n1}}; B_n'(s_{n3+}) = -\frac{\beta\cos\beta\Delta_{n2}}{\sin\beta\Delta_{n2}} \tag{2.100}$$

Notice that with $G(r) = \dfrac{e^{-j\beta r}}{4\pi r}$ and $\dfrac{\partial}{\partial z}G(r) = (-j\beta - 1/r)\cos\theta G(r)$, the electric field at a field point $\mathbf{r}$ is given by

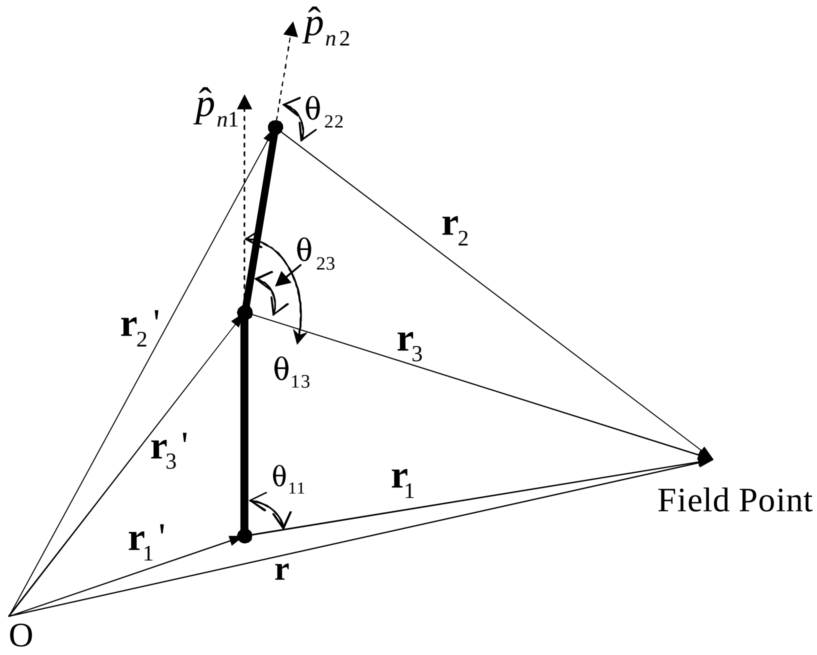

Figure 2-6: Coordinates of the nth Dipole.

$$\mathbf{E}_{\hat{p},n1} = \frac{1}{4\pi j\omega\varepsilon}\left(\frac{\beta}{\sin\beta\Delta_{n1}}\frac{e^{-j\beta r_1}}{r_1} - \left[\frac{\beta\cos\beta\Delta_{n1}}{\sin\beta\Delta_{n1}} - \left(j\beta + \frac{1}{r_3}\right)\cos\theta_{12}\right]\frac{e^{-j\beta r_3}}{r_3}\right), \tag{2.101}$$

$$\mathbf{E}_{\hat{p},n2} = \frac{1}{4\pi j\omega\varepsilon}\left(\frac{\beta}{\sin\beta\Delta_{n2}}\frac{e^{-j\beta r_2}}{r_2} - \left[\frac{\beta\cos\beta\Delta_{n2}}{\sin\beta\Delta_{n2}} + \left(j\beta + \frac{1}{r_3}\right)\cos\theta_{22}\right]\frac{e^{-j\beta r_3}}{r_3}\right), \tag{2.102}$$

$$E_{\hat{p},n1}(\rho,\phi,z) = \frac{\eta}{4\pi j\rho}\quad \begin{bmatrix} \dfrac{\cos\beta\Delta_{n1}}{\sin\beta\Delta_{n1}}e^{-j\beta r_3}\cos\theta_{12} - \dfrac{1}{\sin\beta\Delta_{n1}}e^{-j\beta r_1}\cos\theta_{11} \\ -\left(j\cos^2\theta_{12} - \dfrac{\sin^2\theta_{12}}{\beta r_3}\right)e^{-j\beta r_3} \end{bmatrix} . \tag{2.103}$$

$$E_{\hat{\rho},n2}\left(\rho,\phi,z\right)=\frac{\eta}{4\pi j\rho}\quad\left[\frac{\cos\beta\Delta_{n2}}{\sin\beta\Delta_{n2}}e^{-j\beta r_3}\cos\theta_{22}-\frac{1}{\sin\beta\Delta_{n2}}e^{-j\beta r_2}\cos\theta_{21}\right.$$
$$\left.+\left(j\cos^2\theta_{22}-\frac{\sin^2\theta_{22}}{\beta r_3}\right)e^{-j\beta r_3}\right]\quad. \tag{2.104}$$

When the dipole is straight, the field expressions can be simplified as

$$\mathbf{E}_{\hat{p}}=\frac{-30j}{\sin\beta\Delta_{n1}}\left[G\left(r_1\right)-\cos\beta\Delta_{n1}G\left(r_3\right)\right]+\frac{-30j}{\sin\beta\Delta_{n2}}\left[G\left(r_2\right)-\cos\beta\Delta_{n2}G\left(r_3\right)\right], \tag{2.105}$$

and

$$E_{\hat{\rho}}\left(\rho,\phi,z\right)=\frac{\eta}{4\pi j}\left[\frac{\cos\beta\Delta_{n1}}{\sin\beta\Delta_{n1}}G\left(r_3\right)\frac{\cos\theta_{12}}{\sin\theta_{12}}-\frac{1}{\sin\beta\Delta_{n1}}G\left(r_1\right)\frac{\cos\theta_{11}}{\sin\theta_{11}}\right]$$
$$+\frac{\eta}{4\pi j}\left[\frac{\cos\beta\Delta_{n2}}{\sin\beta\Delta_{n2}}G\left(r_3\right)\frac{\cos\theta_{22}}{\sin\theta_{22}}-\frac{1}{\sin\beta\Delta_{n2}}G\left(r_2\right)\frac{\cos\theta_{21}}{\sin\theta_{21}}\right]\quad. \tag{2.106}$$

2.3.7 Simulation Error in Resonance Frequency

During our simulation, we found that the resonance frequency of thin wires predicted by simulation is generally higher than that obtained by experiments. The error is found to be caused mainly by two sources, the finite radius effect and the none-unity permittivity of host materials.

The thin wire approximation does not consider the effect of finite wire thickness though the wire thickness does exit in the formulation. The effect of wire thickness on the EM properties of the wire had been studied by Schelkunoff and Friis [76]. They argued that there is an end effect due to a somewhat larger capacitance near the ends of the wire and the capacitance of the flat ends. This end effects effectively lengthen the wire and therefore modify the current distribution.

The effective lengthening δ can be written as two parts

$$\delta = \delta_c + \delta_f, \tag{2.107}$$

where δ_c is caused by the capacitance of the end cap of a wire and δ_f is caused by the fringing effect near the ends of the wire. The two parts can be expressed as

$$\delta_c = \frac{aZ_0}{30\pi}, \tag{2.108}$$

$$\delta_f = \frac{X}{\beta K}, \tag{2.109}$$

where

$$Z_0 = 60\left(\ln\frac{1}{\beta a} + \ln 2 - \gamma + \mathrm{Ci}\,\beta l - \frac{\sin\beta l}{\beta l}\right), \tag{2.110}$$

$$X = 60\,\mathrm{Si}\,\beta l + 30\left(2\,\mathrm{Si}\,\beta l - \mathrm{Si}\,2\beta l\right)\cos\beta l \tag{2.111}$$

$$+\,30\left\{\begin{array}{l} \mathrm{Ci}\left(2\beta l\right) - 2\,\mathrm{Ci}\left(\beta l\right) + 2\,\mathrm{Ci}\left(\beta l/2\right) \\ -\ln\left(\beta l\right) - \gamma + 3\ln 2 \end{array}\right\}\sin\beta l \tag{2.112}$$

$$K = 120\left(\ln\frac{1}{\beta a} + \ln 2 - \gamma + \mathrm{Ci}\,\beta l/2\right), \tag{2.113}$$

a and l are the radius and length of the wire, β is the propagation constant of the space where the wire is sitting in. Si, Cin and Ci are the sine and cosine integrals defined as

$$\mathrm{Si}\left(x\right) = \int_0^x \frac{\sin t}{t}dt. \tag{2.114}$$

$$\mathrm{Ci}\left(x\right) = -\int_\infty^x \frac{\cos t}{t}dt. \tag{2.115}$$

$$\mathrm{Cin}\left(x\right) = \int_0^x \frac{1-\cos t}{t}dt. \tag{2.116}$$

$$= -\,\mathrm{Ci}\left(x\right) + \ln\left(x\right) + \gamma \tag{2.117}$$

where $\gamma = 0.5772156649\cdots$ is the Euler constant. Once the effect of finite radius is taken into account, the effective fiber length becomes longer. The predicted resonance frequency will be lower. Because the current on a single wire has been approximated by linear superposition of many overlapping sinusoidal dipoles, the effect of fringing near the ends of a wire, i.e. the effect characterized by δ_f, has been considered. In the following simulation, only δ_c is considered.

Experiments and simulations are carried out to study the resonance frequency shift and to check the validity of the theoretical approximations. Two Cu fiber array samples are fabricated and sent for measurement in order to show the resonance frequency shift. The measurements are carried out by Dr. Matitsine using free-space method that is introduced earlier in this chapter. The configurations are shown in Fig. 2-7. The two arrays have the same pattern. The fibers have length 20mm and diameter 0.1mm. The difference between the two samples lies in the Styrofoam support. The Array in Fig. 2-7 (a) is sandwiched in between two 5mm solid Styrofoam boards as indicated by the gray region. This structure should represent the case that the arrays are standing in a homogeneous space with dielectric constant of Styrofoam (denoted by case A). The Array in Fig. 2-7 (b) is also sandwiched in between two 5mm Styrofoam boards but with the white regions cut off. The fibers are only supported at the center. This sample represents free-standing arrays (denoted by case B).

When case A is simulated, the whole space is assumed to be filled with Styrofoam (with a dielectric constant about $\varepsilon_{Styrofoam} = 1.05$) since the Styrofoam board used in experiments are thick. Case B is simulated with arrays in free space.

The experimental and simulation results are shown in Fig. 2-8. The effect of Styrofoam board on the resonance frequency shift is clearly shown by the two experimental results. The solid Styrofoam boards have lowered the resonance frequency by about $\sqrt{\varepsilon_{Styrofoam}}$ times, which confirms that the two samples are good representations of cases A and B. The simulation results by thin wire approximation with the finite radius effects (the dash-dot line) for the center support

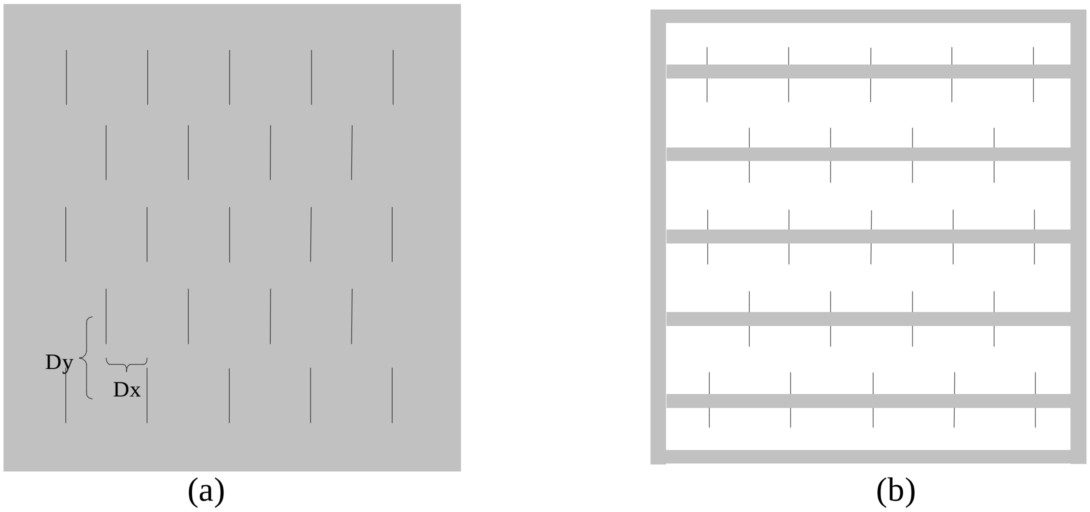

Figure 2-7: Configuration of Cu fiber arrays.

fiber array agree with experiments much better than that obtained with only thin wire approximations (the solid line). The resonance frequency difference between the two simulated results is about 1.4%.

The dot line is the simulated results by assuming the whole space is filled with Styrofoam. It is noticed that there is still some difference in the resonance frequency between the thick dashed curve and the thin dotted curve. The difference may be caused by the glue, fiber coating or the error in Styrofoam dielectric constant data.

To further check the validity of the thin wire approximation, a series of array samples as shown in Fig. 2-9 are fabricated. The elements are Cu fibers with diameter 0.1 mm. The length of the fibers varies from array to array. The fibers are secured in the tiny groves that are cut in a piece of Styrofoam board. No glue is necessary.

The experimental and simulation results are shown in Fig. 2-10 and Fig. 2-11, respectively. The simulation is carried out with the end cap effect included. They are in good agreement for all the samples.

In order to check the effect of glue, two samples were prepared for the same

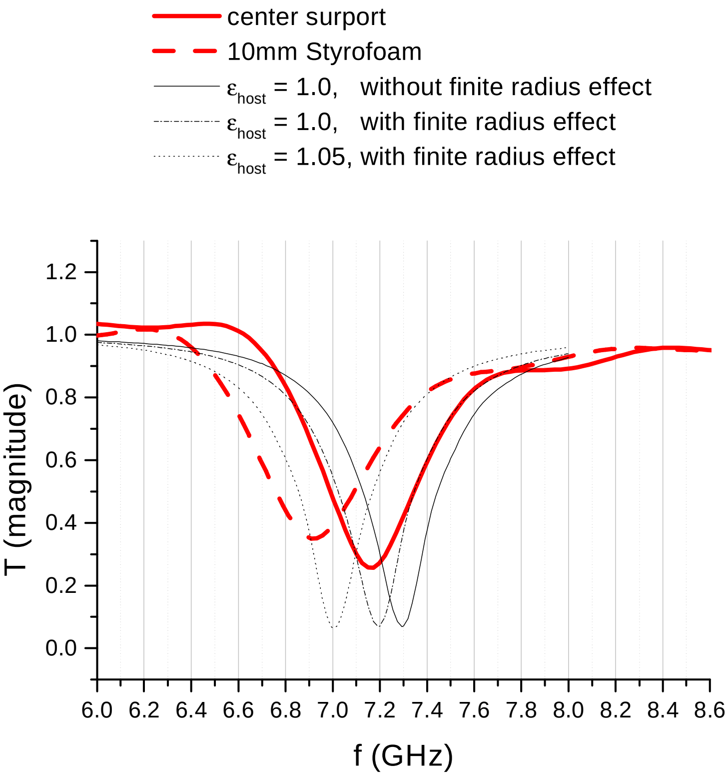

Figure 2-8: Effect of host material and finite fiber radius on the resonance frequency.

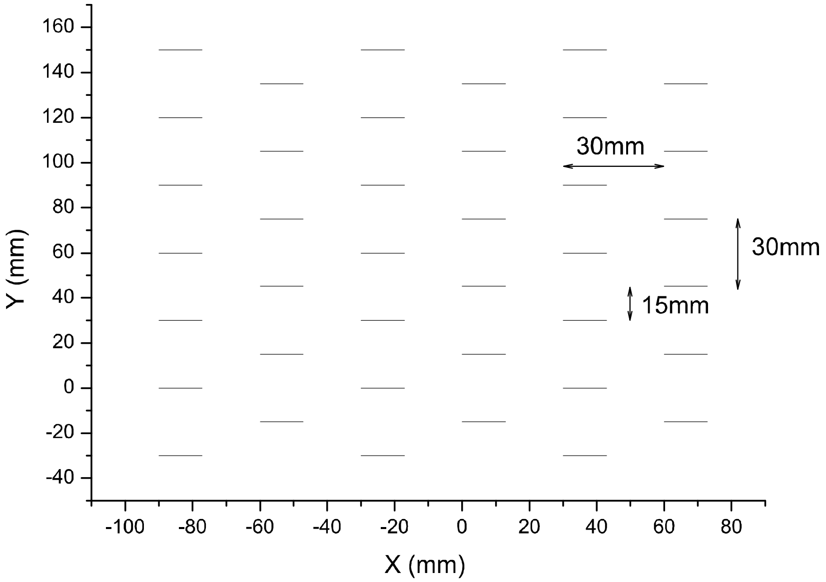

Figure 2-9: Array configuration.

array (with wire length 12.57mm). Paper glue was used in one of the samples. The results are shown in Fig. 2-11. The glue can cause a resonance frequency shift about 1%.

MoM combined with thin wire approximation is an accurate and efficient method for simulation of thin wires. In the following examples, the thin fibers are simulated by MoM with thin wire approximation. The end cap effect is always taken into account.

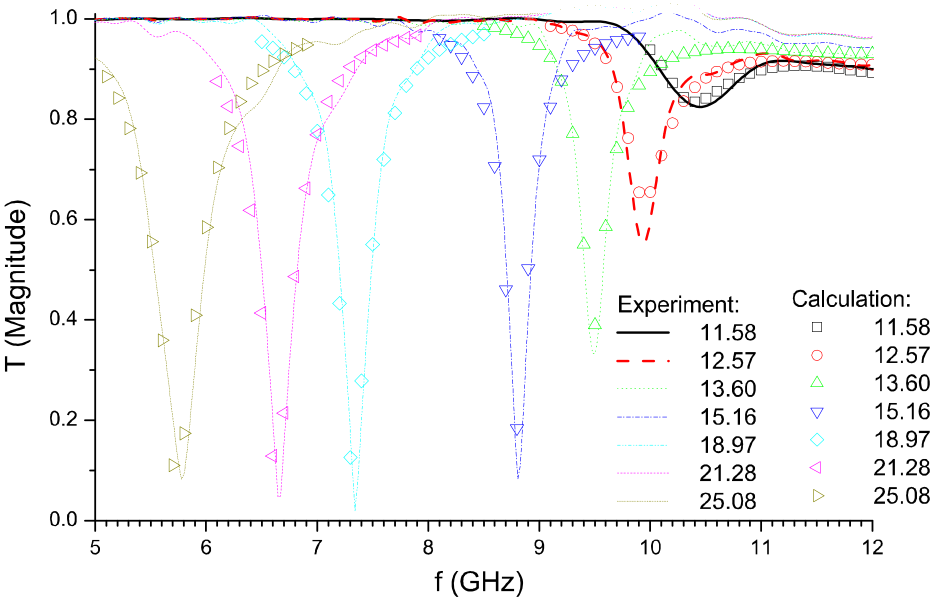

Figure 2-10: The magnitude of transmission coefficients of arrays with relatively long fibers.

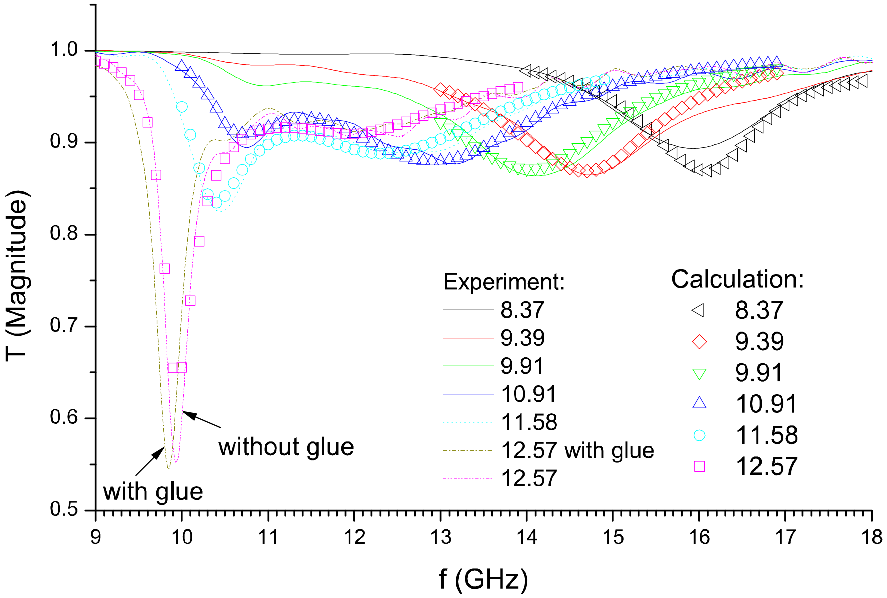

Figure 2-11: The magnitude of transmission coefficients of arrays with relatively short fibers.

Chapter 3

Composite Materials with Spherical Inclusions

The multiple scattering between inclusion particles plays a critical role when the concentration of composite material is high. The effective property of composite material under such situation is consequently quite different from that predicted by models neglecting the multiple scattering effect.

Varadan *et al.* [1] proposed the TCQ method to deal with multiple scattering of 2D elastic waves. The approach combines T-matrix method [58, 59], the statistical configurational averaging technique [77] and the quasi-crystalline approximation [18]. The T-matrix relates the scattered field expansion coefficients of a single elastic cylinder with the excitation field expansion coefficients of the same cylinder. The excitation field over a cylinder includes the incident field and the scattered fields by other cylinders that the multiple scattering between cylinders are considered. Statistical configurational averaging and Lax's quasi-crystalline approximation are applied to extract the coherent part of the scattered field. Consequently, the eigen equation for the effective wave number is obtained. This approach was later extended to three dimensional electromagnetic problems [78].

The T-matrix for a single scatterer plays a critical role in TCQ method. In the formulation of single-scatterer problems, the incident field and the scattered fields from all scatterers, except the concerned scatterer, are regarded as excitation field for the concerned scatterer. Therefore, multiple scattering between scatterers is considered. The scattered field by the concerned scatterer and its excitation field are related by the single-scatterer T-matrix. Configurational averaging technique with respect to scatterer locations can extract the coherent wave characteristics when applied to the single-scatterer scattering problem. Pair correlation functions [79] need to be used to approximate the conditional probability density for different concentration. The result is an recursion equation. Quasi-crystalline approximation is used to truncate the hierarchy enabling passage to a homogeneous continuum whose bulk propagation characteristics can then be studied.

In this chapter, the TCQ method is formulated for 3D EM wave scattering propagation problem. DES is applied to solve the governing equation. Composite materials with spherical inclusion are studied in detail. Comparison between simulation results and reported experimental results for composite materials with lossless dielectric spherical inclusion in lossless host medium has been made. Most of the numerical results are agreeable with the published experimental results. The existence of attenuation peak is numerically confirmed. The error source is analyzed. The theoretical derivation is presented in section 3.1 and 3.2. Section 3.3 shows the simulation results. Section 3.4 concludes this chapter.

3.1 Theory

3.1.1 EM Scattering from N Randomly Distributed Scatterers

Consider the composite material with randomly but uniformly located and aligned inclusion particles as shown in Fig. 3-1. No contact between inclusion particles is allowed. The host medium is characterized by its permittivity ε_h and permeability μ_h.

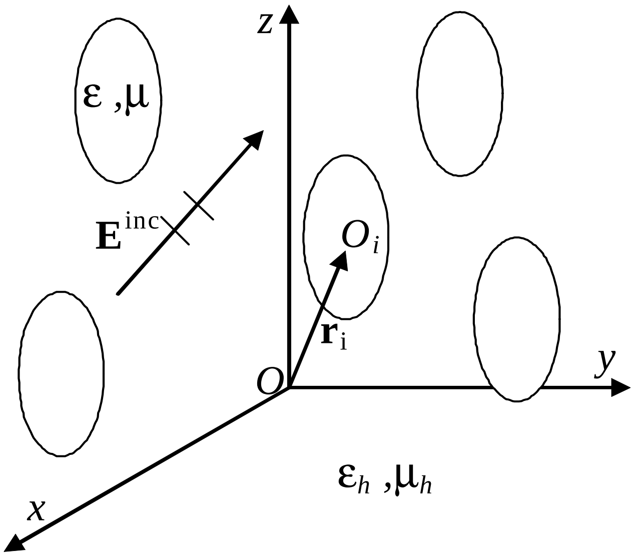

Figure 3-1: N randomly distributed scatterers

Suppose that the composite material is illuminated by a unit plane wave (time factor $e^{-i\omega t}$ is assumed and suppressed)

$$\mathbf{E}^{inc}\left(\mathbf{r}\right) = \hat{e}_0 e^{ik_h \hat{k}\cdot\mathbf{r}}, \tag{3.1}$$

where $\hat{e}_0$ is the incident field polarization, $k_h^2 = \omega^2 \mu_h \varepsilon_h$, $\hat{k}\left(\theta^{inc}, \phi^{inc}\right)$ is the unity propagation vector. The field that excites the ith particle is the sum of the incident field and the fields scattered by all other particles, i.e.,

$$\mathbf{E}_i^e(\mathbf{r}) = \mathbf{E}^{inc}(\mathbf{r}) + \sum_{j\neq i} \mathbf{E}_j^{scat}(\mathbf{r}). \tag{3.2}$$

The incident, scattered and exciting fields can be expanded in terms of vector spherical wave functions as

$$\mathbf{E}_i^{inc}(\mathbf{r}) = \sum_{n=1}^{\infty} \sum_{m=-n}^{n} a_{mn}^i Rg\mathbf{M}_{mn}^i(\mathbf{r}-\mathbf{r}_i) + b_{mn}^i Rg\mathbf{N}_{mn}^i(\mathbf{r}-\mathbf{r}_i), \tag{3.3}$$

$$\mathbf{E}_i^{scat}(\mathbf{r}) = \sum_{n=1}^{\infty} \sum_{m=-n}^{n} f_{mn}^i \mathbf{M}_{mn}^i(\mathbf{r}-\mathbf{r}_i) + g_{mn}^i \mathbf{N}_{mn}^i(\mathbf{r}-\mathbf{r}_i), \;\; |\mathbf{r}-\mathbf{r}_i| > a_i, \tag{3.4}$$

$$\mathbf{E}_i^{e}(\mathbf{r}) = \sum_{n=1}^{\infty} \sum_{m=-n}^{n} \alpha_{mn}^i Rg\mathbf{M}_{mn}^i(\mathbf{r}-\mathbf{r}_i) + \beta_{mn}^i Rg\mathbf{N}_{mn}^i(\mathbf{r}-\mathbf{r}_i), \;\; |\mathbf{r}-\mathbf{r}_i| \le a_i, \tag{3.5}$$

where $\mathbf{M}_{mn}^i(\mathbf{r}-\mathbf{r}_i)$ and $\mathbf{N}_{mn}^i(\mathbf{r}-\mathbf{r}_i)$ are vector spherical wave functions reference to O_i, the local coordination systems of the ith particle. a_i is the radius of the smallest sphere that centered at O_i and enclosing the ith scatterer. Substituting Eqs. (3.3)-(3.5) into Eq. (3.2), applying the vector spherical wave functions translational addition theorems (see Appendix B), and equating the coefficients of $Rg\mathbf{M}_{mn}^i(\mathbf{r}-\mathbf{r}_i)$ and $Rg\mathbf{N}_{mn}^i(\mathbf{r}-\mathbf{r}_i)$ give

$$\alpha_{mn}^i = a_{mn}^i + \sum_{j\neq i} \sum_{\nu=1}^{\infty} \sum_{\mu=-\nu}^{\nu} f_{\mu\nu}^j A_{mn}^{\mu\nu}(\mathbf{r}_{ji}) + g_{\mu\nu}^j B_{mn}^{\mu\nu}(\mathbf{r}_{ji}), \tag{3.6}$$

$$\beta_{mn}^i = b_{mn}^i + \sum_{j\neq i} \sum_{\nu=1}^{\infty} \sum_{\mu=-\nu}^{\nu} f_{\mu\nu}^j B_{mn}^{\mu\nu}(\mathbf{r}_{ji}) + g_{\mu\nu}^j A_{mn}^{\mu\nu}(\mathbf{r}_{ji}), \tag{3.7}$$

where $\mathbf{r}_{ji} = \mathbf{r}_i - \mathbf{r}_j$ is the translation vector from center j to center i.

$$\begin{aligned} A_{\mu\nu}^{mn}(\mathbf{r}_0) = (-1)^{\mu} \sum_p a(m,n\,|-\mu,\nu|\,p)\, a(n,\nu,p)\, h_p^{(1)}(kr_0) \\ P_p^{m-\mu}(\cos\theta_0)\, e^{i(m-\mu)\phi_0}, \end{aligned} \tag{3.8}$$

$$\begin{aligned} B_{\mu\nu}^{mn}\left(\mathbf{r}_0\right) = (-1)^{\mu+1} \sum_{p} a\left(m, n\left|-\mu, \nu\right| p, p-1\right) b\left(n, \nu, p\right) h_p^{(1)}\left(kr_0\right) \\ P_p^{m-\mu}\left(\cos\theta_0\right) e^{i(m-\mu)\phi_0}, \end{aligned} \tag{3.9}$$

where $\mathbf{r}_0 = \left(r_0, \theta_0, \phi_0\right)$ is the translation vector, $h_p^{(1)}(\cdot)$ is the first kind of spherical radial Hankel's function of order p. $P_p^q(\cdot)$ is the associated Legender's function of degree p and order q. The coefficients $a\left(m, n\left|-\mu, \nu\right| p\right)$, $a\left(m, n\left|-\mu, \nu\right| p, p-1\right)$, $a\left(n, \nu, p\right)$ and $b\left(n, \nu, p\right)$ are defined in [55, 80, 81].

In matrix form, 3.6 and 3.7 are

$$\alpha^{\iota} = \mathbf{a}^i + \sum_{j \neq i} \mathbf{V}^{ij} \cdot \mathbf{f}^j, \tag{3.10}$$

where

$$\alpha^{\iota} = \begin{bmatrix} \alpha_{mn}^i & \beta_{mn}^i \end{bmatrix}^T,$$

$$\mathbf{a}^i = \begin{bmatrix} \mathbf{a}_{mn}^i & \mathbf{b}_{mn}^i \end{bmatrix}^T,$$

$$\mathbf{V}^{ij} = \begin{bmatrix} A_{mn}^{\mu\nu}\left(\mathbf{r}_{ji}\right) & B_{mn}^{\mu\nu}\left(\mathbf{r}_{ji}\right) \\ B_{mn}^{\mu\nu}\left(\mathbf{r}_{ji}\right) & A_{mn}^{\mu\nu}\left(\mathbf{r}_{ji}\right) \end{bmatrix},$$

$$\mathbf{f}^j = \begin{bmatrix} \mathbf{f}_{\mu\nu}^i & \mathbf{g}_{\mu\nu}^i \end{bmatrix}^T,$$

$$\mathbf{f} = \begin{bmatrix} \mathbf{f}_{\mu\nu}^1 & \mathbf{g}_{\mu\nu}^1 & \cdots & \mathbf{f}_{\mu\nu}^j & \mathbf{g}_{\mu\nu}^j & \cdots & \mathbf{f}_{\mu\nu}^N & \mathbf{g}_{\mu\nu}^N \end{bmatrix}^T.$$

In addition, the scattered field expansion coefficients and the excitation field expansion coefficients are related through the T-matrix as

$$\mathbf{f}^i = \mathbf{T}^i \cdot \alpha^{\iota}, \tag{3.11}$$

Substitute Eq. (3.10) into Eq. (3.11), we have

$$\mathbf{f}^i = \mathbf{T}^i \cdot \left(\mathbf{a}^i + \sum_{j \neq i} \mathbf{V}^{ij} \cdot \mathbf{f}^j \right). \tag{3.12}$$

Equation (3.12) considers all the multiple scattering within composite materials.

3.1.2 Configurational Averaging and Quasi-crystalline Approximation

The configurational averaging is defined as [58, 78],

$$\langle f \rangle = \int\limits_V d\mathbf{r}_1 \cdots \int\limits_V d\mathbf{r}_N f\left(\mathbf{r}_1, \cdots, \mathbf{r}_N\right) p\left(\mathbf{r}_1, \cdots, \mathbf{r}_N\right), \tag{3.13}$$

where $p\left(\mathbf{r}_1, \cdots, \mathbf{r}_N\right)$ is the probability density function, $\left(\mathbf{r}_1, \cdots, \mathbf{r}_N\right)$ are the position vectors of scatterers. The conditional configurational average is defined as

$$\langle f \rangle_i = \int\limits_V d\mathbf{r}_1 \cdots \int\limits_V d\mathbf{r}_{i-1} \int\limits_V d\mathbf{r}_{i+1} \cdots \tag{3.14}$$

$$\cdots \int\limits_V d\mathbf{r}_N f\left(\mathbf{r}_1, \cdots, \mathbf{r}_N\right) p\left(\mathbf{r}_1, \cdots, \mathbf{r}_{i-1}, \mathbf{r}_{i+1}, \cdots \mathbf{r}_N \left| \mathbf{r}_i \right.\right), \tag{3.15}$$

where $p\left(\mathbf{r}_1, \cdots, \mathbf{r}_{i-1}, \mathbf{r}_{i+1}, \cdots \mathbf{r}_N \left| \mathbf{r}_i \right.\right)$ is the conditional probability density of finding the other scatterers when the ith scatterer is fixed at $\mathbf{r}_i$.

$$p\left(\mathbf{r}_1, \cdots, \mathbf{r}_N\right) = p\left(\mathbf{r}_i\right) p\left(\mathbf{r}_1, \cdots, \mathbf{r}_{i-1}, \mathbf{r}_{i+1}, \cdots \mathbf{r}_N \left| \mathbf{r}_i \right.\right). \tag{3.16}$$

$\langle f \rangle_{ij}, \langle f \rangle_{ijk}, \cdots$ are defined accordingly.

If the scatterers are randomly distributed, the positions of all scatterers are equally probable within the volume V accessible to the scatterers, and hence

$$p\left(\mathbf{r}_i\right) = \begin{cases} 1/V & \mathbf{r}_i \in V \\ 0 & \mathbf{r}_i \notin V \end{cases} . \tag{3.17}$$

In addition, the conditional probability density is written in terms of the pair-correlation function as

$$p\left(\mathbf{r}_j \left| \mathbf{r}_i \right.\right) = g\left(\mathbf{r}_{ji}\right)/V', \tag{3.18}$$

where V' is V excluding the sphere of radius $2a$ centered at $\mathbf{r}_i$.

Making Conditional averaging over Eq. (3.12), we have

$$\left\langle \mathbf{f}^i \right\rangle_i = \mathrm{T}^i \cdot \left(\mathbf{a}^i + \sum_{j \neq i} \int\limits_{V'} p\left(\mathbf{r}_j \left| \mathbf{r}_i \right.\right) \mathbf{V}^{ij} \cdot \left\langle \mathbf{f}^j \right\rangle_{ij} d\mathbf{r}_j \right) . \tag{3.19}$$

For identical scatterers, we have

$$\left\langle \mathbf{f}^i \right\rangle_i = \mathrm{T}^i \cdot \left(\mathbf{a}^i + n \int\limits_{V'} g\left(\mathbf{r}_{ji}\right) \mathbf{V}^{ij} \cdot \left\langle \mathbf{f}^j \right\rangle_{ij} d\mathbf{r}_j \right) , \tag{3.20}$$

where n is the number density of inclusion particles. The configurational average with one particle fixed has been related to that with two particles fixed. The configurational average with two particles fixed can further be related to that with three particles fixed and so on. There will be effectively infinite hierarchy of equations that are linked together.

The hierarchy in Eq. (3.20) is truncated by applying the quasi-crystalline approximation [59, 78],

$$\left\langle \mathbf{f}^j \right\rangle_{ij} = \left\langle \mathbf{f}^j \right\rangle_j . \tag{3.21}$$

Therefore

$$\left\langle \mathbf{f}^i \right\rangle_i = \mathrm{T}^i \cdot \left(\mathbf{a}^i + n \int\limits_{V'} g\left(\mathbf{r}_{ji}\right) \mathbf{V}^{ij} \cdot \left\langle \mathbf{f}^j \right\rangle_j d\mathbf{r}_j \right). \tag{3.22}$$

Equation (3.22) is the equation that involves only the conditional configurational averaged of the scatted field of a scatterer with the scatterer fixed.

3.1.3 Effective Wavenumber

Now, we consider the composite material as an effectively homogeneous dielectric medium with effective propagation vector $\mathbf{k}_e = k_e \hat{k}\left(\theta^{inc}, \phi^{inc}\right)$. The identical scatterers are assumed to be aligned. The field scattered by different scatterers at different position should only be different in a phase factor $e^{i\mathbf{k}_e \cdot \mathbf{r}_i}$. Thus, it can be assumed [78] that

$$\left\langle \mathbf{f}^i \right\rangle_i = \mathbf{Y} e^{i\mathbf{k}_e \cdot \mathbf{r}_i}, \tag{3.23}$$

where $\mathbf{Y}$ is the part of expansion coefficients that are the same for all the same scatterers. Substituting Eq. (3.23) into (3.22) leads to

$$\mathbf{Y} e^{i\mathbf{k}_e \cdot \mathbf{r}_i} = \mathrm{T}^i \cdot \left(\mathbf{a}^i + n \int\limits_{V'} g\left(\mathbf{r}_{ji}\right) \mathbf{V}^{ij} e^{i\mathbf{k}_e \cdot \mathbf{r}_j} d\mathbf{r}_j \cdot \mathbf{Y} \right). \tag{3.24}$$

Now, consider the integrals in Eq. (3.24)

$$\mathbf{I} = n \int\limits_{V'} g\left(\mathbf{r}_{ji}\right) \mathbf{V}^{ij} e^{i\mathbf{k}_e \cdot \mathbf{r}_j} d\mathbf{r}_j = e^{i\mathbf{k}_e \cdot \mathbf{r}_i} \begin{bmatrix} \left(\mathbf{I}_A\right)^{\mu\nu}_{m'n'} & \left(\mathbf{I}_B\right)^{\mu\nu}_{m'n'} \\ \left(\mathbf{I}_B\right)^{\mu\nu}_{m'n'} & \left(\mathbf{I}_A\right)^{\mu\nu}_{m'n'} \end{bmatrix}. \tag{3.25}$$

In detail, it is

$$\left(\mathbf{I}_A\right)^{\mu\nu}_{m'n'} = n \int\limits_{V'} g\left(r_{ji}\right) A^{\mu\nu}_{m'n'}\left(\mathbf{r}_{ji}\right) e^{-i\mathbf{k}_e \cdot \mathbf{r}_{ji}} d\mathbf{r}_j, \tag{3.26}$$

$$(\mathbf{I}_B)^{\mu\nu}_{m'n'} = n \int\limits_{V'} g(r_{ji})\, B^{\mu\nu}_{m'n'}(\mathbf{r}_{ji})\, e^{-i\mathbf{k}_e\cdot\mathbf{r}_{ji}} d\mathbf{r}_j. \tag{3.27}$$

Ignoring the involved constants in Eqs. (3.8) and (3.9) for the time being. They can be inserted back after the integrals are carried out. We have

$$\begin{aligned}(\mathbf{I}'_p)^{\mu\nu}_{m'n'} &= n \int\limits_{V'} g(r_{ji})\, z_p(k_h r_{ji})\, P_p^{\mu-m'}(\cos\theta_{ji})\, e^{i(\mu-m')\phi_{ji}} e^{-i\mathbf{k}_e\cdot\mathbf{r}_{ji}} d\mathbf{r}_j \\ &= (\mathbf{I}'_{1p})^{\mu\nu}_{m'n'} + (\mathbf{I}'_{2p})^{\mu\nu}_{m'n'}\end{aligned}, \tag{3.28}$$

where

$$(\mathbf{I}'_{1p})^{\mu\nu}_{m'n'} = n \int\limits_{V'} z_p(k_h r_{ji})\, P_p^{\mu-m'}(\cos\theta_{ji})\, e^{i(\mu-m')\phi_{ji}} e^{-i\mathbf{k}_e\cdot\mathbf{r}_{ji}} d\mathbf{r}_j, \tag{3.29}$$

$$(\mathbf{I}'_{2p})^{\mu\nu}_{m'n'} = n \int\limits_{V'} [g(r_{ji}) - 1]\, z_p(k_h r_{ji})\, P_p^{\mu-m'}(\cos\theta_{ji})\, e^{i(\mu-m')\phi_{ji}} e^{-i\mathbf{k}_e\cdot\mathbf{r}_{ji}} d\mathbf{r}_j. \tag{3.30}$$

Consider $(\mathbf{I}'_{1p})^{\mu\nu}_{m'n'}$ first. Noting that both $e^{-i\mathbf{k}_e\cdot\mathbf{r}_{ji}}$ and $h_p^{(1)}(k_h r_{ji})\, P_p^{\mu-m'}(\cos\theta_{ji})\, e^{i(\mu-m')\phi_{ji}}$ are solutions of scalar wave equation, we have

$$\nabla^2 e^{-i\mathbf{k}_e\cdot\mathbf{r}_{ji}} + k_e^2 e^{-i\mathbf{k}_e\cdot\mathbf{r}_{ji}} = 0, \tag{3.31}$$

$$\begin{aligned}&\nabla^2 \left[h_p^{(1)}(k_h r_{ji})\, P_p^{\mu-m'}(\cos\theta_{ji})\, e^{i(\mu-m')\phi_{ji}}\right] \\ &+ k_h^2 h_p^{(1)}(k_h r_{ji})\, P_p^{\mu-m'}(\cos\theta_{ji})\, e^{i(\mu-m')\phi_{ji}} = 0\end{aligned}. \tag{3.32}$$

Therefore

$$\left(\mathbf{I}'_{1p}\right)^{\mu\nu}_{m'n'} = \frac{n}{k_h^2 - k_e^2} \int\limits_{V'} \left\{ \begin{array}{c} z_p P_p^{\mu-m'} e^{i(\mu-m')\phi_{ji}} \nabla^2 \left(e^{-i\mathbf{k}_e\cdot\mathbf{r}_{ji}}\right) \\ -e^{-i\mathbf{k}_e\cdot\mathbf{r}_{ji}} \nabla^2 \left[z_p P_p^{\mu-m'} e^{i(\mu-m')\phi_{ji}}\right] \end{array} \right\} d\mathbf{r}_j. \tag{3.33}$$

Applying scalar Green's theorem to Eq. (3.33) gives

$$\left(\mathbf{I}'_{1p}\right)^{\mu\nu}_{m'n'} = \left(\mathbf{I}'_{\infty p}\right)^{\mu\nu}_{m'n'} + \left(\mathbf{I}'_{Sp}\right)^{\mu\nu}_{m'n'}, \tag{3.34}$$

where S is a spherical surface with radius $2a$ and

$$\left(\mathbf{I}'_{\infty p}\right)^{\mu\nu}_{m'n'} = \frac{n}{k_h^2 - k_e^2} \int\limits_{S_\infty} \left\{ \begin{array}{c} z_p P_p^{\mu-m'} e^{i(\mu-m')\phi_{ji}} \frac{\partial}{\partial n} \left(e^{-i\mathbf{k}_e\cdot\mathbf{r}_{ji}}\right) \\ -e^{-i\mathbf{k}_e\cdot\mathbf{r}_{ji}} \frac{\partial}{\partial n} \left[z_p P_p^{\mu-m'} e^{i(\mu-m')\phi_{ji}}\right] \end{array} \right\} dS, \tag{3.35}$$

$$\left(\mathbf{I}'_{Sp}\right)^{\mu\nu}_{m'n'} = \frac{-n}{k_h^2 - k_e^2} \int\limits_{S} \left\{ \begin{array}{c} z_p P_p^{\mu-m'} e^{i(\mu-m')\phi_{ji}} \frac{\partial}{\partial n} \left(e^{-i\mathbf{k}_e\cdot\mathbf{r}_{ji}}\right) \\ -e^{-i\mathbf{k}_e\cdot\mathbf{r}_{ji}} \frac{\partial}{\partial n} \left[z_p P_p^{\mu-m'} e^{i(\mu-m')\phi_{ji}}\right] \end{array} \right\} dS. \tag{3.36}$$

Using the plane wave expansion formula [81, 82]

$$e^{-i\mathbf{k}_e\cdot\mathbf{r}_{ji}} = \sum_{n=0}^{\infty} \sum_{m=-n}^{n} (-i)^n (2n+1) \frac{(n-m)!}{(n+m)!} j_n\left(k_e r_{ji}\right) \tag{3.37}$$

$$P_n^m\left(\cos\theta^{inc}\right) P_n^m\left(\cos\theta_{ji}\right) e^{im\left(\phi^{inc}-\phi_{ji}\right)}, \tag{3.38}$$

we have

$$\begin{aligned}(\mathbf{I'}_{Sp})^{\mu\nu}_{m'n'} = {} & \frac{-n}{k_h^2 - k_e^2} \sum_{n=0}^{\infty} \sum_{m=-n}^{n} (-i)^n (2n+1) \frac{(n-m)!}{(n+m)!} P_n^m (\cos\theta^{inc}) e^{im\phi^{inc}} \\ & \times (2a)^2 \left[z_p(k_h r) \frac{\partial j_n(k_e r)}{\partial r} - j_n(k_e r) \frac{\partial z_p(k_h r)}{\partial r} \right] \Bigg|_{r=2a} \qquad . \\ & \times \int_0^\pi P_n^m(\cos\theta_{ji}) P_p^{\mu-m'}(\cos\theta_{ji}) \sin\theta_{ji} d\theta_{ji} \int_0^{2\pi} e^{i(\mu-m')\phi_{ji}} e^{-im\phi_{ji}} d\phi_{ji}\end{aligned} \tag{3.39}$$

Using the orthogonality properties

$$\int_{-1}^{1} P_n^m(x) P'^m_n(x) dx = \int_0^\pi P_n^m(\cos\theta) P'^m_n(\cos\theta) \sin\theta d\theta \tag{3.40}$$

$$= \delta_{nn'} \frac{2}{2n+1} \frac{(n+m)!}{(n-m)!}, \tag{3.41}$$

$$\int_0^{2\pi} e^{im'\phi_{ji}} e^{-im\phi_{ji}} d\phi_{ji} = \delta_{mm'} 2\pi, \tag{3.42}$$

we have

$$\begin{aligned}(\mathbf{I'}_{Sp})^{\mu\nu}_{m'n'} = {} & \frac{(-i)^p}{k_h^2 - k_e^2} \frac{12\eta}{a} P_p^{\mu-m'}(\cos\theta^{inc}) e^{i(\mu-m')\phi^{inc}} \\ \times & \left\{ k_h j_p(k_e r) \frac{\partial h_p^{(1)}(k_h r)}{\partial(k_h r)} - k_e h_p^{(1)}(k_h r) \frac{\partial j_p(k_e r)}{\partial(k_e r)} \right\} \Bigg|_{r=2a} \qquad ,\end{aligned} \tag{3.43}$$

where $\eta = \frac{N}{V}\frac{4\pi a^3}{3} = c\left(\frac{a}{b}\right)^2$, c is the volume concentration. According to the extinction theorem [55,78,83], $I'_{\infty p}$ cancels with the term $\mathrm{T}^{\iota} \cdot \mathbf{a}^i$. Similar approach can be used to calculate $(\mathbf{I'}_{2p})^{\mu\nu}_{m'n'}$. The result is

$$\begin{aligned}(\mathbf{I'}_{2p})^{\mu\nu}_{m'n'} = {} & (-i)^p P_p^{\mu-m'}(\cos\theta^{inc}) e^{i(\mu-m')\phi^{inc}} 24\eta \\ & \int_1^\infty x^2 [g(x) - 1] z_p(k_h r) j_p(k_e r) dx \qquad .\end{aligned} \tag{3.44}$$

Therefore,

$$\mathbf{Y} = \mathbf{T}^i \cdot \mathbf{V'} \cdot \mathbf{Y}, \tag{3.45}$$

where

$$\mathbf{V}' = \left[\begin{array}{cc} (\mathbf{I}'_A)^{\mu\nu}_{m'n'} & (\mathbf{I}'_B)^{\mu\nu}_{m'n'} \\ (\mathbf{I}'_B)^{\mu\nu}_{m'n'} & (\mathbf{I}'_A)^{\mu\nu}_{m'n'} \end{array} \right],$$

$$\begin{aligned} (\mathbf{I}'_A)^{\mu\nu}_{m'n'} &= (-1)^{m'} \sum_p a\left(\mu, \nu \left| -m', n' \right| p\right) a\left(\nu, n', p\right) \\ &\quad \left[(\mathbf{I}'_{S'p})^{\mu\nu}_{m'n'} + (\mathbf{I}'_{2p})^{\mu\nu}_{m'n'} \right], \\ (\mathbf{I}'_B)^{\mu\nu}_{m'n'} &= (-1)^{m'+1} \sum_p a\left(\mu, \nu \left| -m', n' \right| p, p-1\right) b\left(\nu, n', p\right) \\ &\quad \left[(\mathbf{I}'_{S'p})^{\mu\nu}_{m'n'} + (\mathbf{I}'_{2p})^{\mu\nu}_{m'n'} \right]. \end{aligned}$$

3.1.4 Determination of k_e

Equation (3.45) is an infinite homogeneous system of linear equations. For a nontrivial solution of Eq. (3.45), the determinant of the truncated coefficient matrix $\mathbf{T}^i \cdot \mathbf{V}' - \mathbf{I}$ should vanish. Consequently, an objective function can be defined as

$$f\left(k_e\right) = \left| \mathbf{T}^i \cdot \mathbf{V}' - \mathbf{I} \right|. \tag{3.46}$$

However, it is numerically inconvenient to use the above objective function.

Equivalently, Eq. (3.45) implies that at least one of the eigenvalues $\lambda_n\left(\mathbf{T}^i \cdot \mathbf{V}'\right)$ of the matrix $\mathbf{T}^i \cdot \mathbf{V}'$ is 1. Alternatively, we can define a more proper objective function as

$$f\left(k_e\right) = \min_n \left| \lambda_n\left(\mathbf{T}^i \cdot \mathbf{V}'\right) - 1 \right|. \tag{3.47}$$

The Muller's complex root searching algorithm [84] has been used to determine the effective wave number of composite material with random inclusion. It is less time consuming when the number of solutions is known and a good initial guess about each solution is available. However, due to the anisotropy of some of the composite materials of interest, these conditions are difficult to be satisfied. Hence, the Muller's method is not suitable for the present problem.

The differential evolution strategy (DES) [67] is considered for the root searching process in the present problem. As a global optimizer, the DES is in general more time consuming than Muller's method. However, it requires almost nothing on the initial solution and is capable of finding all solutions easily.

3.2 Pair Correlation Functions for Hard Spheres

It has been noticed in the derivation of the TCQ model that the pair correlation function (or radial distribution function) [79] comes into the formulation when carrying out the configurational average. Numerical results show that a good approximation to the pair correlation functions is critical for dense composite materials.

In our derivation, we have restricted that there is no contact between inclusion particles. Therefore, only hard-sphere pair correlation functions are needed. There are several theories about it. Unfortunately, not all of them are suitable for application in our simulations because no explicit mathematical expression and/or source code is available.

The simplest approximation to the pair correlation function of hard-spheres with radius a is hole correction (HC), i.e.,

$$g\left(x\right)=\begin{cases}0 & x\in[0,1]\\ 1 & x>1\end{cases}, \tag{3.48}$$

where $x=\dfrac{r}{a}$, r is the distance between the center of two spheres. The HC pair correlation function is formulated by observing that two spheres can not over lap with each other. This is a very crude approximation and simulations with HC pair correlation suffer great error.

The widely used pair correlation function is the Percus-Yevick (PY) [85–87] pair correlation function. These functions are the solutions to the PY equation which is very successful in getting $g(x)$ for short-ranged pair potentials, such as hard-spheres. It is mathematically expressed as

$$
\begin{aligned}
g(x) &= \frac{1}{2\pi xj}\int_{\delta-j\infty}^{\delta+j\infty}\frac{tL(t)\,e^{xt}dt}{12\eta\left[L(t)+S(t)\,e^{t}\right]} && (3.49)\\
&= \frac{1}{24\pi\eta xj}\sum_{n=1}^{\infty}(\,-1)^{n+1}\int_{\delta-i\infty}^{\delta+i\infty}te^{t(x-n)}\left[\frac{L(t)}{S(t)}\right]^{n}dt, && (3.50)
\end{aligned}
$$

where

$$S(t)=(1-\eta)^{2}t^{3}+6\eta(1-\eta)t^{2}+18\eta^{2t}-12\eta(1+2\eta),$$

$$L(t)=12\eta\left[\left(1+\frac{1}{2}\eta\right)t+(1+2\eta)\right].$$

By residue theorem, it can be further written as

$$g(x)=\frac{1}{12\eta x}\sum_{n=1}^{\infty}(\,-1)^{n+1}\,Res\left\{te^{t(x-n)}\left[\frac{L(t)}{S(t)}\right]^{n}\right\}. \tag{3.51}$$

The PY pair correlation function is most suitable for application in our simulation although its explicit expression is very complicated.

Rowlinson [88] proposed the self-consistent (SC) approximation to the pair correlation function which improve the PY pair correlation approximation. We have used directly the available source code to calculate this function and used to simulate composite materials.

3.3 Numerical Results

In this section, the model presented in section 3.1 is applied to determine the effective wave number of non-magnetic composite materials. Both the host medium and the inclusion particles are assumed non-magnetic. Numerical simulations are presented. Comparisons with published experimental results are

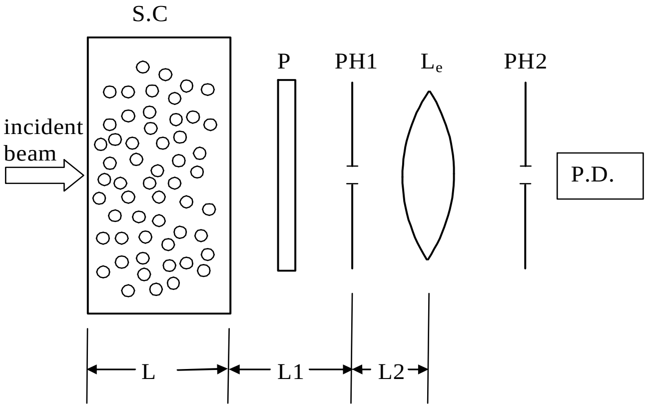

Figure 3-2: Experimental setup by Ishimaru and Kuga [4]: S.C., sample cell; P, polarizer; PH1, pinhole-1 with diameter 3 mm; PH2, pinhole-2 with diameter 25 μm; Le, 10x microscope objective lens; P.D. photodiode; L1, 97 mm; and L2 57 mm.

made wherever possible.

In 1982, Ishimaru and Kuga [4] carried out a series of experimental study of wave attenuation in a dense distribution of particles. Their experimental configuration is shown in Fig. 3-2. The parameters used in their experiments are shown in Table 3.1.

In the Figs. 2 and 3 of [4], the data shown is

$$\gamma = \frac{\alpha\left(k_h a, c\right)}{\alpha_0\left(k_h a, c\right)}, \tag{3.52}$$

where

$$\alpha_0\left(k_h a, c\right) = n_0 \sigma_t\left(k_h a\right), \tag{3.53}$$

$$n_0 = \frac{c}{4\pi a^3/3}, \tag{3.54}$$

Table 3.1: Characteristics of Latex Particles. [4]

Diameter(μm)	0.091	0.109	0.481	1.101
Lot Number	$1A07$	$1A23$	$1A28$	$7G3K$
Standard deviation(μm)	0.0058	0.0027	0.0018	0.0055
Index of refraction	1.588	1.588	1.588	1.588
σ_s $\left(\times 10^{-5}\,\mu\mathrm{m}^2\right)$	3.2912	8.959	12380	-
SD of σ_s $\left(\times 10^{-5}\,\mu\mathrm{m}^2\right)$	1.115	1.317	18.8	-
Measured α $\left(10^{-2}\,\mathrm{mm}^{-1}\right)$ at low density $\left(10^{-3}\right)$	2.080 at 37.69%	1.07 at 9.33%	2.798 at 1.166%	4.72 at 1.166%
α_0 $\left(\times 10^{-2}\,\mathrm{mm}^{-1}\right)$ at the same density	3.137	1.242	2.481	-
α/α_0	0.663	0.862	1.128	–
SD of α/α_0	0.0067	0.0036	0.0129	–
Equivalent diameter	0.080	0.103	0.526 – 0.538	–
Size parameter ka	0.529	0.681	3.518	(7.280)

Table 3.2: Characteristics of Latex Particles (continue). [4]

Diameter(μm)	2.02	5.7	11.9
Lot Number	$1A12$	$1B01$	$1A32$
Standard deviation(μm)	0.0135	1.5	1.9
Index of refraction	1.5768	1.58	1.57 – 1.583
σ_s $(\mu\mathrm{m}^2)$	10.758	59.93	237.067 – 238.88
SD of σ_s $(\mu\mathrm{m}^2)$	8.7×10^{-2}	32.343	74.74 – 75.5
Measured α $\left(10^{-2}\,\mathrm{mm}^{-1}\right)$ at low density $\left(10^{-3}\right)$	2.845 at 1.1898%	0.618 at 1.166%	0.3086 at 1.166%
α_0 $\left(\times 10^{-2}\,\mathrm{mm}^{-1}\right)$ at the same density	2.967	0.5897	0.2926
α/α_0	0.959	1.048	1.055
SD of α/α_0	0.0088	0.0148	0.0215
Equivalent diameter	2.057 – 2.076	5.38 – 5.49	10.08 – 12.64
Size parameter ka	13.662	36.238	82.793

$$\begin{aligned}\sigma_t\left(k_h a\right) &= \frac{4\pi}{k_h} Im\left[\mathbf{f}\left(k_h a, \hat{k}^{inc}, \hat{k}^{inc}\right)\cdot \hat{e}^{inc}\right] \\ &= \frac{4\pi}{k_n^2} Im\left[\mathbf{F}\left(k_h a, \hat{k}^{inc}, \hat{k}^{inc}\right)\cdot \hat{e}^{inc}\right]\end{aligned}, \tag{3.55}$$

where $\mathbf{F}\left(k_h r, \hat{k}^{inc}, \hat{k}^{s}\right)$ is the far-field amplitude of the scattered electric field $\mathbf{E}^s(\mathbf{r})$ in the scattering direction $\hat{k}^s$ of a particle illuminated by a plane wave propagating in the direction $\hat{k}^{inc}$ with unit amplitude.

$$\lim_{k_h r\to\infty} \mathbf{E}^s(\mathbf{r}) = \mathbf{f}\left(k_h r, \hat{k}^{inc}, \hat{k}^{s}\right)\frac{e^{ik_h r}}{r} = \mathbf{F}\left(k_h r, \hat{k}^{inc}, \hat{k}^{s}\right)\frac{e^{ik_h r}}{k_h r}. \tag{3.56}$$

$4\pi Im\left[\mathbf{F}\left(k_h a, \hat{k}^{inc}, \hat{k}^{inc}\right)\cdot \hat{e}^{inc}\right]$ is calculated using Mie theory.

In Fig. 4 of [4], the data shown is

$$\gamma' = \frac{\alpha\left(k_h a, c\right)}{\alpha_0\left(k_h a, 100\%\right)}. \tag{3.57}$$

Therefore,

$$\gamma = \frac{\alpha\left(k_h a, c\right)}{\alpha_0\left(k_h a, c\right)} = \gamma' \frac{\alpha_0\left(k_h a, 100\%\right)}{\alpha_0\left(k_h a, c\right)} = \frac{\gamma'}{c}, \tag{3.58}$$

$$\begin{aligned}\alpha\left(k_h a, c\right) &= \gamma'\alpha_0\left(k_h a, 100\%\right) = \gamma' n_0\left(100\%\right)\sigma_t\left(k_h a\right) \\ &= \gamma'\frac{1}{4\pi a^3/3}\frac{4\pi}{k_n^2} Im\left[\mathbf{F}\left(k_h a, \hat{k}^{inc}, \hat{k}^{inc}\right)\cdot \hat{e}^{inc}\right] \\ &= k_h\gamma'\frac{1}{4\pi\left(k_h a\right)^3/3} 4\pi Im\left[\mathbf{F}\left(k_h a, \hat{k}^{inc}, \hat{k}^{inc}\right)\cdot \hat{e}^{inc}\right]\end{aligned}. \tag{3.59}$$

Accordingly,

$$\frac{\alpha\left(k_h a, c\right)}{k_h} = \gamma'\frac{1}{4\pi\left(k_h a\right)^3/3} 4\pi Im\left[\mathbf{F}\left(k_h a, \hat{k}^{inc}, \hat{k}^{inc}\right)\cdot \hat{e}^{inc}\right]. \tag{3.60}$$

In our simulation, we compute

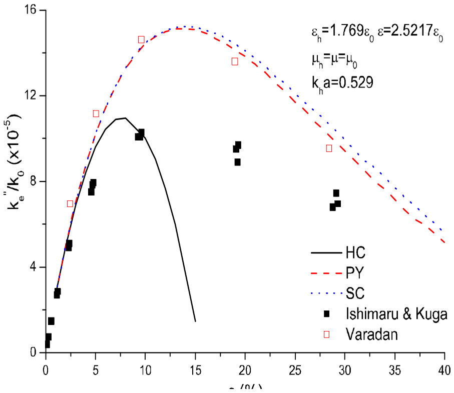

Figure 3-3: Imaginary Part of Effective Wave Number for $k_h a = 0.529$

$$\frac{k_e\left(k_h a, c\right)}{k_0\left(k_h a\right)} = \frac{k_e'\left(k_h a, c\right)}{k_0\left(k_h a\right)} + i\frac{k_e''(k_h a, c)}{k_0\left(k_h a\right)}, \tag{3.61}$$

where

$$\begin{aligned} \frac{k_e''(k_h a, c)}{k_0\left(k_h a\right)} &= \frac{\sqrt{\varepsilon_h}}{2}\frac{\alpha\left(k_h a, c\right)}{k_h} \\ &= \gamma'\frac{\sqrt{\varepsilon_h}}{2}\frac{1}{4\pi(k_h a)^3/3}4\pi Im\left[\mathbf{F}\left(k_h a, \hat{k}^{inc}, \hat{k}^{inc}\right)\cdot\hat{e}^{inc}\right] \end{aligned} \tag{3.62}$$

The simulated imaginary part of the effective wave number for $k_h a = 0.529$, $k_h a = 0.681$, $k_h a = 3.518$, and $k_h a = 7.280$ are shown in Figs. 3-3 - 3-6. We have applied the hole correction (HC) pair correlation function, the Percus Yevick (PY) pair correlation and the self-consistent (SC) pair correlation function.

It is observed that although the SC result is slightly higher than the PY result, there is no significant discrepancy between them. The PY and SC results are almost identical to the HC result for $c \ll c_p$, where c_p is the volume concentration where the maximum attenuation occurs. The PY and SC results are closer to the experimental results than the HC result for $c > c_p$. The TCQ model with HC

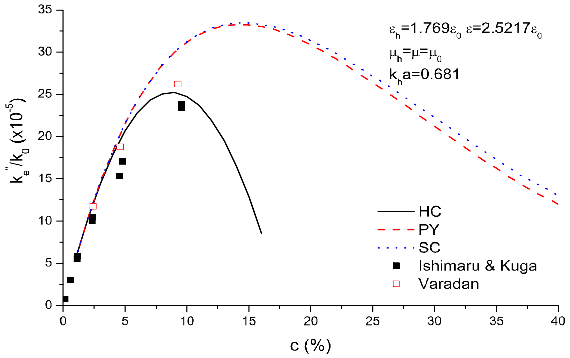

Figure 3-4: Imaginary Part of Effective Wave Number for $k_h a = 0.681$

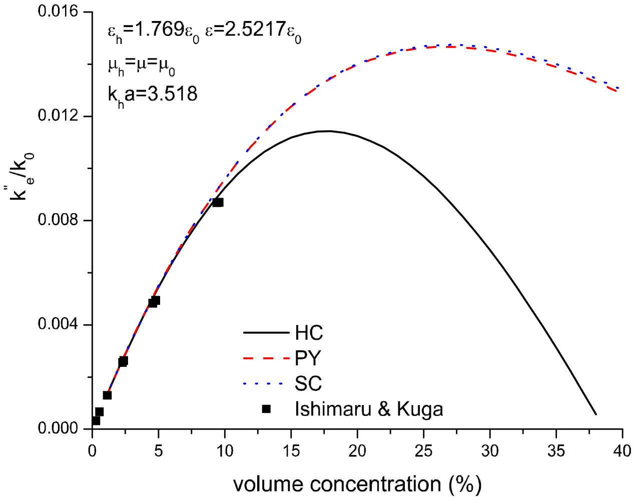

Figure 3-5: Imaginary Part of Effective Wave Number for $k_h a = 3.518$

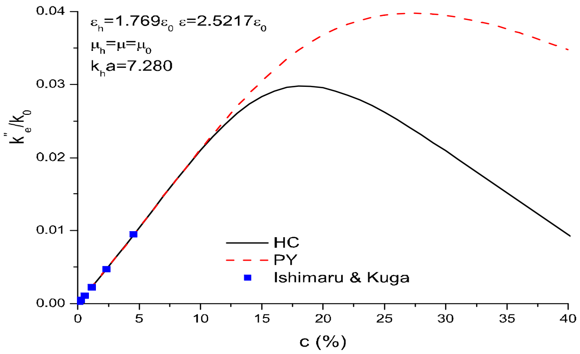

Figure 3-6: Imaginary Part of Effective Wave Number for $k_h a = 7.280$

pair correlation function even breaks down if the volume concentration exceeds a size-dependent breakdown point $\bar{c}\,(k_h a)$. The breakdown points observed are $\bar{c}\,(0.529) \approx 17\%$, $\bar{c}\,(0.681) \approx 19\%$, and $\bar{c}\,(3.518) \approx 39\%$ respectively. We have not observed the breakdown point for the case $k_h a = 7.280$.

More importantly, it is observed that the simulation results agreed better with the experimental results for composite materials with larger inclusion particles. This is understandable, since it is more difficult to measure small attenuation accurately, in comparison to the measurement of high attenuation constant. In addition, the measured size of the inclusion particles is more inaccurate for smaller inclusion particles. In [4], Ishimaru and Kuga noticed that the values provided by the manufacturer did not fit well with the experimental results. They estimated an equivalent diameter to fit the experimental results. We noticed that the total cross scattering section $\sigma_t\,(k_h a)$ for computation of $\alpha_0\,(k_h a, c)$ or $\alpha_0\,(k_h a, 100\%)$ is very sensitive to the particle size $k_h a$, for relatively small particles. Therefore, negligibly small error of the estimated equivalent diameter will result in obvious discrepancy between the experimental and simulation

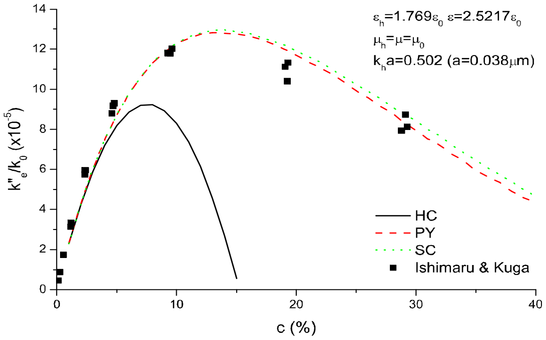

Figure 3-7: Imaginary Part of Effective Wave Number for $k_h a = 0.502$

results. We have found that the experimental and simulation results agree well if the equivalent diameter is $0.076\,\mu$m ($k_h a = 0.502$) in the first experiment, as shown in Fig. 3-7. Similarly, we obtained closer agreement for an equivalent diameter of $0.1\,\mu$m ($k_h a = 0.660$) in the second experiment, as shown in Fig. 3-8. It is obvious that the equivalent diameter of $k_h a = 3.518$ has also been slightly over-estimated by Ishimaru and Kuga. However, we did not adjust this equivalent diameter, since the discrepancy is negligible. The simulation result for $k_h a = 7.280$ agrees perfectly well with the experimental data.

k''_e increases to the attenuation peak as the volume concentration increases, and decreases beyond that. This confirms the observation of attenuation peak in [4] for small inclusion particles and the forecast of attenuation peak in [4] for larger particles that "the attenuation is expected to decrease eventually at much higher densities". The attenuation peak and the corresponding volume concentration are strongly size-dependent. For the above cases, the larger the inclusion particles are, the higher the attenuation peak and the corresponding volume concentration are.

The simulated real part of the effective wave number k'_e is shown in Fig. 3-9. It is easy to observe that k'_e is almost linearly proportional to the concentration

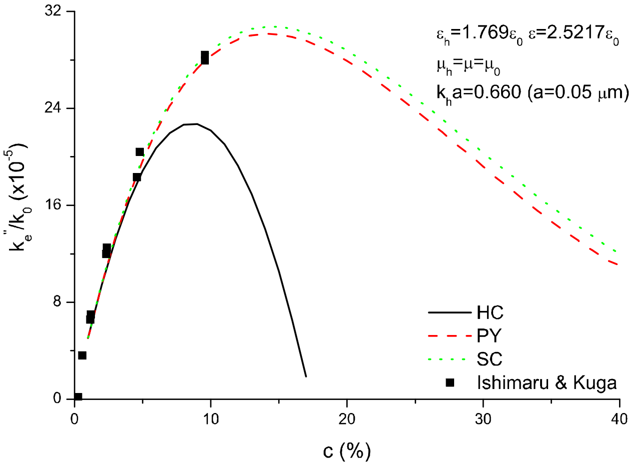

Figure 3-8: Imaginary Part of Effective Wave Number for $k_h a = 0.660$

for $k_h a = 0.529$, $k_h a = 0.681$ and $k_h a = 3.518$. The linearity between k'_e and volume concentration disappears for $k_h a = 7.280$. k'_e increases a little as the inclusion particles are larger. However, it is not size sensitive.

3.4 Conclusions

In this chapter, TCQ method is derived and applied to study the effective electromagnetic properties of composite materials with random spherical inclusions. An more appropriate objective function in terms of the effective propagation constant is defined based on the governing eigen equation of TCQ method. The problem of determining the effective propagation constant is transformed into an optimization problem. To ensure the accuracy and efficiency of solution, DES instead of Muller's method is applied to solve the optimization problem.

The existence of attenuation peak with increasing concentration is numerically confirmed. The attenuation due to multiple scattering between inclusion particles is more prominent for composites with electrically larger inclusion particles.

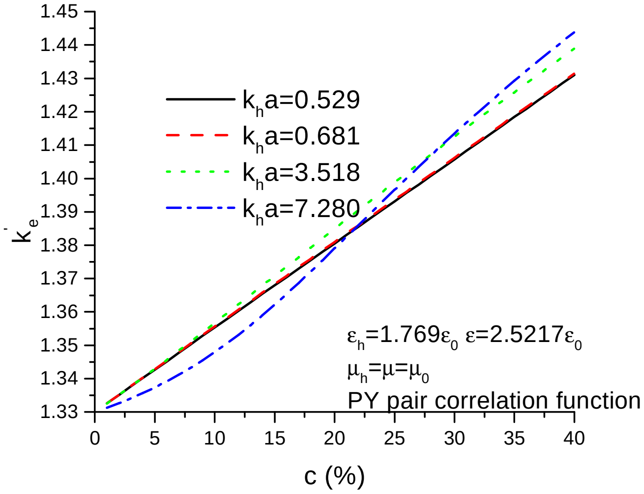

Figure 3-9: Real Part of Effective Wave Number

Chapter 4

Composite Materials with Spheroidal Inclusions

In chapter 3, we have assumed that the inclusion particles are aligned with each other in order to obtain the effective propagation constant. However, it is too restrictive to model many realistic cases where scatterers are most likely to take arbitrary orientation. Other than spheres, which have no preferred orientation, spheroids have the simplest shapes that deviate from that of spheres. More importantly, it introduces shape anisotropy into the composite system. Most particles are not spheres and possess a preferred polarization direction. Spheroid is a good model for simulating this behavior of non-spherical particles. In this chapter, composite with random spheroidal inclusions with either aligned or arbitrary orientation is studied by the TCQ method. Section 4.1 extends the TCQ method to model random spheroids. Numerical results are presented in section 4.2. Finally, conclusions are given in section 4.3.

4.1 Theory

Randomly distributed spheroidal inclusions in a composite material are shown in Fig. 4-1. Assume these spheroids are identical. Eq. 3.22 is still applicable. Applying orientational average over Eq. 3.22, we can write approximately

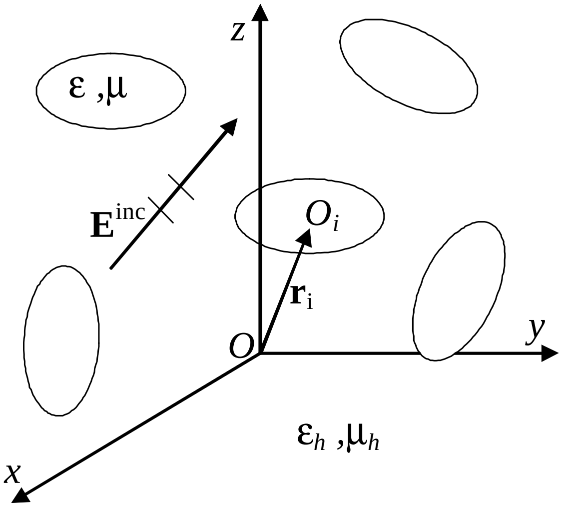

Figure 4-1: Composite Materials with Randomly Distributed Inclusions

$$\left\langle \left\langle \mathbf{f}^{i} \right\rangle_{i} \right\rangle = \left\langle \mathrm{T}^{i} \right\rangle \cdot \left(\mathbf{a}^{i} + n \int_{V'} g\left(\mathbf{r}_{ji}\right) \mathbf{V}^{ij} \cdot \left\langle \left\langle \mathbf{f}^{j} \right\rangle_{j} \right\rangle d\mathbf{r}_{j} \right). \tag{4.1}$$

Following the same procedures as given in section 3.1, we can obtain

$$\left\langle \mathbf{Y} \right\rangle = \left\langle \mathbf{T}^{i} \right\rangle \cdot \mathbf{V}' \cdot \left\langle \mathbf{Y} \right\rangle, \tag{4.2}$$

where it has been assumed that $\left\langle \left\langle \mathbf{f}^{i} \right\rangle_{i} \right\rangle = \left\langle \mathbf{Y} \right\rangle e^{i\mathbf{k}_{e}\cdot\mathbf{r}_{i}}$. The difference between Eq. 4.2 and Eq. 3.45 is the T-matrix term. A coordinate rotation operation needs to be performed.

4.1.1 T-matrix under Coordinates Rotation

The T-matrix of a scatterer has been derived in section 2.1 as:

$$\bar{\mathbf{T}} = \bar{\mathbf{B}} \cdot \bar{\mathbf{A}}^{-1}. \tag{4.3}$$

In the rotated coordinate system (x', y', z'), it is written as

$$\bar{\mathbf{T}}' = \bar{\mathbf{B}}' \cdot \left(\bar{\mathbf{A}}'\right)^{-1}. \tag{4.4}$$

Define a block diagonal matrix of Wigner D-functions

$$\mathbf{D}\left(\alpha\beta\gamma\right) = \begin{bmatrix} D^1\left(\alpha\beta\gamma\right) & & & \\ & \cdots & & \\ & & D^n\left(\alpha\beta\gamma\right) & \\ & & & \cdots \end{bmatrix}, \tag{4.5}$$

where

$$\mathbf{D}^n\left(\alpha\beta\gamma\right) = \left[D^{(n)}_{mm'}\left(\alpha\beta\gamma\right)\right]. \tag{4.6}$$

From Eqs. (C.1) and (C.10), it can be shown that

$$\mathbf{D}^{-1}\left(\alpha\beta\gamma\right) = \mathbf{D}^{+}\left(\alpha\beta\gamma\right), \tag{4.7}$$

where the superscript -1 and $+$ stand for matrix inverse and matrix complex conjugate transpose respectively. With the vector spherical wave functions rotational addition theorems derived in section C.3, it can be shown that

$$\bar{\mathbf{B}} = \begin{bmatrix} D\left(\alpha\beta\gamma\right) & \\ & D\left(\alpha\beta\gamma\right) \end{bmatrix}^{*} \cdot \bar{\mathbf{B}}' \cdot \begin{bmatrix} D\left(\alpha\beta\gamma\right) & \\ & D\left(\alpha\beta\gamma\right) \end{bmatrix}^{+}, \tag{4.8}$$

$$\bar{\mathbf{A}} = \begin{bmatrix} D\left(\alpha\beta\gamma\right) & \\ & D\left(\alpha\beta\gamma\right) \end{bmatrix}^{*} \cdot \bar{\mathbf{A}}' \cdot \begin{bmatrix} D\left(\alpha\beta\gamma\right) & \\ & D\left(\alpha\beta\gamma\right) \end{bmatrix}^{+}. \tag{4.9}$$

Therefore,

$$\begin{aligned}\bar{\mathbf{T}} &= \begin{bmatrix} D\left(\alpha\beta\gamma\right) & \\ & D\left(\alpha\beta\gamma\right)\end{bmatrix}^{*} \cdot \bar{\mathbf{T}}' \cdot \begin{bmatrix} D^{*}\left(\alpha\beta\gamma\right) & \\ & D^{*}\left(\alpha\beta\gamma\right)\end{bmatrix}^{-1} \\ &= \begin{bmatrix} D\left(\alpha\beta\gamma\right) & \\ & D\left(\alpha\beta\gamma\right)\end{bmatrix}^{*} \cdot \bar{\mathbf{T}}' \cdot \begin{bmatrix} D\left(\alpha\beta\gamma\right) & \\ & D\left(\alpha\beta\gamma\right)\end{bmatrix}^{T}\end{aligned} , \qquad (4.10)$$

where the superscript T means matrix transpose.

4.1.2 Orientationally Averaged T-matrix

The average effect of random orientation of a scatterer is represented by its orientationally averaged T-matrix. The averaged T-matrix over all possible orientations of the scatter is written as

$$\left\langle \bar{\mathbf{T}} \right\rangle = \frac{1}{8\pi^2}\int_0^{2\pi} d\alpha \int_0^{2\pi} d\gamma \int_0^{\pi} \bar{\mathbf{T}} \sin\beta d\beta, \qquad (4.11)$$

$$\left\langle \mathbf{T} \right\rangle = \frac{1}{8\pi^2}\int_0^{2\pi} d\alpha \int_0^{2\pi} d\gamma \int_0^{\pi} \mathbf{T} \sin\beta d\beta. \qquad (4.12)$$

From [89],

$$\frac{1}{8\pi^2}\int_0^{2\pi} d\alpha \int_0^{2\pi} d\gamma \int_0^{\pi} D_{mm'}^{*\,(n)}\left(\alpha\beta\gamma\right) D_{\mu\mu'}^{(\nu)}\left(\alpha\beta\gamma\right) \sin\beta d\beta \qquad (4.13)$$

$$= \delta_{m\mu}\delta_{m'\mu'}\delta_{n\nu}\frac{1}{2n+1}. \qquad (4.14)$$

Therefore,

$$\left\langle \left[\bar{\mathbf{T}}_{mn,\mu\nu}\right] \right\rangle = \delta_{m\mu}\delta_{n\nu}\frac{1}{2n+1}\sum_{m'}\delta_{m'\mu'}\left[\bar{\mathbf{T}}'_{m'n,\mu'\nu}\right], \qquad (4.15)$$

$$\left\langle \left[\mathbf{T}_{mn,\mu\nu}\right] \right\rangle = \delta_{m\mu}\delta_{n\nu}\frac{1}{2n+1}\sum_{m'}\delta_{m'\mu'}\left[\mathbf{T}'_{m'n,\mu'\nu}\right]. \qquad (4.16)$$

In order to solve Eq. 4.2, we transfer the problem of determining the effective wave number of composite materials into an optimization problem and solve the optimization problem using the differential evolution strategy [67].

4.2 Numerical Results

In this section, the effective wave numbers of non-magnetic composite materials with spheroidal inclusions are studied numerically using the TCQ method. Both the host medium and the inclusion particles are assumed non-magnetic.

4.2.1 Composite Materials with Aligned Dielectric Spheroidal Inclusions

The composite materials with aligned dielectric spheroidal inclusions are considered first. Although this kind of composite materials is unrealistic, investigating on it may give us some understanding of the anisotropic properties of composite materials with orientation preference. The SC pair correlation function is used in our simulation.

The relationship between the effective wave number of the composite material and the volume concentration is shown in Figs. 4-2—4-5. The effects of inclusion size, incident angle and aspect ratio on the effective wave number of composite material, $k_e = k_e' + ik_e''$, are studied.

From the figures, we observe that k_e' is almost linearly proportional to the concentration for all of the presented cases. It is insensitive to the inclusion particle size. However, k_e'' increases to the attenuation peak as the volume concentration increases, and decreases beyond that. The attenuation peak is present in all cases. It is strongly size dependent. Larger particle results in larger attenuation. For small particle, such as $k_h a = 0.1$, the attenuation is negligible. The different behavior between k_e' and k_e'' is the result of multiple scattering among scatterers. EMT is not able to address this issue.

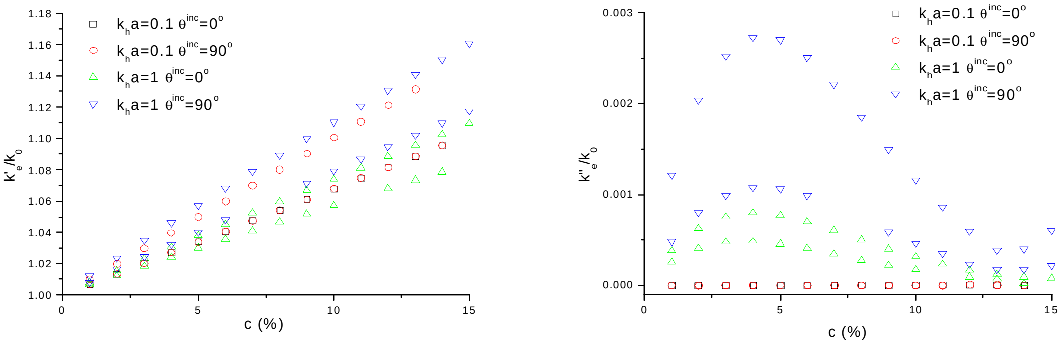

(a) (b)

Figure 4-2: Effective wave number-volume concentration relation of composite materials with aligned spheroidal dielectric inclusion of aspect ratio 2. (a) the normallized real part of effective wave number. (b) the normallized imaginary part of the effective wave number. ($\varepsilon_h = \varepsilon_0$, $\varepsilon = 4\varepsilon_0$, $\mu_h = \mu = \mu_0$, $a/b = 2$)

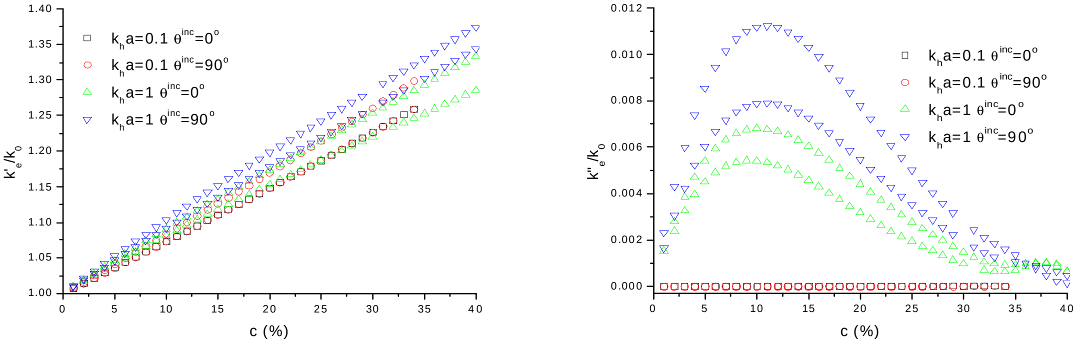

(a) (b)

Figure 4-3: Effective wave number-volume concentration relation of composite materials with aligned spheroidal dielectric inclusion of aspect ratio 1.25. (a) the normallized real part of effective wave number. (b) the normallized imaginary part of the effective wave number. ($\varepsilon_h = \varepsilon_0$, $\varepsilon = 4\varepsilon_0$, $\mu_h = \mu = \mu_0$, $a/b = 1.25$)

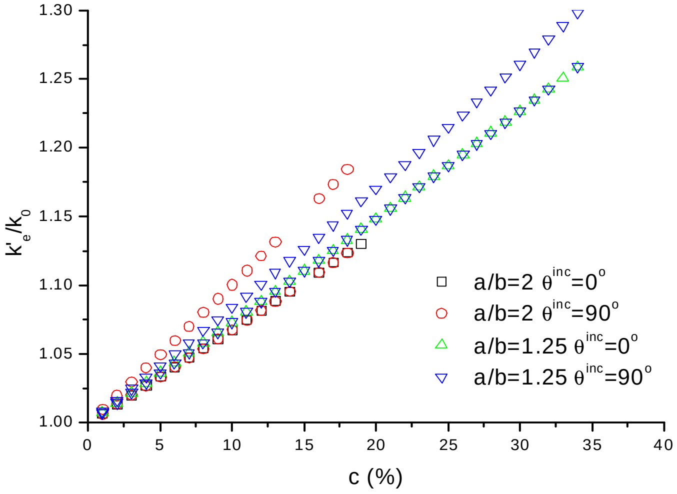

Figure 4-4: Effective wave number-volume concentration relation of composite materials with smaller aligned spheroidal dielectric inclusion. ($\varepsilon_h = \varepsilon_0$, $\varepsilon = 4\varepsilon_0$, $\mu_h = \mu = \mu_0$, $k_h a = 0.1$)

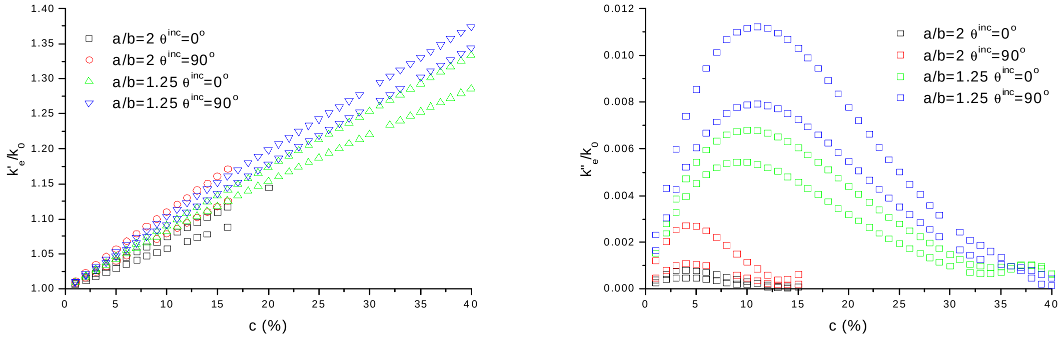

(a)

(b)

Figure 4-5: Effective wave number-volume concentration relation of composite materials with larger aligned spheroidal dielectric inclusion. (a) the normallized real part of effective wave number. (b) the normallized imaginary part of the effective wave number. ($\varepsilon_h = \varepsilon_0$, $\varepsilon = 4\varepsilon_0$, $\mu_h = \mu = \mu_0$, $k_h a = 1$)

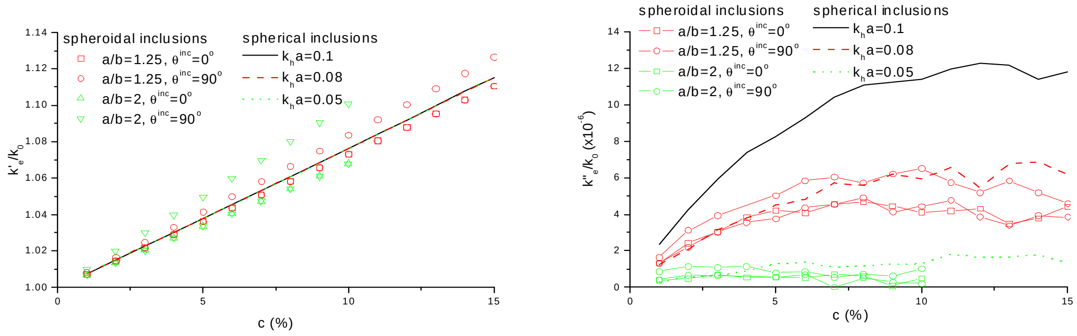

(a)

(b)

Figure 4-6: Comparison of effective wave number of composite materials with smaller spherical and aligned spheroidal inclusion. The lines are results for composites with spherical inclusions and symbols for those with spheroidal inclusions. (a) the normallized real part of effective wave number. (b) the normallized imaginary part of the effective wave number. ($\varepsilon_h = \varepsilon_0$, $\varepsilon = 4\varepsilon_0$, $\mu_h = \mu = \mu_0$, $k_h a = 0.1$ for all spheroidal cases.)

k''_e is also sensitive to the aspect ratio of inclusion particles and the direction of the propagation vector. When the symmetric axis of the inclusion particles is perpendicular with the propagation vector, two separate modes exist. This clearly shows the anisotropy of composite materials with aligned spheroidal inclusion. The two modes tend to be degenerated as the aspect ratio decreases. When the symmetric axis of inclusion particle parallels with the propagation vector, there is only one mode for smaller inclusion particle case ($k_h a = 0.1$). According to crystalline optics, this kind of composite material is effectively uniaxial. However, for larger inclusion particle case ($k_h a = 1$), we found that there are two separate modes.

To have more understanding on the observed anisotropy, comparison of effective wave number of composite materials with spherical and aligned spheroidal inclusion is made. The comparison results are shown in Figs. 4-6 for smaller inclusion case and 4-7 for larger inclusion case.

From Fig. 4-6, it is observed that, when the inclusion particles are very small, k'_e remains unchanged while k''_e keeps decreasing as the size of spherical

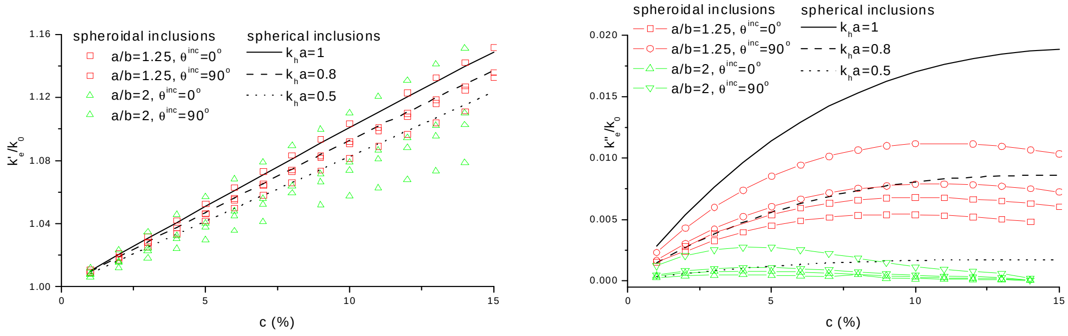

(a)

(b)

Figure 4-7: Comparison of effective wave number of composite materials with larger spherical and aligned spheroidal inclusion. The lines are results for composites with spherical inclusions and symbols for those with spheroidal inclusions. (a) the normallized real part of effective wave number. (b) the normallized imaginary part of the effective wave number. ($\varepsilon_h = \varepsilon_0$, $\varepsilon = 4\varepsilon_0$, $\mu_h = \mu = \mu_0$, $k_h a = 1$ for all spheroidal cases.)

inclusion particles reduces from $k_h a = 0.1$ to $k_h a = 0.05$. For composite materials with aligned spheroidal inclusion particles, when the symmetric axis of inclusion particle parallels with the propagation vector, k_e is unique and is a little bit lower than that of spherical inclusion of radius $k_h b$. On the other hand, when the symmetric axis of inclusion particle is perpendicular to the propagation vector, k_e has two branches. One branch is identical to that of the parallel case. As to the other branch, k'_e is higher than k'_e of spherical inclusion of radius $k_h a$ while k''_e is higher than k''_e of spherical inclusion of radius $k_h b$ and lower than k''_e of spherical inclusion of radius $k_h a$. It is also observed that the larger the aspect ratio is, the larger the anisotropic effect is.

In Fig. 4-7, k_e keeps decreasing as sphere radius reduces from $k_h a = 1$ to $k_h a = 0.5$. For aligned spheroidal inclusion particles, similar anisotropy with smaller inclusion particles is observed when the symmetric axis of inclusion particle is perpendicular with the propagation vector. However, when the wave propagates along the symmetry axis, two branches are observed. k_e of both of the two branches is lower than that of spherical inclusion of radius $k_h b$.

For smaller inclusion particles, the uniqueness of modes when the wave propagates along the particle symmetry axis, and the existence of two separate modes when the particle symmetry axis is perpendicular to the propagation vector, is consistent with crystalline optics [90] for uniaxial material. Therefore, composite material with smaller aligned spheroidal inclusion particles is effectively uniaxial.

On the other hand, the appearance of two separate modes in composite materials with larger aligned spheroidal inclusion particles when the wave propagates along the particle symmetry agree well with the propagation characteristics of plane waves in general non-magnetic anisotropic material. Note that we have observed relatively high effective loss due to multiple scattering between inclusion particles in such composite material, it is quite possible that effective permittivity tensor of composite material with larger aligned spheroidal inclusion particles becomes non-symmetric and complex.

Next, we will investigate the angle dependence of k_e. Without loss of generality, $\phi^{inc} = 0^o$ is assumed. The simulation results are shown in Fig. 4-8. In Fig. 4-8, two branches are observed in all cases. The composite material with smaller spheroidal inclusion ($k_h a = 0.1$) presents typical characteristics of uniaxial anisotropy that one branch is independent on θ^{inc} while the other branch is clearly dependent on θ^{inc}. According to crystalline optics, the two branches correspond to different linear polarizations. The flat branch corresponds to ordinary wave, while the other direction dependent branch corresponds to extraordinary wave.

When the inclusion particle is larger, the effective property of composite material is completely different. In this case, both branches are θ^{inc} dependent. In addition, the angle dependence of the two branches looks similar. This agrees well with the propagation characteristics of plane waves in general non-magnetic anisotropic material.

The effect due of the aspect ratio of spheroidal particles on k_e is illustrated in Fig. 4-9. It is obvious from the results obtained that there is no effective anisotropy for spherical inclusion particles. The anisotropy becomes stronger

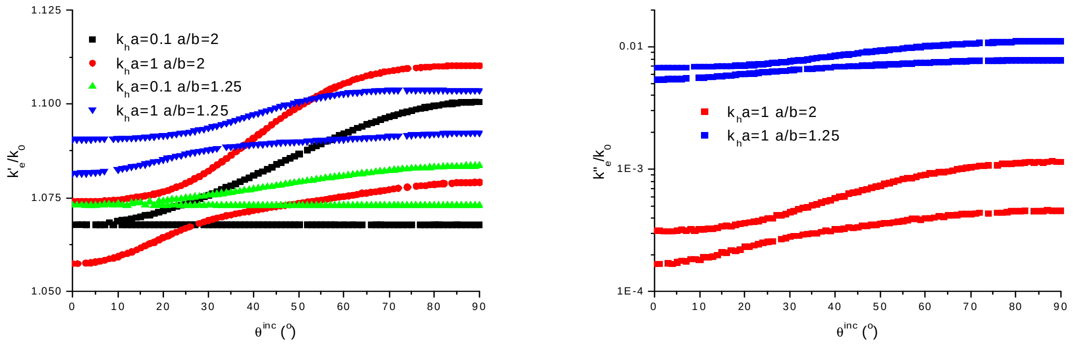

(a)

(b)

Figure 4-8: Effective wave number-direction of propagation vector relation of composite materials with aligned spheroidal dielectric inclusion. (a) the normallized real part of effective wave number. (b) the normallized imaginary part of the effective wave number. ($\varepsilon_h = \varepsilon_0$, $\varepsilon = 4\varepsilon_0$, $\mu_h = \mu = \mu_0$, $c = 10\%$)

as the aspect ratio increases. Similarly, we found that the composite materials with smaller and larger inclusion particles exhibit different anisotropy properties. We also observed from Fig. 4-9 that the effective wave number decreases as the aspect ratio increases, when the wave propagates along the particle symmetry axis. This is reasonable because the polarization effect is weaker for larger aspect ratio particles. On the other hand, there are two separate branches when the wave propagation vector is perpendicular to the particle symmetry axis. In one branch, the effective wave number increases as the aspect ratio increases. The other branch shows reverse trend.

4.2.2 Composite Materials with Random Dielectric Spheroidal Inclusions

In this section, we will consider the bulk composite materials with random distribution of dielectric spheroidal inclusions. The composite material is bulk so that there is no orientation preference for the inclusion particles. The simulation

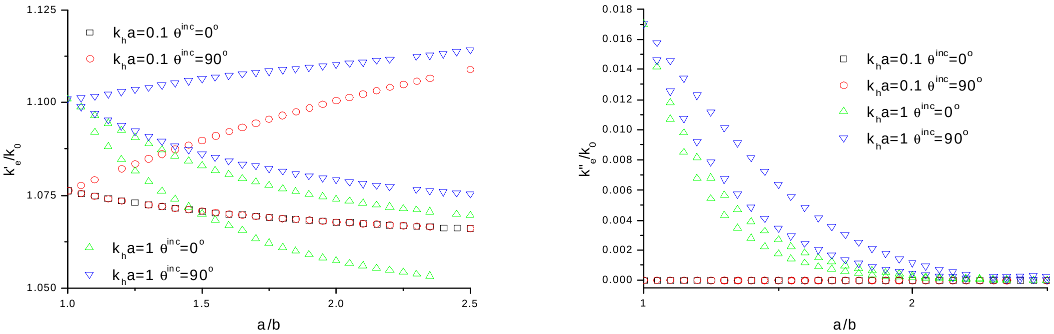

(a) (b)

Figure 4-9: Effective wave number-aspect ratio relation of composite materials with aligned spheroidal dielectric inclusion. (a) the normallized real part of effective wave number. (b) the normallized imaginary part of the effective wave number. ($\varepsilon_h = \varepsilon_0$, $\varepsilon = 4\varepsilon_0$, $\mu_h = \mu = \mu_0$, $c = 10\%$)

results are shown in Figs. 4-10—4-13.

No effective anisotropy is observed in the composites with totally random spheroidal inclusions. The properties of the composites with random spheroidal inclusions look similar to those with spherical inclusions. For all the presented cases, k_e' is linearly proportional to volume concentration and increases a little as the inclusion particles are larger. However, it is not size sensitive. The attenuation peak, shown by the curves of k_e'', is present in all cases. k_e'' is strongly size dependent. Larger particle results in larger attenuation. For small particle, such as $k_h a = 0.1$, the attenuation is negligible. k_e'' is also sensitive to the aspect ratio of inclusion particles. The effective isotropic property is further confirmed by studying the angle dependence of the effective wave number of composite materials with random distribution of spheroidal inclusion particles. No angle dependence is observed in the calculated results which are not shown here.

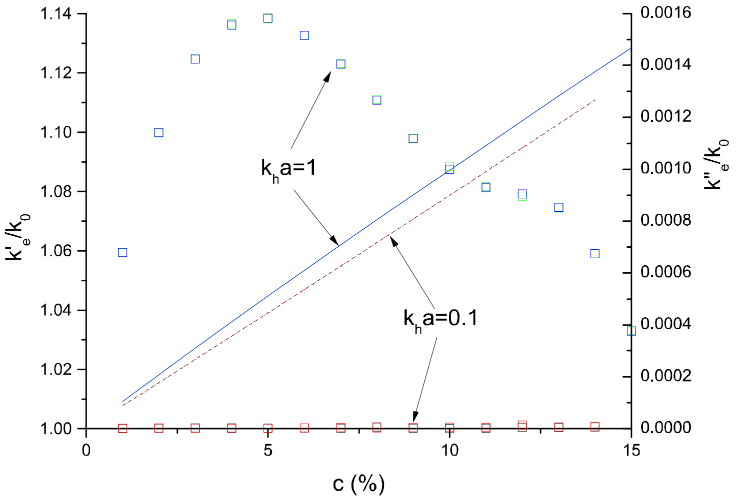

Figure 4-10: Effective wave number-volume concentration relation of composite materials with spheroidal dielectric inclusion of Aaspect ratio 2. The lines are for k_e'/k_0 and the symbols k_e''/k_0. For both inclusion sizes shown in the fibure, the results for $\theta^{inc} = 0°$ and $90°$ overlap. ($\varepsilon_h = \varepsilon_0$, $\varepsilon = 4\varepsilon_0$, $\mu_h = \mu = \mu_0$, $a/b = 2$)

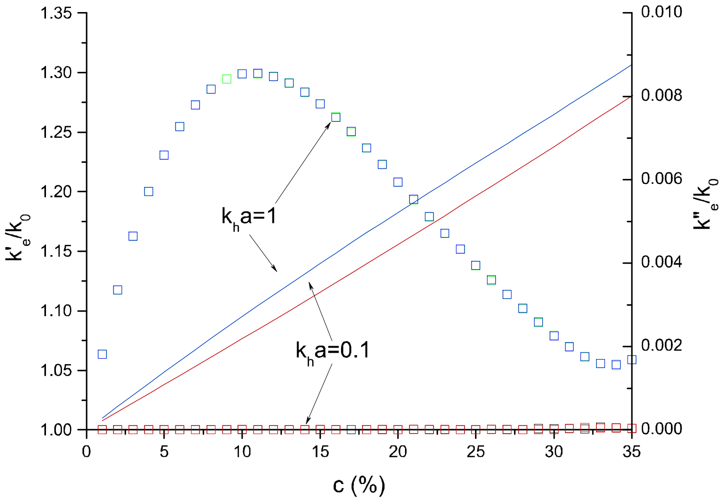

Figure 4-11: Effective wave number-volume concentration relation of composite materials with spheroidal dielectric inclusion of Aaspect ratio 1.25. The lines are for k_e'/k_0 and the symbols k_e''/k_0. For both inclusion sizes shown in the fibure, the results for $\theta^{inc} = 0°$ and $90°$ overlap. ($\varepsilon_h = \varepsilon_0$, $\varepsilon = 4\varepsilon_0$, $\mu_h = \mu = \mu_0$, $a/b = 1.25$)

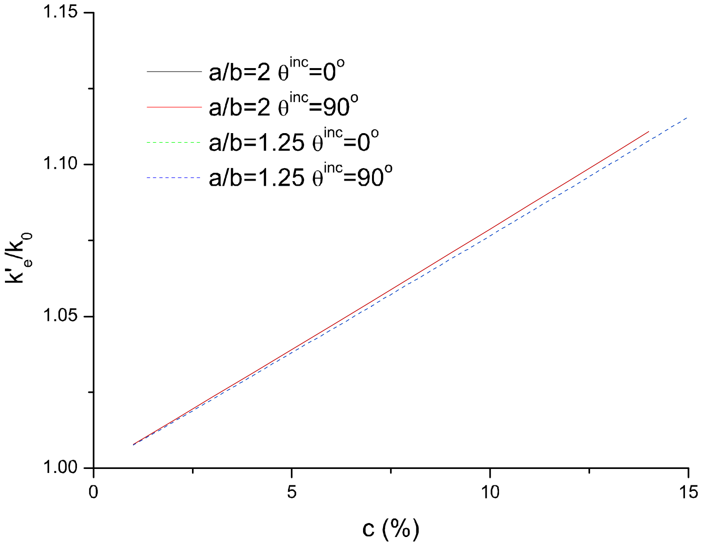

Figure 4-12: Effective wave number-volume concentration relation of composite materials with smaller spheroidal dielectric inclusion. ($\varepsilon_h = \varepsilon_0$, $\varepsilon = 4\varepsilon_0$, $\mu_h = \mu = \mu_0$, $k_h a = 0.1$)

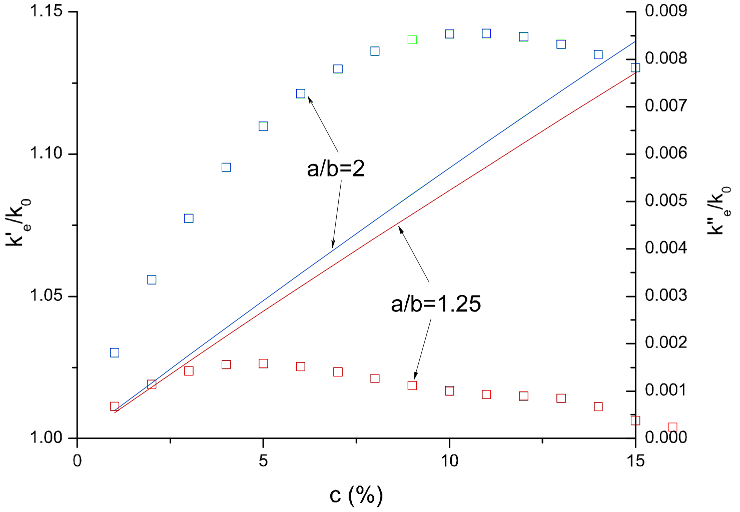

Figure 4-13: Effective wave number-volume concentration relation of composite materials with larger spheroidal dielectric inclusion. The lines are for k_e'/k_0 and the symbols k_e''/k_0. For both inclusion sizes shown in the fibure, the results for $\theta^{inc} = 0°$ and 90° overlap.($\varepsilon_h = \varepsilon_0$, $\varepsilon = 4\varepsilon_0$, $\mu_h = \mu = \mu_0$, $k_h a = 1$)

4.3 Conclusions

In this chapter, the TCQ model and the DES algorithm are applied to analyze the effective electromagnetic properties of composite materials with aligned and random spheroidal inclusions.

For composite materials with aligned spheroidal inclusion, different anisotropy is observed for different size of inclusions. Composite materials with smaller aligned spheroidal inclusion particles behave like uniaxial material. When the inclusion particles are larger, the composite materials have two separate propagation modes even if the wave propagates along the particle symmetry axis. In addition, both modes are propagation direction dependent and the dependency relationship look similar. This agrees well with the propagation characteristics of plane waves in a general nonmagnetic anisotropic material.

When the inclusion particles in composite materials are allowed to take random orientation, the effective anisotropy disappears. The characteristics of composite materials with random spheroidal inclusion particles are very similar to those with spherical inclusion particles. It is also noticed that the composite materials with larger aligned inclusion particles are effectively quite lossy.

For the design of lossy composite materials, larger particles are preferred due to their stronger multiple scattering loss. If anisotropic composite materials are desired, the anisotropically shaped particles have to be arranged so that their preferred polarization directions are aligned.

Chapter 5

Composite Slabs with Fiber Inclusions

The application of Both EMT and TCQ methods are limited by the shape of the inclusions. They are hardly applicable to composites with inclusions that have large aspect ratios, such as disks and fibers. Composite materials with conductive fibers are of great practical interests, due to their unique properties. For example, high permittivity composites can be fabricated using low concentrations of fibers, and the dielectric dispersion curve can be 'shaped' by using fibers with different properties.

In this chapter, fiber composite slabs are numerically studied. The scattering properties of the fibers are calculated by MoM. The configurational average on the random distribution of fibers is considered by the Monte Carlo simulation. The effective transmission and reflection coefficients of a composite slab are obtained through numerical simulation. The relationship between configurationally averaged scattered field and the effective transmission and reflection coefficients are derived in Section 5.1. The results are compared with Maxwell-Garnnet theory. The method for numerical simulation of fiber composite materials are described in Section 5.2. Section 5.3 studies the minimal sample size for accurate simulation of fiber composites. The effect of fiber conductivity, concentration, length, electrical contacts among fibers and wave frequency on the minimal sample size are studied in detail. Numerical results on the fiber composite simulation are given in Section 5.5.

5.1 Transmission and Reflection Coefficients of Composite Slabs

A general theory for composite slabs is presented in this section. The effective reflection and transmission coefficients can be obtained based on the configurationally averaged scattered field of the inclusions. The configuration of a composite slab is shown in Fig. 5-1. Scatterers of arbitrary shape are randomly distributed in a planarly stratified host slab of $N-2$ layers (from region 2 to region N-1). The indices for regions and interfaces follow those used by Chew [91] except that the origin of the coordinate is set to the first interface of the host medium. Therefore, $d_1 = 0$. Region 1 and N are the background medium of the slab. Each region is characterized by its relative permittivity ε_i and relative permeability μ_i, where i is the region index. Each region has a relative impedance $\eta_i = \sqrt{\mu_i/\varepsilon_i}$ to free-space. The total thickness of the slab is $h = d_{N-1}$.

5.1.1 Theory

The transmission coefficient of the composite slab is firstly derived. Region 1 and N are assumed to be the same for convenience. Consider a plane wave (time factor $e^{j\omega t}$ is assumed and suppressed)

$$\mathbf{E}^{inc}\left(\mathbf{r}\right) = \hat{e}e^{-j\mathbf{k}^{inc}\cdot\mathbf{r}}, \tag{5.1}$$

which illuminate the composite slab from below, where $\mathbf{k}^{inc} = k_1\hat{k}^{inc}$ is the wave vector in region 1 and $\hat{k}^{inc} = \alpha\hat{x} + \beta\hat{y} + \gamma\hat{z}$. The coordinates used for the jth scatterer has been illustrated in Fig. 5-1.

Let $\mathbf{I}\left(\mathbf{r}'\right)$ be the current distribution on the jth scatterer in the composite slab and $\mathbf{E}_j^s\left(\mathbf{r}\right)$ the scattered far field at point $\mathbf{r}$ due to this scatterer. Construct

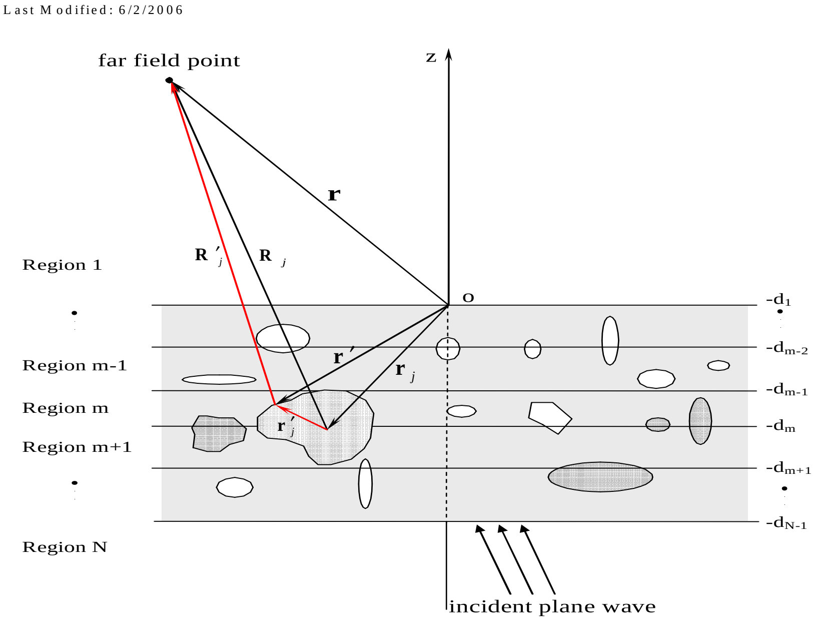

Figure 5-1: Random Composite Slab Model

a uniform current dipole $\hat{p}_t I_t l_t \delta\left(\mathbf{r}''-\mathbf{r}\right)$ at point $\mathbf{r}$, where $\hat{p}_t$ is the unit direction of the dipole, $I_t l_t$ is the current moment. The electric field at point $\mathbf{r}'$ radiated from this uniform current dipole is denoted by $\mathbf{E}_t\left(\mathbf{r}'\right)$. According to reciprocal theorem [92], we can write

$$\int\limits_{\substack{\text{over}\\ \text{dipole}}} \mathbf{E}_j^s\left(\mathbf{r}''\right)\cdot\hat{p}_t I_t l_t \delta\left(\mathbf{r}''-\mathbf{r}\right) d\mathbf{r}'' = \int\limits_{\substack{\text{over}\\ \text{scatterer}}} \mathbf{E}_t\left(\mathbf{r}'\right)\cdot\mathbf{I}\left(\mathbf{r}'\right) d\mathbf{r}', \tag{5.2}$$

or

$$\mathbf{E}_j^s\left(\mathbf{r}\right)\cdot\hat{p}_t = \frac{1}{I_t l_t}\int\limits_{\substack{\text{over}\\ \text{scatterer}}} \mathbf{E}_t\left(\mathbf{r}'\right)\cdot\mathbf{I}\left(\mathbf{r}'\right) d\mathbf{r}'. \tag{5.3}$$

When the uniform current dipole is far from all the scatterers in the composite slab and the space is homogeneous, $\mathbf{E}_t\left(\mathbf{r}'\right)$ can be written as

$$\begin{aligned}\mathbf{E}_t\left(\mathbf{r}'\right) &= -j\omega\mu_1 \int\limits_{\substack{\text{over}\\ \text{dipole}}} \frac{e^{-jk_1\left|\mathbf{r}''-\mathbf{r}'\right|}}{4\pi\left|\mathbf{r}''-\mathbf{r}'\right|}\hat{p}_t I_t l_t \delta\left(\mathbf{r}''-\mathbf{r}\right) d\mathbf{r}'' \\ &= -j\omega\mu_1 \frac{e^{-jk_1\left|\mathbf{r}-\mathbf{r}'\right|}}{4\pi\left|\mathbf{r}-\mathbf{r}'\right|}\hat{p}_t I_t l_t\end{aligned}. \tag{5.4}$$

Equation (5.4) can also be written as

$$\mathbf{E}_t\left(\mathbf{r}'\right) = -j\omega\mu_1 \frac{e^{-jk_1\left|\mathbf{R}_j-\mathbf{r}'_j\right|}}{4\pi\left|\mathbf{R}_j-\mathbf{r}'_j\right|}\hat{p}_t I_t l_t \approx -j\omega\mu_1 \frac{e^{-jk_1 R_j}}{4\pi R_j} e^{jk_1\hat{R}_j\cdot\mathbf{r}'_j}\hat{p}_t I_t l_t,$$

where $R_j = \left|\mathbf{R}_j\right| = \left|\mathbf{r}-\mathbf{r}_j\right|$, $\hat{R}_j = \mathbf{R}_j/R_j = \left(\hat{R}_{jx},\hat{R}_{jy},\hat{R}_{jz}\right)$ and $R_j >> r'_j$. $\mathbf{E}_t\left(\mathbf{r}'\right)$ is a plane wave and only the transverse to $\hat{R}_j$ components exit. In the presence of stratified medium, it is convenient to express $\mathbf{E}_t\left(\mathbf{r}'\right)$ into TE and TM terms as

$$\begin{aligned}&\mathbf{E}_t^{TE}\left(\mathbf{r}'\right) = \\ &-j\omega\mu_1 \frac{e^{-jk_1 R_j}}{4\pi R_j} e^{jk_1\hat{R}_j\cdot\mathbf{r}'_j} I_t l_t \times \\ &\left\{e^{-jk_1\hat{R}_{jz}\left(z_j+z'_j\right)}\left[\tilde{S}_{1,m}^{TE} e^{-jk_{mz}\left(-d_{m-1}-z'\right)}\right]\left[1+\tilde{R}_{m,m+1}^{TE} e^{-j2k_{mz}\left(z'+d_m\right)}\right]\hat{\phi}_m\right\},\end{aligned} \tag{5.5}$$

$$
\begin{aligned}
&\mathbf{E}_t^{TM}(\mathbf{r}') = \\
&-j\omega\mu_1 \frac{e^{-jk_1R_j}}{4\pi R_j} e^{jk_1\hat{R}_j\cdot\mathbf{r}'_j} I_t l_t \times \\
&\left\{ e^{-jk_1\hat{R}_{jz}\left(z_j+z'_j\right)} \left[\frac{\eta_m}{\eta_1}\tilde{S}^{TM}_{1,m} e^{-jk_{mz}(-d_{m-1}-z')}\right] \left[\hat{\theta}_m + \hat{\theta}'_m \tilde{R}^{TM}_{m,m+1} e^{-j2k_{mz}(z'+d_m)}\right] \right\},
\end{aligned}
\tag{5.6}
$$

where the terms in curly brackets accounts for the effect of stratified medium. The region index m has been chosen so that $\mathbf{r}'$ resides in region m. z' is a component of $\mathbf{r}' = (x', y', z')$, $\tilde{S}^{TE}_{1m}$ and $\tilde{S}^{TM}_{1m}$ are the generalized transmission coefficients that relate the down going wave in region m to that in region 1 where the effect of all layers are accounted for [91] [93]. $\tilde{R}^{TE}_{m,m+1}$ and $\tilde{R}^{TM}_{m,m+1}$ are the generalized reflection coefficients at the interface between region m and $m+1$ relating the up-going wave to the down-going wave in that region where the effect of all layers are accounted for. $\hat{\theta}_m$ and $\hat{\theta}'_m$ are the unit $\mathbf{E}$ field vector for the down-going and up-going TM waves, respectively, in region m. $\hat{\phi}_m$ is the unit $\mathbf{E}$ field vector for the TE wave in region m.

Substituting Eqs. (5.5) and (5.6) into Eq. (5.3), we have

$$
E_j^{s,TE}(\mathbf{r}) = -j\omega\mu_1 \frac{e^{-jk_1R_j}}{4\pi R_j} e^{-jk_1\hat{R}_{jz}z_j} A_j^{TE}\left(\hat{R}_j\right), \tag{5.7}
$$

$$
E_j^{s,TM}(\mathbf{r}) = -j\omega\mu_1 \frac{e^{-jk_1R_j}}{4\pi R_j} e^{-jk_1\hat{R}_{jz}z_j} A_j^{TM}\left(\hat{R}_j\right), \tag{5.8}
$$

where

$$
\begin{aligned}
A_j^{TE}\left(\hat{R}_j\right) = \int\limits_{\substack{\text{over}\\ \text{scatterer}}} & e^{jk_1\hat{R}_j\cdot\mathbf{r}'_j} e^{-jk_1\hat{R}_{jz}z'_j} \left[\tilde{S}^{TE}_{1m} e^{-jk_{mz}(-d_{m-1}-z')}\right] \times \\
& \left[1 + \tilde{R}^{TE}_{m,m+1} e^{-j2k_{mz}(z'+d_m)}\right] \hat{\phi}_m \cdot \mathbf{I}(\mathbf{r}')\, d\mathbf{r}',
\end{aligned}
\tag{5.9}
$$

$$A_j^{TM}\left(\hat{R}_j\right) = \int\limits_{\substack{\text{over}\\ \text{scatterer}}} e^{jk_1\hat{R}_j\cdot\mathbf{r}'_j} e^{-jk_1\hat{R}_{jz}z'_j} \left[\frac{\eta_m}{\eta_1}\tilde{S}_{1m}^{TM} e^{-jk_{mz}(-d_{m-1}-z')}\right] \times \\ \left[\hat{\theta}_m + \hat{\theta}'_m \tilde{R}_{m,m+1}^{TM} e^{-j2k_{mz}(z'+d_m)}\right] \cdot \mathbf{I}\left(\mathbf{r}'\right) d\mathbf{r}'. \tag{5.10}$$

The total scattered field can be written as

$$\mathbf{E}^s\left(\mathbf{r}\right) = \sum_j E_j^{s,TE}\left(\mathbf{r}\right)\hat{\phi}_1 + E_j^{s,TM}\left(\mathbf{r}\right)\hat{\theta}_1. \tag{5.11}$$

Since all scatterers are randomly and uniformly distributed in the slab, it is more meaningful to obtain a configurationally averaged field for a composite with a certain density of inclusions (scatterers). Applying configurational average [77] on Eq. (5.11), and substituting Eqs. (5.7) and (5.8) into Eq. (5.11), we have

$$\begin{aligned} \langle \mathbf{E}^s(\mathbf{r})\rangle &= \int\limits_{V_1} d\mathbf{r}_1 \int\limits_{s_1} ds_1 \cdots \int\limits_{V_N} d\mathbf{r}_N \int\limits_{s_N} ds_N p(\mathbf{r}_1, s_1\cdots\mathbf{r}_N, s_N) \\ &\times \sum_j \frac{e^{-jk_1R_j}}{R_j} e^{-jk_1\hat{R}_{jz}z_j}\left(-j\omega\mu_1\right)\left(A_j^{TE}\hat{\phi}_1 + A_j^{TM}\hat{\theta}_1\right) \end{aligned} \tag{5.12}$$

where $p\left(\mathbf{r}_1, s_1\cdots\mathbf{r}_N, s_N\right)$ is the probability distribution function such that

$$p\left(\mathbf{r}_1, s_1\cdots\mathbf{r}_N, s_N\right) d\mathbf{r}_1 ds_1\cdots d\mathbf{r}_N ds_N$$

represents the probability of finding the scatterers in a configuration in which the first scatterer lies in the elemental volume $d\mathbf{r}_1$ about the point $\mathbf{r}_1$ and has a scattering parameter lying between s_1 and $s_1 + ds_1$, the second scatterer lies in the elemental volume $d\mathbf{r}_2$ about the point $\mathbf{r}_2$ and has a scattering parameter lying between s_2 and $s_2 + ds_2$, and so on [77]. N is the total number of scatterers in volume V. V_i is the volume accessible to the ith scatterer.

In the sense of configurational average, all scatterers are equivalent. Eq. (5.12) can be re-written as

$$\left\langle \mathbf{E}^{sca}\left(\mathbf{r}\right)\right\rangle = N\int\limits_{V_j} d\mathbf{r}_j \int\limits_{s_j} ds_j p\left(\mathbf{r}_j, s_j\right) \frac{e^{-jk_0R_j}}{R_j} \left\langle \mathbf{F}_j\left(\mathbf{r}_j, s_j, \hat{R}_j\right)\right\rangle_j \tag{5.13}$$

$$\left\langle \mathbf{E}^{s}\left(\mathbf{r}\right)\right\rangle = N\int\limits_{V_j} d\mathbf{r}_j \int\limits_{s_j} ds_j p\left(\mathbf{r}_j, s_j\right) \frac{e^{-jk_1R_j}}{R_j} e^{-jk_1\hat{R}_{jz}z_j} \left\langle \mathbf{F}_j\left(\mathbf{r}_j, s_j, \hat{R}_j\right)\right\rangle_j, \tag{5.14}$$

where

$$\left\langle \mathbf{F}_j\left(\mathbf{r}_j, s_j, \hat{R}_j\right)\right\rangle_j = \left\langle -j\omega\mu_1\left(A_j^{TE}\hat{\phi}_1 + A_j^{TM}\hat{\theta}_1\right)\right\rangle_j \tag{5.15}$$

is the conditionally averaged scattering amplitude of the jth scatterer at $\mathbf{r}_j$ with scattering parameter s_j in the presence of all other scatterers, $\left\langle\cdot\right\rangle_j$ is the first order conditional configurational average,

$$\begin{aligned} \left\langle f\left(\mathbf{r}, \mathbf{r}_1, s_1 \cdots \mathbf{r}_N, s_N\right)\right\rangle_j = &\int\limits_{V_1} dr_1 \int\limits_{s_1} ds_1 \cdots \int\limits_{V_{i\neq j}} dr_i \int\limits_{s_{i\neq j}} ds_i \cdots \int\limits_{V_N} dr_N \int\limits_{s_N} ds_N \\ &\times p\left(\mathbf{r}_1, s_1 \cdots, \mathbf{r}_{i\neq j}, s_{i\neq j} \cdots \mathbf{r}_N, s_N\right) f\left(\mathbf{r}, \mathbf{r}_1, s_1 \cdots \mathbf{r}_N, s_N\right), \end{aligned} \tag{5.16}$$

$$p\left(\mathbf{r}_1, s_1 \cdots \mathbf{r}_N, s_N\right) = p\left(\mathbf{r}_j, s_j\right) p\left(\mathbf{r}_1, s_1 \cdots, \mathbf{r}_{i\neq j}, s_{i\neq j}, \cdots \mathbf{r}_N, s_N \left|\mathbf{r}_j, s_j\right.\right). \tag{5.17}$$

Suppose the locations of the scatterers are independent of the scattering parameters, i.e.,

$$p\left(\mathbf{r}_j, s_j\right) = p\left(\mathbf{r}_j\right) p\left(s_j\right). \tag{5.18}$$

If the scatterers are randomly but uniformly distributed in the slab, then

$$p\left(\mathbf{r}_j\right) = 1/V. \tag{5.19}$$

Therefore,

$$\langle \mathbf{E}^s(\mathbf{r}) \rangle = n_v \int\limits_{V_j} d\mathbf{r}_j \frac{e^{-jk_1 R_j}}{R_j} e^{-jk_1 \hat{R}_{jz} z_j} \int\limits_{s_j} ds_j p(s_j) \left\langle \mathbf{F}_j \left(\mathbf{r}_j, s_j, \hat{R}_j \right) \right\rangle_j \tag{5.20}$$

where $n_v = N/V$ is the volume number density of the scatterers. For slabs, another useful quantity is area number density, $n_a = N/S = Nh/V$, where S and h is the area and thickness of the slab that contains N scatterers.

When the slab is infinite in $x - y$ plane and the incident wave is a plane wave as given by Eq. (5.1), the following relation can be obtained:

$$\left\langle \mathbf{F}_j \left(\mathbf{r}_j, s_j, \hat{R}_j \right) \right\rangle_j = e^{-jk_1(\alpha x_j + \beta y_j)} \left\langle \mathbf{F}_j \left(z_j \hat{z}, s_j, \hat{R}_j \right) \right\rangle_j .$$

Equation (5.20) becomes

$$\langle \mathbf{E}^s(\mathbf{r}) \rangle = \frac{n_a}{h} \int\limits_{V_j} d\mathbf{r}_j \frac{e^{-jk_1 R_j}}{R_j} e^{-jk_1(\alpha x_j + \beta y_j)} e^{-jk_1 \hat{R}_{jz} z_j} \int\limits_{s_j} ds_j p(s_j) \left\langle \mathbf{F}_j \left(z_j \hat{z}, s_j, \hat{R}_j \right) \right\rangle_j \tag{5.21}$$

The integral in Eq. (5.21) with respect to x_j and y_j can be evaluated by the method of stationary phase [52]. The result is

$$\langle \mathbf{E}^s(\mathbf{r}) \rangle \cong \frac{2\pi n_a j}{-k_1 \sqrt{(1-\alpha^2)(1-\beta^2)}} e^{-jk_1(\alpha x + \beta y + \gamma z)} \mathbf{F}_c \left(\hat{R}_{js} \right), \tag{5.22}$$

where

$$\mathbf{F}_c \left(\hat{R}_{js} \right) = \int_0^{-h} \frac{dz_j}{h} \int\limits_{s_j} ds_j p(s_j) \left\langle \mathbf{F}_j \left(z_j \hat{z}, s_j, \hat{R}_{js} \right) \right\rangle_j , \tag{5.23}$$

$\hat{R}_{js} = (\alpha, \beta, \gamma) = \hat{k}^{inc}$. $\mathbf{F}_c \left(\hat{R}_{js} \right)$ is the conditionally configurationally averaged scattering amplitude in $\hat{R}_{js}$ direction, which is along the direction of $\hat{k}^{inc}$. In general, it can only be determined numerically.

The effective transmission coefficient matrix for a composite slab as shown in fig. 5-1 is defined as

$$T_c = \frac{\mathbf{E}^{inc}\left(-h\hat{z}\right) + \left\langle \mathbf{E}^s\left(\mathbf{0}\right)\right\rangle_c}{\mathbf{E}^{inc}\left(-h\hat{z}\right)}, \tag{5.24}$$

$$T_x = \frac{\left\langle \mathbf{E}^s\left(\mathbf{0}\right)\right\rangle_x}{\mathbf{E}^{inc}\left(-h\hat{z}\right)}, \tag{5.25}$$

where the subscripts c and x mean the co-polarized and cross-polarized components, respectively.

The reflection coefficient of the same composite slab can also be obtained in the same way by assuming that an incident wave illuminate the composite slab from above. Equation (5.22) becomes

$$\left\langle \mathbf{E}^s\left(\mathbf{r}\right)\right\rangle \cong \frac{2\pi n_a j}{-k_1\sqrt{\left(1-\alpha^2\right)\left(1-\beta^2\right)}} e^{-jk_1(\alpha x+\beta y-\gamma z)}\mathbf{F}_c\left(\hat{R}_{js}\right), \tag{5.26}$$

where $\hat{R}_{js} = (\alpha, \beta, -\gamma)$. The reflection coefficient is given by

$$R_{x/c} = \frac{\left\langle \mathbf{E}^s\left(\mathbf{0}\right)\right\rangle_{x/c}}{\mathbf{E}^{inc}\left(-h\hat{z}\right)}, \tag{5.27}$$

The effective permittivity of the composite slab can be calculated after the transmission coefficients are obtained. Considering the composite slab to be homogeneous with effective relative permittivity ε_e and thickness h, the transmission coefficient is

$$T = \frac{T_{e,1}T_{1,e}e^{-jk_{e,z}h}}{1 - R_{1,e}^2 e^{-2jk_{e,z}h}}, \tag{5.28}$$

where $R_{i,j}$ and $T_{i,j}$ are the Fresnel reflection and transmission coefficients for wave propagating from medium i to medium j. $k_{e,z}$ is the z component of the wave vector in the effective medium. $R_{i,j}$, $T_{i,j}$ and $k_{e,z}$ are functions of ε_e. By equating Eq. (5.24) or (5.25) with Eq. (5.28), we can obtain the effective relative permittivity, ε_e, of the composite slab. ε_e may be tensor.

5.1.2 Theoretical Validation

The formulation above is applicable to composite slabs with inclusions of arbitrary shapes. Here, we consider composite slab with small dielectric spherical inclusions at low concentration. It is presented here to verify the above formulation, and to serve as a demonstration of how the formulation is applied to characterize composite materials.

Analytical results for the FSA of small dielectric spheres are available. We assume that the concentration of the spheres is very low such that the mutual coupling between scatterers is negligible, and the spheres have relative permittivity very close to that of the host medium. In this case, the forward scattering amplitude of a sphere $\mathbf{F}\left(\mathbf{0},\hat{z}\right)$ can be analytically obtained as

$$\mathbf{F}\left(\mathbf{0},\hat{z}\right)=k_0^2\frac{\varepsilon_s-1}{\varepsilon_s+2}a^3\hat{x}, \tag{5.29}$$

where ε_s and a are the relative permittivity and the radius of the spheres, respectively. Substitute Eq. (5.29) into Eqs. (5.22) and (5.24), we have

$$T=1-jk_0\frac{3hc}{2}\frac{\varepsilon_s-1}{\varepsilon_s+2}, \tag{5.30}$$

where c is the volume concentration of spheres. Given the assumption that the effective permittivity is very close to that of the host medium, $\varepsilon_e\approx 1$. Equation (5.28) can be simplified to

$$T=e^{-jk_0\left(\sqrt{\varepsilon_e}-1\right)h}. \tag{5.31}$$

The corresponding approximate effective permittivity of the composite slab is therefore

$$\varepsilon_e=1+3c\frac{\varepsilon_s-1}{\varepsilon_s+2}+\frac{9c^2}{4}\left(\frac{\varepsilon_s-1}{\varepsilon_s+2}\right)^2. \tag{5.32}$$

Equation (5.32) is in fact the low concentration approximation form of Maxwell-Garnett theory [11]. The comparison is shown in Fig. 5-2, which clearly confirms

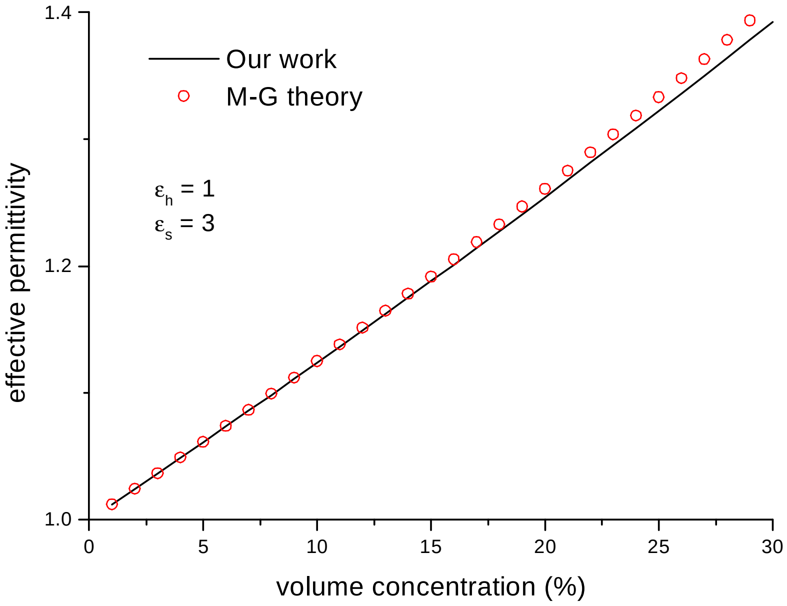

Figure 5-2: Effective permittivity of composite material of homogeneous dielectric spheres.

the good agreement at low concentration.

5.2 Transmission and Reflection Coefficients of Fiber Composite Slabs

Composite materials with random fiber inclusions are normally prepared as slabs. One of the preparing techniques is to spray a mixture of fibers and liquid polymer or some other liquid onto a substrate. The sample is prepared layer by layer. The thickness of each layer is normally in the order of the diameter of the fibers which is much smaller than the length of the fibers. As a result, the fibers are all parallel to the substrate.

Our model considers a random distribution of fibers in a slab region as shown in Fig. 5-3. The slab is arranged to be parallel to the $x-y$ plane and extends to infinity in the x and y directions. The fibers are all parallel to the $x-y$

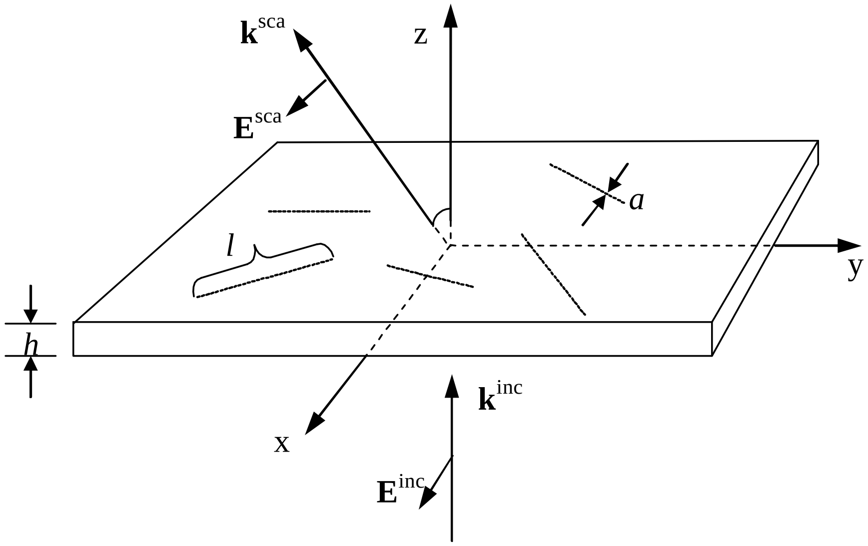

Figure 5-3: Composite slab with random fibers.

plane but otherwise random. It is assumed that the fibers are none magnetic. In addition, the fiber radius are normally smaller than 0.02 times of its length and the wavelength of interest. The circumferential currents are not likely to be excited to give rise to significant artificial magnetic effects.

The computation of the configurationally averaged scattering amplitude $\mathbf{F}_c\left(\hat{R}_{js}\right)$ with Monte Carlo method is discussed in this section. A finite number N_0 of wires are chosen to evaluate $\mathbf{F}_c\left(\hat{R}_{js}\right)$. For a fixed configuration of N_0 fibers, the total scattering amplitude $\mathbf{F}\left(\hat{R}_{js}\right)$ is

$$\mathbf{F}\left(\hat{R}_{js}\right) = -j\omega\mu_1 \sum_{j=1}^{N_0} \left[e^{-jk_1\hat{R}_{jz}z_j} A_j^{TE}\left(\hat{R}_j\right)\hat{\phi}_1 + e^{-jk_1\hat{R}_{jz}z_j} A_j^{TM}\left(\hat{R}_j\right)\hat{\theta}_1 \right], \tag{5.33}$$

where all the quantities are defined in the previous section. Note that $A_j^{TE}\left(\hat{R}_j\right)$ and $A_j^{TM}\left(\hat{R}_j\right)$ can be calculated after the current distributions on the fibers are known. The averaged scattering amplitude is simply given by

$$\mathbf{F}'\left(\hat{R}_{js}\right)=\frac{\mathbf{F}\left(\hat{R}_{js}\right)}{N_0}. \tag{5.34}$$

The block diagram of the Monte Carlo calculation process is shown in Fig. 5-4. After initializing the Monte Carlo simulation, the program goes into the Monte Carlo simulation. A random distribution of N_0 wires according to a prescribed concentration is generated first. Then, the current distributions on all wires are obtained using MoM and the averaged scattering amplitude of the N_0 wires $\mathbf{F}_i\left(\hat{R}_{js}\right)$ is calculated according to Eq. 5.34. A minimum number of Monte Carlo steps $i_{\min}$ is required to be finished before going to the next step where the mean value $\overline{\mathbf{F}}_i\left(\hat{R}_{js}\right)$ of all $\mathbf{F}_{m=1,\cdots,i}\left(\hat{R}_{js}\right)$ obtained so far is calculated by

$$\overline{\mathbf{F}}_i\left(\hat{R}_{js}\right)=\frac{1}{i}\sum_{m=1}^{i}\mathbf{F}_m\left(\hat{R}_{js}\right).$$

The absolute difference $\left|\overline{\mathbf{F}}_i\left(\hat{R}_{js}\right)-\overline{\mathbf{F}}_{i-1}\left(\hat{R}_{js}\right)\right|$ is used to check the convergence of the Monte Carlo simulation. When the absolute difference is smaller than a preset tolerance, $\overline{\mathbf{F}}_i\left(\hat{R}_{js}\right)$ is taken to be the configurationally averaged scattering amplitude $\mathbf{F}_c\left(\hat{R}_{js}\right)$, which will be used in the calculation of transmission or reflection coefficients by substituting it into Eq. (5.22) and then into Eq. (5.24), (5.25) or (5.27), respectively.

The numerically calculated $\mathbf{F}_c\left(\hat{R}_{js}\right)$ is a good approximation to the real value provided that N_0 is sufficiently large. The choice of N_0 affects the efficiency and precision of the simulation. Many factors can affect the choice of suitable N_0. This issue is studied and the details are reported in the next section.

For a fixed N_0, the convergence behavior of a Monte Carlo simulation for the transmission coefficients of composite slabs with highly conductive, insulated fibers is shown in Fig. 5-5. The number concentration is 4 cm^{-2}. The simulated sample contains $N_0 = 40$ fibers with length 10 mm and diameter 0.1 mm. At

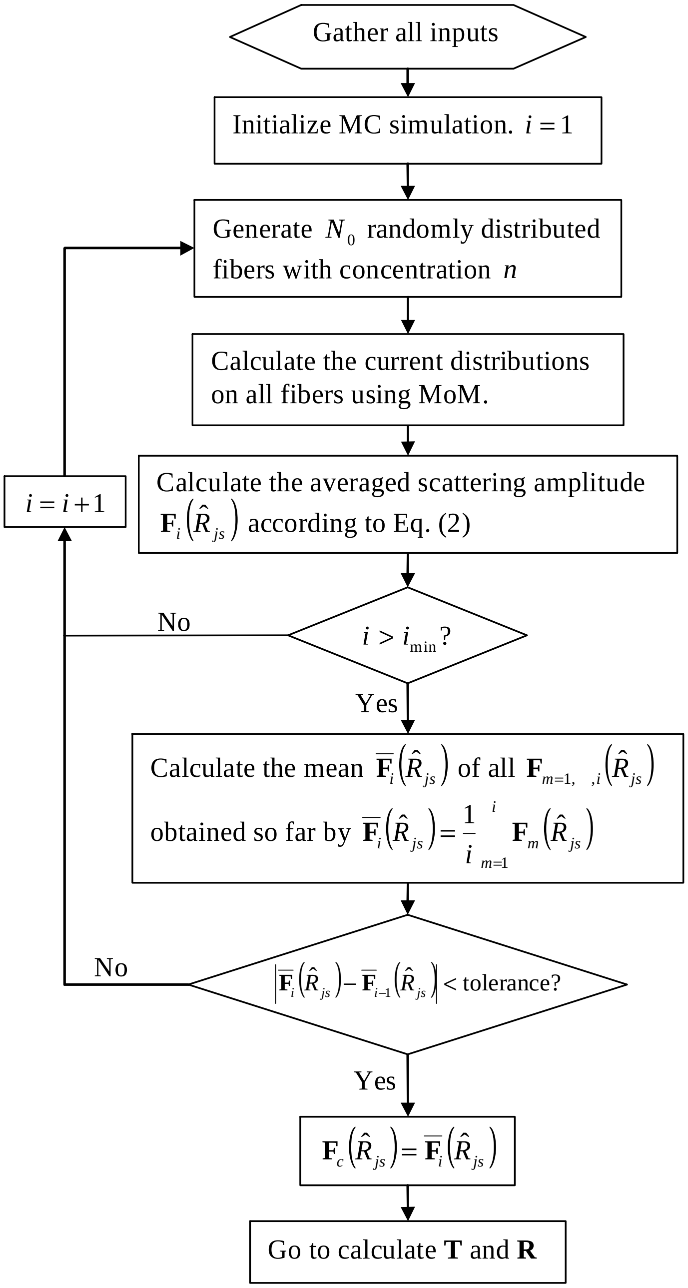

Figure 5-4: Block diagram of Monte Carlo simulation for the configurationally averaged forward scattering amplitude.

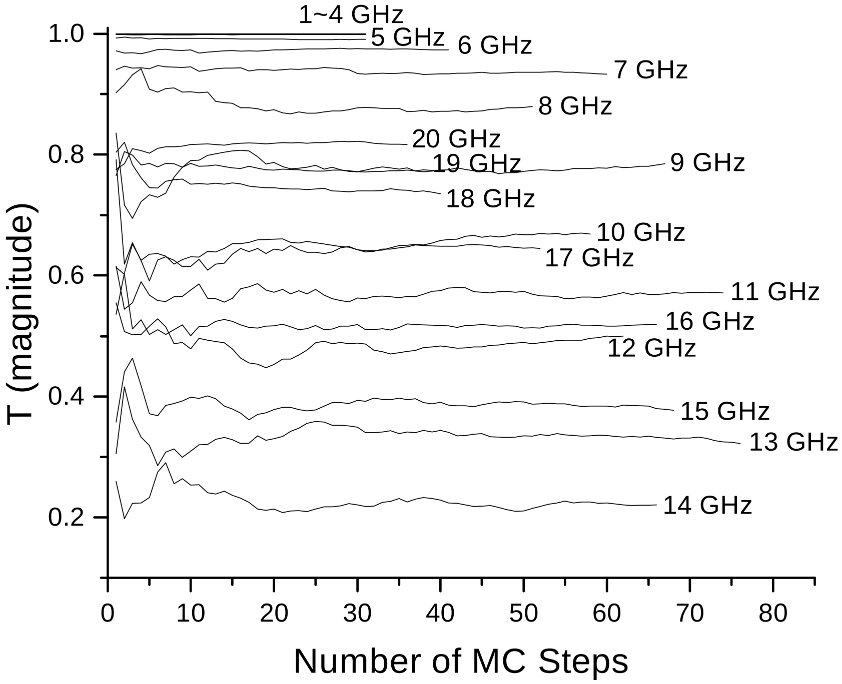

Figure 5-5: Convergence behavior of Monte Carlo simulation for transmission coefficients T. (Sample series #1, $n_c = 4$ cm^{-2}, 40 fibers are used.)

least 30 Monte Carlo steps are carried out for all frequencies.

5.3 The Issue of Sample Size for Fiber Composite Simulation

The approximation introduced into the method developed in the last chapters is the truncation of the slab to a finite transverse extent in modeling the propagation of EM wave through a slab of infinite extent. The interactions among inclusions in the infinite slab are approximated by that in the finite slab. As the transverse dimension of the finite slab increases, the result obtained is expected to approach that of the infinite slab. However, a large slab requires significantly more computational resources. Therefore, it is important to determine a minimal size in order to save computation time without compromising on the accuracy.

Tapered incident wave is frequently used in numerical simulation of the scattering from truncated rough surfaces [10]. It is used to avoid the excitation of current near the edge of a truncated rough surface. Therefore the simulation error due to the truncation can be reduced. In practice, the beam size of the tapered incident wave (normal incidence) has to be in the order of wavelength. The minimal dimension of the truncated sample has to be about 10 times larger than the beam size in order for the incident wave decay sufficiently at the sample edge. If such a big sample has to be used in simulating composite slabs with practical concentration of inclusions, the large number of inclusions in the sample makes the computation impossible. Further reduction in sample size without loss of accuracy is necessary.

The current distribution is confined in the conducting fibers in composite materials. It is continuous within one or a few contacted fibers if the fiber concentration is below the percolation threshold. This is different from the current distribution in rough surfaces. The fiber composite slab can be truncated without cutting fibers by deciding whether a fiber is kept or disposed. The truncation of a fiber composite slab will not truncate the current so abruptly as the truncation of a rough surface do. The truncation error of a fiber composite slab is mainly caused by the change of environment experienced by the fibers near the sample edge. It is studied numerically and reported in the following sections.

The truncated fiber composite slabs used in our simulation are much smaller than that required for the simulation with a tapered incident wave. As a result, tapered incident wave does not help to reduce the truncation error in our case. Plane incident wave is used in all the simulations.

Nguyen and Geneviève [26] analyzed fiber filled composites based on numerical simulation. For a given frequency, they demonstrated that there is a characteristic homogenization length, beyond which the sample can be considered as “homogenizable". In other words, the numerical results become independent of the sample size when the sample is sufficiently large. Therefore, the character-

Table 5.1: The properties of 4 series of samples

sample series	fiber conductivity $10^6(\Omega\mathrm{m})^{-1}$	control of contacts between fibers
#1	70	insulated
#2	70	bare
#3	0.006	insulated
#4	0.006	bare

istic homogenization length corresponds to our minimal sample size. However, the frequency chosen is quite far from the resonance frequency of the fibers. In reality, the minimal sample size (or the characteristic length) depends strongly on frequency and many other factors, such as the inclusion's shape, conductivity, concentration, electrical contacts among inclusions, host materials, etc.

In this section, we present a detailed study on the effects of inclusion's concentration, conductivity, electrical contacts among inclusions, and frequency on the minimal sample size. Since square samples are used in our simulation, the sample size can be characterized by either the side length L of the sample or the number of fibers N embedded in the sample. They are related to each other by the 2D number concentration n_c of fibers by:

$$L = \sqrt{N/n_a} \tag{5.35}$$

Identical fibers are randomly distributed in a finite slab in accordance to a prescribed concentration n_a. All fibers are arranged randomly but parallel to the slab surface (see Fig. 5-3).

The fibers are of length l = 10 mm and diameter a = 0.1 mm. Numerical results for four series of samples are tabulated as shown in Table 5.1.

5.3.1 Effect of Electrical Contact

The effect of electrical contact between fibers are studied here by comparing the simulated results of sample series #1 and #2 at a fixed concentration of 4 cm^{-2}.

The transmission coefficients of sample series #1 are given in Fig. 5-6. The fibers are assumed to be electrically insulated from each other even though they have physical contacts. Different curves correspond to different number of fibers used in the simulation. The difference in the magnitude of transmission coefficient given by the curves reduces as the number of fibers increases. It is noted that the difference between the results obtained using 40 and 130 fibers is less than 0.05 or 5% (maximum magnitude of T is 1). Samples with intermediate number of fibers between 40 and 130 had also been simulated. All results fall within 5% of that given by 130 fibers, but are not shown here. Hence, the minimal sample size, which gives less than 5% error, has to contain about 40 fibers.

Each of the transmission coefficient curves shows a dip at about 14 GHz, which is due to the resonance of the fibers. The resonance dip broadens as the number of fibers increases from 10 to 130. The modification of the shape of the curves demonstrates the role of interaction among fibers, even though they are not in electrical contact. It is due to the interaction that a proper sample size has to be chosen to obtain a reasonable approximation.

The results for sample series #2 are shown in Fig. 5-7. The fibers are assumed to have perfect electrical contacts if they are in physical contact. This is a simplified model of the bare fiber inclusions. As the number of fibers used in the simulation increases, the results change dramatically at low frequency and near the resonance frequency. The behavior at low frequency is caused by long conducting paths formed among different fibers that are in electrical contact. The longer conducting path leads to a lower resonance frequency, hence more noticeable difference at low frequency range is observed as compared to the results shown in Fig. 5-6.

The long conducting path enhances the long range interaction strength. As a result, significantly more fibers are needed to obtain reasonable results. In this example, results obtained with 130 fibers differ from that obtained with 150 fibers by less than 5%. Therefore, the minimal sample in this case has to include about

130 fibers in order to achieve errors of less than 5%. Note that only 40 fibers are needed for simulating series #1 samples with the same concentration. Electrical contacts among fibers have changed the minimal sample size dramatically.

In contrast, the electrical contacts are found not to affect the results at high frequency (14 GHz and above) as can be seen from Figs. 5-6 and 5-7.

Results for two limiting cases for electrical contact are shown here. When the electrical contact is not perfect, the minimal sample size will be in between the two limiting cases. In most of the practical cases, the electrical contacts are far from perfect. The minimal sample size is very near the results of insulated case. This is favorable to simulation.

The transmission coefficients for the cross-polarized fields are also shown in Fig. 5-6 and 5-7. The magnitudes of these fields are very small due to the random distribution of fibers.

5.3.2 Effect of Frequency

The simulation error in transmission coefficient, which is defined as the difference between the transmission coefficient and the converged result obtained with the most number of fibers, is plotted with respect to frequency and the number of fibers in Figs. 5-8 and 5-9, for the cases shown in Figs. 5-6 and 5-7, respectively. The transmission coefficient obtained using the most number of fibers are deemed as precise in each case. Different gray scales or labeled curves indicate different errors. The equi-error curves give the minimal sample sizes that can produce results with that error. The fluctuation of the equi-error curves shows clearly the frequency dependence of the minimal sample sizes.

In Fig. 5-8, the larger errors are distributed mainly within $6 - 19$ GHz, which surrounds the resonance frequency of the fiber inclusions. The error is very small outside this frequency range, even if only a few fibers are chosen for simulation.

The frequency dependence changes with different composites. The simulation errors for the series #2 samples shown in Fig. 5-9 are distributed mainly in the range below resonance frequency.

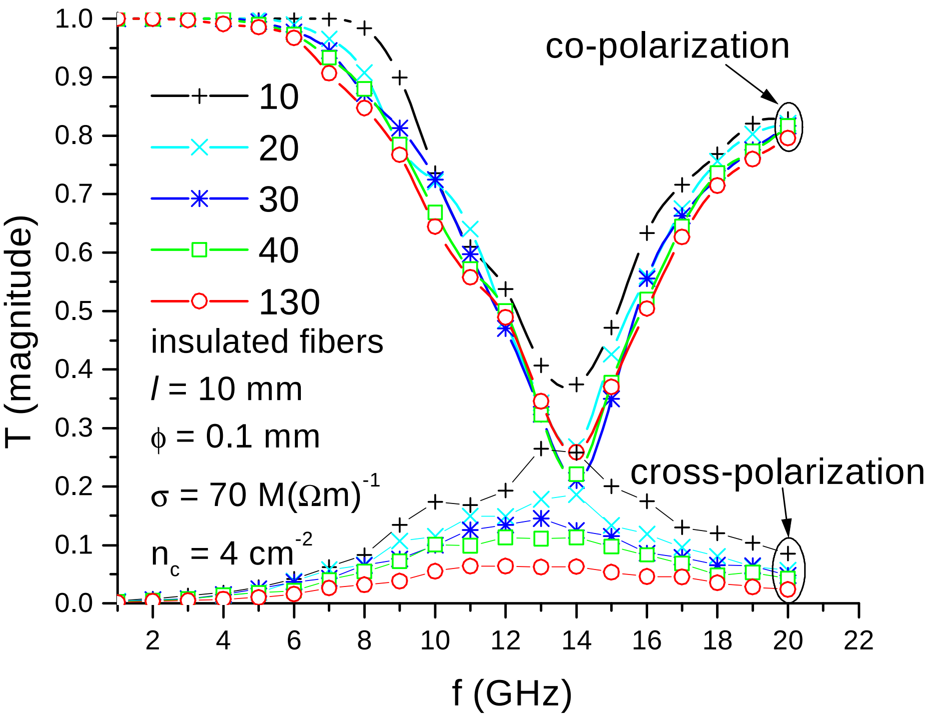

Figure 5-6: Transmission coefficients of sample series #1. Different curves correspond to different numbers of fibers. (Composite slab with highly conductive, insulated fibers, $n_c = 4$ cm^{-2})

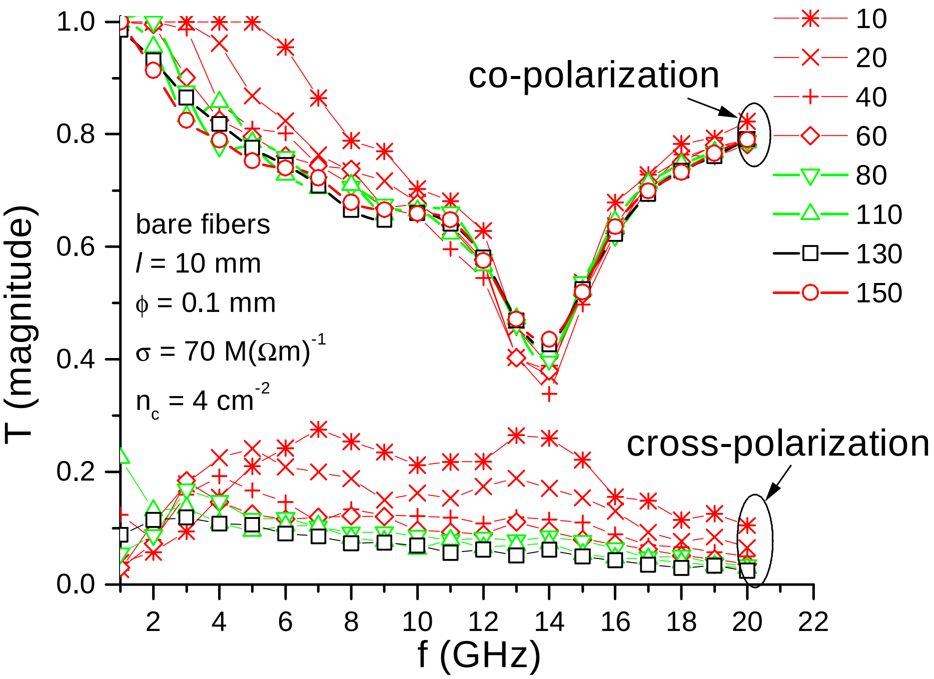

Figure 5-7: Transmission coefficients of sample series #2. Different curves correspond to different numbers of fibers. (Composite slab with highly conductive, bare fibers, $n_c = 4\ \text{cm}^{-2}$)

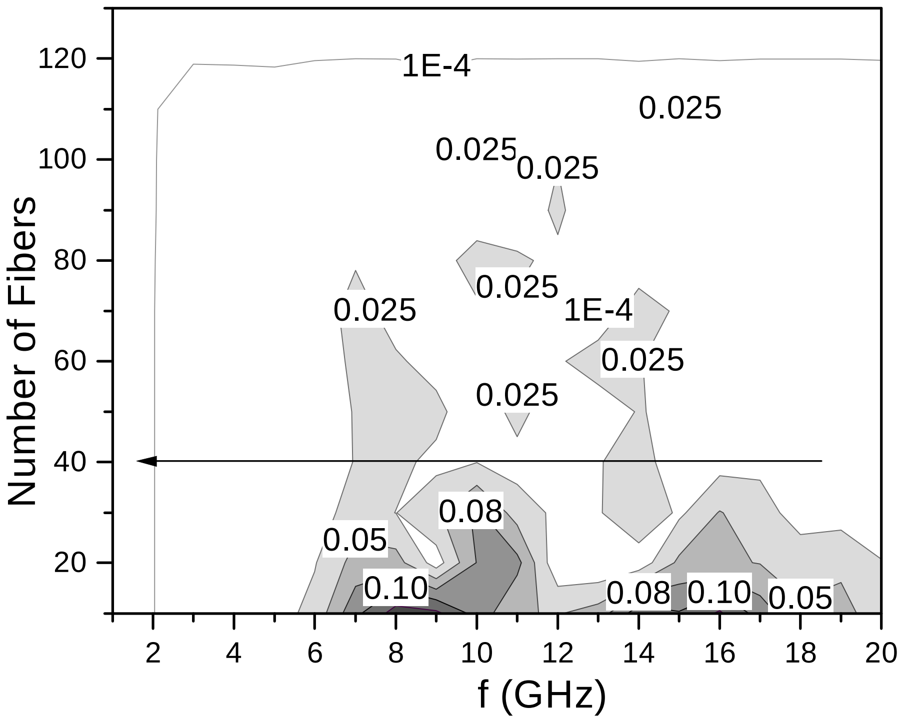

Figure 5-8: Simulation error for sample series #1. (Composite slab with highly conductive, insulated fibers, $n_c = 4$ cm^{-2}. The line indicates the common sample size that gives simulation error below 5% in the whole simulated frequency range.)

The Monte Carlo simulation results shown in Fig. 5-5 also indicate the frequency dependency. More Monte Carlo iterations are needed near the resonance frequency.

5.3.3 Effect of Concentration

The previous results have shown that the minimal sample size is strongly frequency dependent. In the following, the effect of fiber concentration on the minimal sample size over $1-20$ GHz is studied. For simplicity, a common minimal sample size is chosen for the band $1-20$ GHz. For example, it comprises 40 and 130 fibers for the cases shown in Fig. 5-8 and Fig. 5-9 (see the arrow-lines in the figures), respectively, so that the error in the simulated results is less than

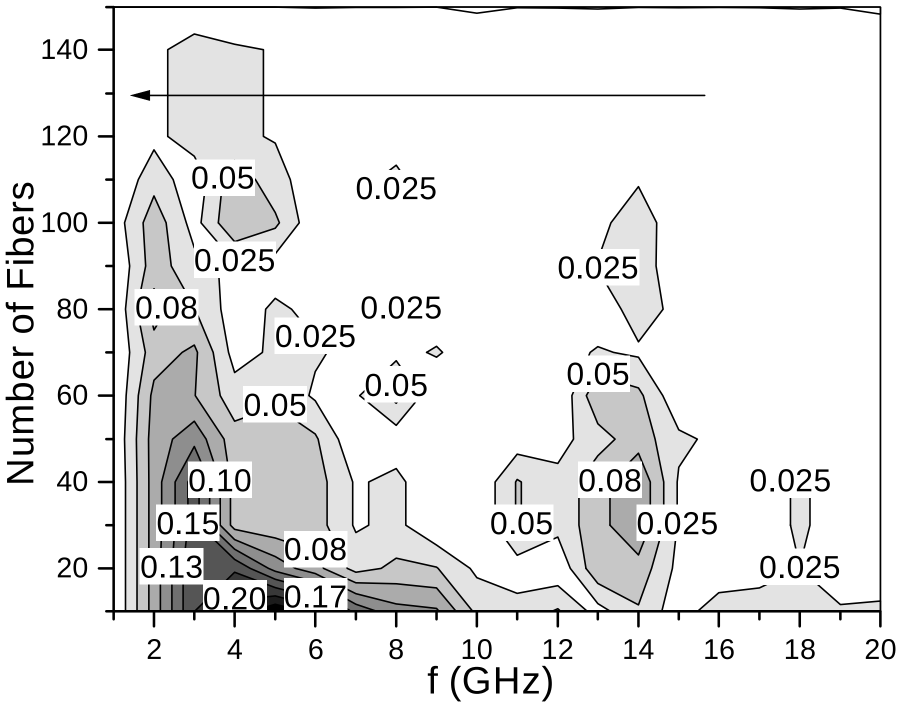

Figure 5-9: Simulation error for sample series #2. (Composite slab with highly conductive, bare fibers, $n_c = 4$ cm^{-2}. The line indicates the common sample size that gives simulation error below 5% in the whole simulated frequency range.)

5%.

Figures 5-10 and 5-11 show the relation between the minimal sample sizes and the concentration of fibers for sample series #1 − #4. Fig. 5-11 is a mapping from Fig. 5-10 using Eq. (5.35). In Fig. 5-10, the results for sample series #2 are well fitted using second order polynomial. The second order polynomials are used to fit results below 3 cm^{-2}, and linear functions are used to fit the remainder. The fitting curves are also mapped to Fig. 5-11 using Eq. (5.35).

From Fig. 5-11, it can be observed that the minimal sample side length increases rapidly with fiber concentration for low concentration. All curves becomes flat as the concentration further increases, except for sample series #2, which comprises highly conductive, bare fibers. The largest minimal sample size is about 4.0 cm for sample series #1, 3.0 cm for sample series #3, 3.5 cm for sample series #4. The largest minimal sample sizes provide a guide for future simulation that may be carried out on similar series of samples.

The minimal sample size for sample series #2 does not stabilize over the range of the simulated concentration. Denser composites with highly conductive, bare fibers will need significantly more computational resources.

5.3.4 Effect of Fiber Conductivity

Our simulation shows that the conductivity greatly affects the results. Simulation of composites with less conductive fibers requires smaller sample, as shown in Figs. 5-10 and 5-11.

5.3.5 Effect of Fiber Length

The effect of fiber length on the minimal number of fibers needed for simulation is shown in Fig. 5-12. For the sample with fiber length 3 mm, the resonance frequency is out of the concerned freqeuncy range. The response is very weak within the concerned concentration range. One fiber is enough for the simulation. As the length increases from 6 mm to 12 mm, the resonance frequency

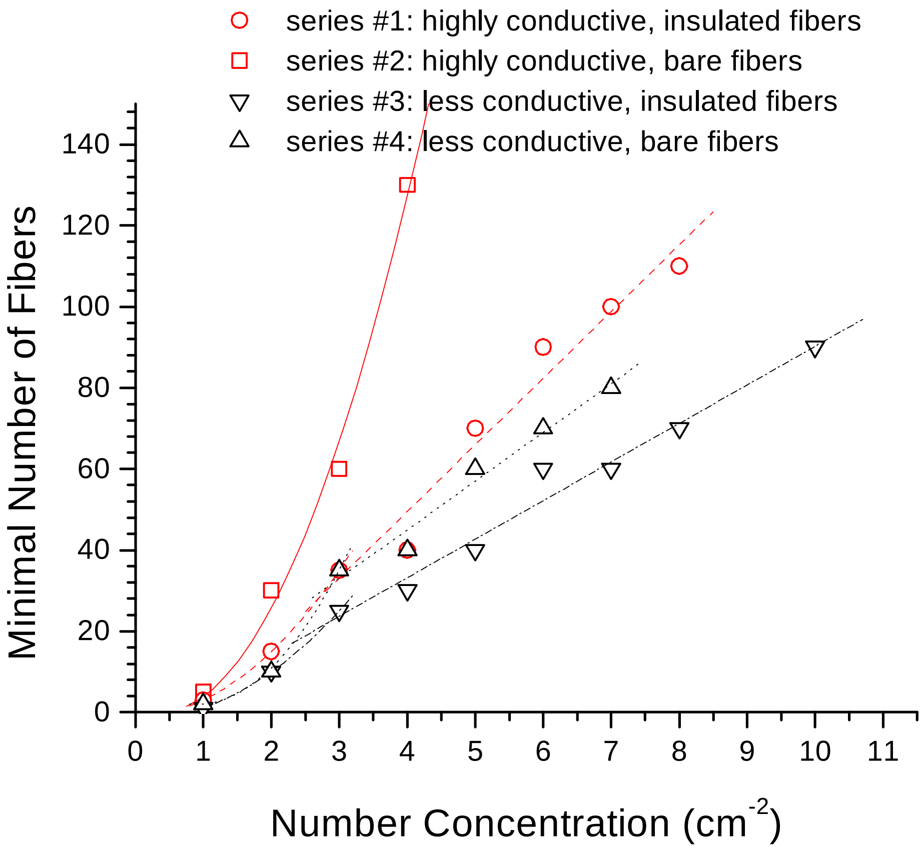

Figure 5-10: Minimum number of fibers with respect to fiber concentration.

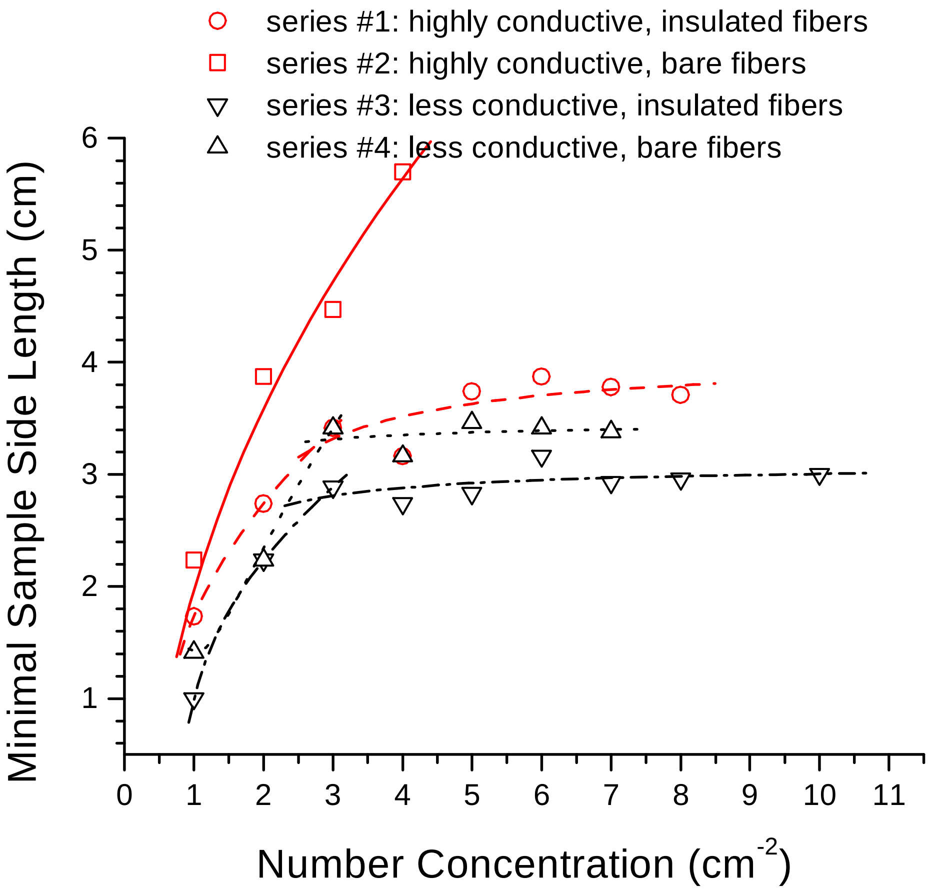

Figure 5-11: Minimal sample side length with respect to fiber concentration.

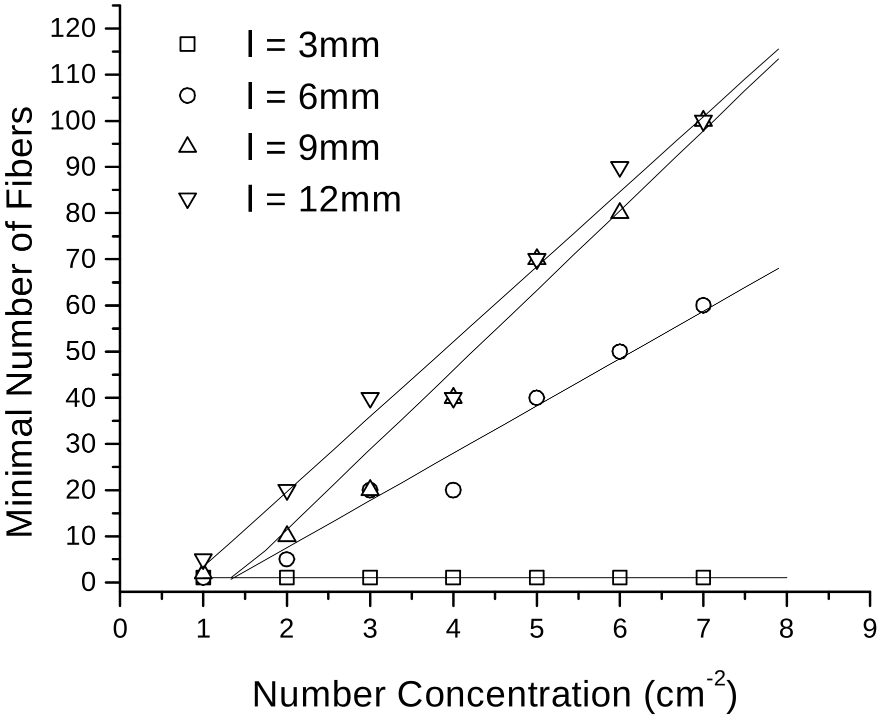

Figure 5-12: Minimum number of fibers with respect to fiber concentration for different fiber length. (Highly conductive, insulated fibers, $a = 0.05$ mm)

moves into the concerned frequency range. The response of the samples becomes stronger. The minimum number of fibers needed for simulation increases. For the samples with fiber length 9 mm and 12 mm, the resonance frequencies are within the concerned frequency range. The difference between the two curves is very small. However, simulation for samples with longer fibers requires slightly more number of fibers. This is because a longer fiber will increase the interaction range compared with a shorter fiber.

5.3.6 Discussions

The effects of inclusion's electrical contact, concentration, conductivity, and wave frequency on the minimal sample size are studied via numerical simulation. A larger minimal sample size is required to simulate composites with higher concentration, better electrical contacts and operating near resonance frequency. The low conductivity of fibers results in smaller minimal sample size required in the simulation. As pointed out in the introduction, the truncation error is caused by the change of environment experienced by the fibers near the sample edge. Part of the interactions between fibers is cut off. Strong and long range interactions cause large truncation error. Fibers with high conductivity and working near resonance frequency carry strong current and therefore cause strong interaction. High concentration of fibers brings the fibers nearer to each other so that the interaction is stronger.

It is also observed that the minimal sample side length stabilizes with increasing concentration, except for composites with bare highly conductive fibers. The stabilized minimal sample side length can be used to determine the number of fibers needed in future simulations of other concentration values. The reason for a stabilized minimal sample size can be explained partially by the decreasing of fiber current magnitude as the fiber concentration increases. This phenomenon is shown in Fig. 5-13. A simple two-dimensional linear thin dipole periodic array with periodicity D_x and D_y (see inset of Fig. 5-13) has been simulated. The fibers are of length 10 mm and radius 0.05 mm. D_y is fixed at 15 mm. The concentration changes with D_x. The current on all array elements has the same phase as long as the normal incidence and forward scattering far field are of interest. The magnitude of the current is shown to decrease with the increasing concentration in the concerned frequency range. The same phenomenon can also be observed in fiber composites. The decreasing of fiber current can reduce the interaction strength and range. Therefore, the increasing of minimal sample side length with increasing concentration can be compensated and stopped by the decreasing of current magnitude.

Electrical contacts between bare fibers form routes for currents to flow from one fiber to another. The interaction is direct and strong. Two limiting cases of electrical contact, i.e. perfect contact and insulation, are simulated. Any composite slabs with intermediate inclusion contact situations will require an intermediate minimal sample size.

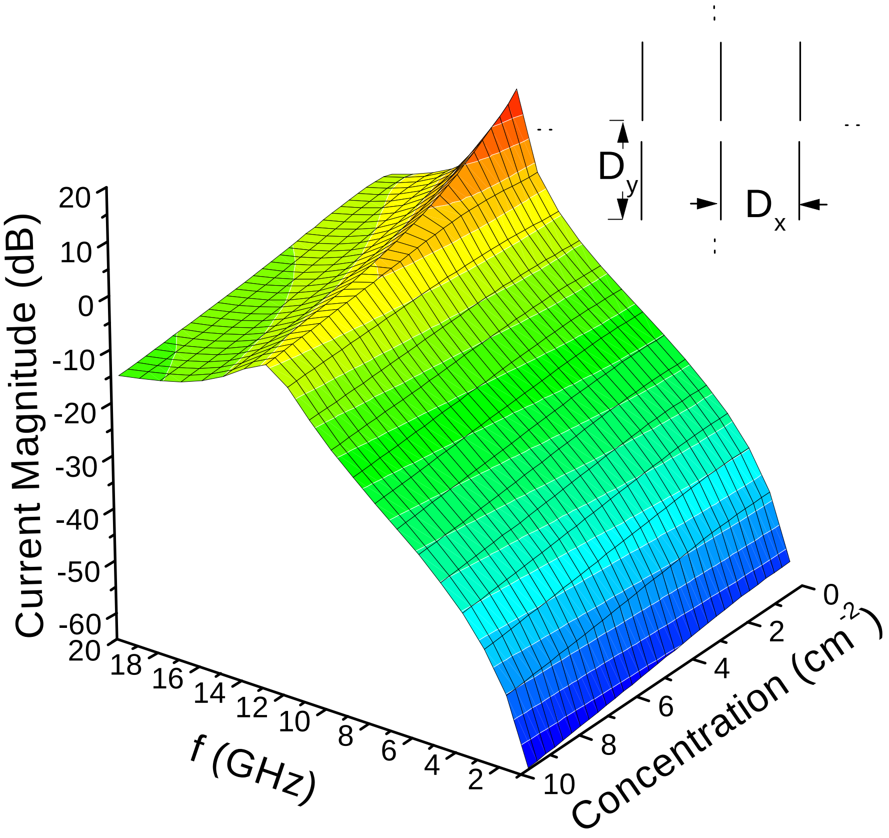

Figure 5-13: Electric current magnitude of an array element. (Highly conductive dipole array, $l = 10$ mm, $a = 0.05$ mm, $D_y = 15$ mm)

5.4 Sample Preparation and Measurement

5.4.1 Sample Preparation

The concentration, length and conductivity of fibers inclusions within a fiber composite are the key factors that can be varied in order to engineer the properties of composites. Electrical contact between fibers is another factor that modifies the properties of composites. Experimental study on the effect of these factors becomes necessary. Although several case studies on these factors have been reported, the published results are either limited or shadowed by uncertainties accompanying the preparation of samples. For example, the experimental results in [24, 26, 94] are confined in low concentration range. Some of them can even be approximated with the dilute limit. Although there are also some experimental results with high concentration of inclusions, such as those presented in [53], these measurements are not suitable to validate numerical simulations because the measured results are complicated by the host material containing a lot of air bubbles, the non-homogeneous distribution of the fibers, the broken or crooked fibers and other factors. No experimental results on electrical contact effect on the properties of composite can be found. Therefore, it is necessary to fabricate and measure more composites in order to investigate the properties of composites and validate numerical results.

The samples are made of 2 pieces of Styrofoam boards that hold some randomly distributed fibers in between them. Each Styrofoam board is of thickness 5 mm and area 20 cm ×20 cm. The relative permittivity of Styrofoam is about 1.05 and relative permeability is 1. Two kinds of fibers, Cu and C, are used as inclusions. The fibers are cut into different lengths. The lengths of the fibers have approximately Gaussian distribution around their mean value due to cut error. The fibers are grouped and labeled in Table 5.2 according to their properties.

To make a composite sample using Cu fibers, the amount of fibers is calculated according to the required concentration. The fibers are then randomly distributed on a piece of paper with a marked area of 20 cm ×20 cm. A piece

Table 5.2: The Properties of Fibers Used in Fabrication of Samples

Label	Material	Length		Diameter	Conductivity
		Mean (mm)	Standard deviation (mm)	(mm)	$10^6\,(\Omega\,\mathrm{m})^{-1}$
Cu-1	Cu	9.98	0.37	0.01	70
Cu-2	Cu	15.20	0.20	0.01	70
Cu-3	Cu	9.70	0.16	0.01	70
C-1	C	5.45	–	0.0035	~ 0.04
C-2	C	14.51	–	0.0035	~ 0.04

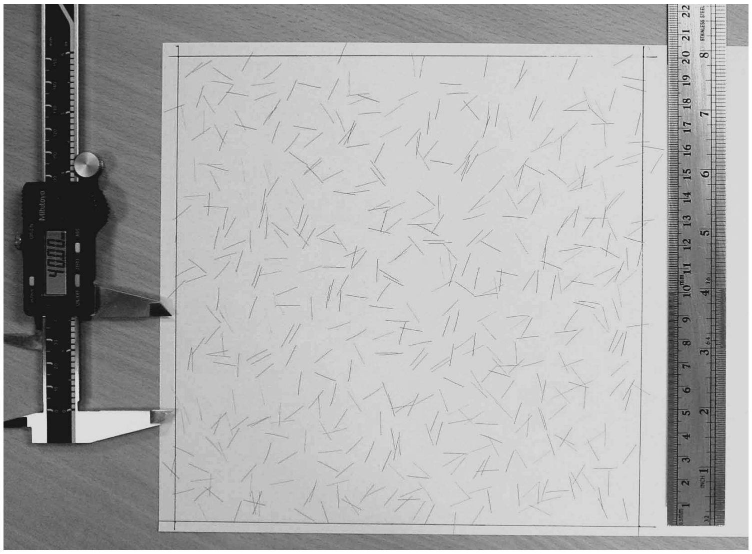

Figure 5-14: The randomly distributed Cu fibers to be sandwiched into Styrofoam boards. Cu-1 fibers are used here.

of Styrofoam board (SB-a), whose dimension is mentioned above and one side of it is covered by a thin layer of paper glue, is stuck onto the area with the randomly distributed fibers. After putting some moderate pressure, the paper can be removed from the Styrofoam board and the fibers are stuck onto it. A few dropped fibers can be taken up manually and stuck back to the Styrofoam board. This method is easy to be implemented and the randomness of the fiber distribution can be monitored and controlled. A prepared sample is shown in Fig. 5-14. In order to prevent the fibers from dropping, another piece of Styrofoam board is used to cover the fibers to form a sandwich sample and the edges are secured with tapes.

Samples with C fibers are difficult to prepare due to the tiny thickness of the fibers. In order to manipulate the C fibers, they are mixed with water and the mixture is poured onto a 20 cm ×20 cm Styrofoam board with elevated boarders, which is of height 5 mm. The fibers are then manually separated and distributed randomly. After the water evaporated, another piece of Styrofoam board is pasted on the sample to prevent the C fibers from dropping or moving.

5.4.2 Measurement and Error Due to Quasi-Randomness

The samples are sent to be measured by the free space method (the details of the free space method can be found in [24, 95] at normal incidence. Oblique incidences are not considered in this thesis. The free space measurement set-up is illustrated as shown in Fig. 1-3. The reflection coefficients can also be measured by this system. In our study, transmission coefficients are sufficient to characterize our samples.

The measured complex transmission coefficients include the effect of the randomly distributed fibers as well as the two Styrofoam boards. In this study, the main interest is the properties of the random fiber layer. Other effects, mainly caused by the Styrofoam boards, should be minimized. Due to the low permittivity of the Styrofoam boards and the simple structure of the sample, the effect of Styrofoam boards on the experimental results can be easily calibrated out without much error and the properties of the composite slab due to the random fiber inclusions alone can be easily studied.

In the free space measurement used in this study, most of the energy of a microwave beam is focused on an area of diameter 15 cm, which is confined by the antennas and the absorbers, while the length of the fibers is in the order of centimeters for applications in the microwave range. It is not preferred to modify the measurement setup. Under such circumstances, the randomness of the fiber distribution causes considerable measurement errors due to the large length of the fibers used in the sample fabrication and the limited size of the illuminated zone of the measurement set-up. It is important to know the magnitude of the

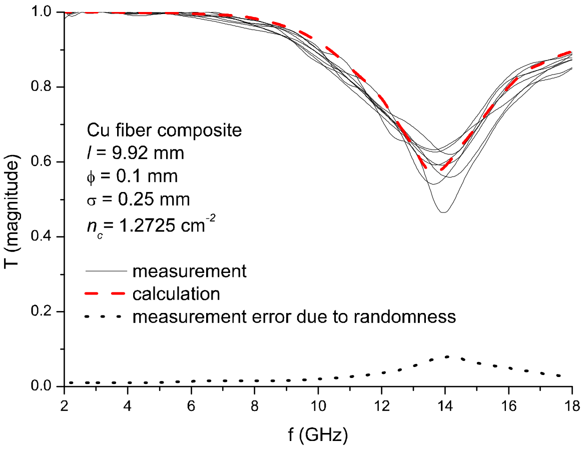

Figure 5-15: Transmission coefficient magnitude of Cu fiber composite. ($\bar{l} = 9.92\,\mathrm{mm}$, $\phi = 0.1\,\mathrm{mm}$, $\sigma_l = 0.25\,\mathrm{mm}$, $n_c = 1.2725\,\mathrm{cm}^{-2}$)

error before interpreting measurement results and making further comparison with calculations.

Four samples containing Cu-1 fibers with mean length $l = 9.98\,\mathrm{mm}$ and standard deviation 0.37 mm are prepared to study the effect of randomness. 509 fibers are randomly distributed in a 20 cm ×20 cm region, which corresponds to a number concentration of $1.2725\,\mathrm{cm}^{-2}$. These fibers have a very thin insulation coating, so there is no electrical contact between them. The transmission coefficients of the four samples are measured for two orthogonal polarizations. Eight solid curves corresponding to the measurement results of the magnitudes and phases of the transmission coefficients are plotted in Figs. 5-15 and 5-16, respectively. The dotted lines in Figs. 5-15 and 5-16 denote the error caused by the random distribution of the fibers and estimated by observing the distribution range of the measured results. It is clearly seen that the error is frequency dependent. The largest error occurs around the resonance frequency of the fibers which is about 14 GHz. This phenomenon can be attributed to the strong response of the induced currents flowing in the fiber near resonant frequency. It renders the measurement results more sensitive to the configuration of the fibers.

The measurement errors shown in Figs. 5-15 and 5-16 are specific to the samples discussed above. It changes with other factors, such as concentration, fiber length and conductivity. It decreases as the concentration of the fibers increases. If the fiber length is chosen such that the resonance is absent in the concerned frequency range, the error is smaller. When the fibers are of low conductivity, the response of the induced current to the incident field is not strong. The error is also smaller. To reduce the measurement error due to the randomness of fibers, wider beam in the free space measurement setup and larger samples have to be used. The manufacturing process should also be monitored to produce random but homogeneous samples.

Results obtained by numerical calculation are presented by the dashed curves in Figs. 5-15 and 5-16. Good agreement between calculation and measurement are observed. To simplify the calculation, it is assumed that the whole space is filled up with Styrofoam. This is valid because the Styrofoam boards used in the experiments are thick and their relative permittivity is near to that of free space.

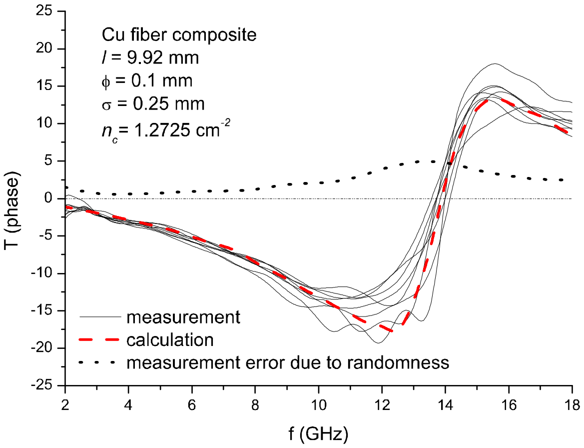

Figure 5-16: Transmission coefficient phase of Cu fiber composite. ($\bar{l} = 9.92\,\mathrm{mm}$, $\phi = 0.1\,\mathrm{mm}$, $\sigma_l = 0.25\,\mathrm{mm}$, $n_c = 1.2725\,\mathrm{cm}^{-2}$)

5.5 Numerical Results

The numerical method proposed above is used to study the properties of different fiber composites. The effects of fiber concentration, electrical contacts between fibers and various other fiber properties on the effective properties of composite materials are studied in details. Several samples are prepared in order to validate the theory.

5.5.1 Effect of Fiber length

The resonance frequency of highly conductive fibers is directly related to the fiber length. Composites with Cu-1 and Cu-2 fiber inclusions are simulated and the results are also shown in Fig. 5-17 as dashed lines. Both samples have number concentration $1.25\,\mathrm{cm}^{-2}$. Good agreements between simulation and experimental results are obtained for both cases. The resonant frequency of the sample with Cu-1 fibers is about 14 GHz and that with Cu-2 fibers is about 9.3 GHz. Both of these resonance frequencies correspond to approximately wavelengths that are twice the lengths of the fiber inclusions. The phase of transmission coefficients shows similar agreements and it is not shown here.

Since the length have Gaussian like distribution, it is interesting to study the effect of standard deviation, σ, of the length distribution on the properties of composite materials. The frequency dependence of the magnitude of transmission coefficients of Cu fiber composites at different standard length deviation are plotted in Fig. 5-18. When the standard length deviation is small, $\sigma < 0.1l$, it mainly changes the magnitude of transmission coefficient curves. A smaller σ results in a sharper resonance peak. When the standard length deviation is large, $\sigma > 0.1l$, it changes not only the shape of the curves, but also the position of the curves. A larger σ shifts the peak value of the resonance peak to lower frequency. The widening of resonance peak as σ increases is because the resonance frequency of a highly conductive thin wire is determined mainly by its length. A distributed length corresponds to a distributed resonance frequency.

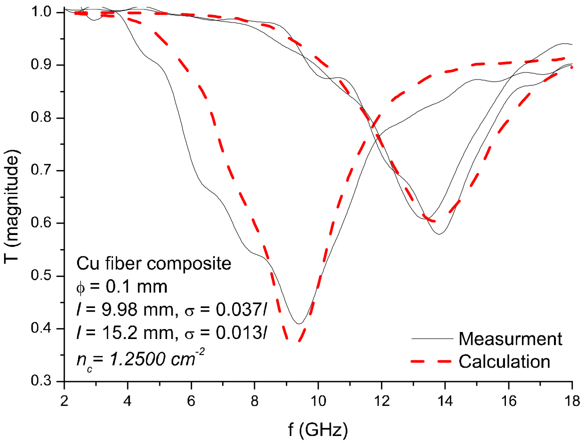

Figure 5-17: Frequency dependence of the magnitude of transmission coefficient of Cu fiber composite. ($\bar{l} = 15.2\,\mathrm{mm}$, $\phi = 0.1\,\mathrm{mm}$, $\sigma_l = 0.013\bar{l}$, $n_c = 5.0000\,\mathrm{cm}^{-2}$)

The amount of energy that can be scattered by fibers depends on their lengths if they are all working at resonance frequency. The longer the fiber is, the more energy it can scatter. As σ increases, the lengths of fibers are distributed more uniformly. But, the longer fibers scatter more energy than the short ones, i.e., resonance effect of the longer are stronger. As a result, the resonance peak of Fig. 5-18 is seen shifting to lower frequency as σ increases.

5.5.2 Effect of Electrical Contact

The effect of electrical contact between fibers is shown in Fig. 5-19. The composites have number concentration $2.545\,\mathrm{cm}^{-2}$. The fiber length is about $10\,\mathrm{mm}$. Numerical calculation is carried out for the limiting cases of perfect electrical contact whenever there is a physical contact between fibers and of non-electrical contact. The calculation result is shown by the curve with cross and circles, respectively, in Fig. 5-19. The perfect electrical contact has reduced the transmission coefficients in the range $2 - 10\,\mathrm{GHz}$. The transmission coefficient in the range $10 - 18\,\mathrm{GHz}$ is increased because the originally stand along fibers that

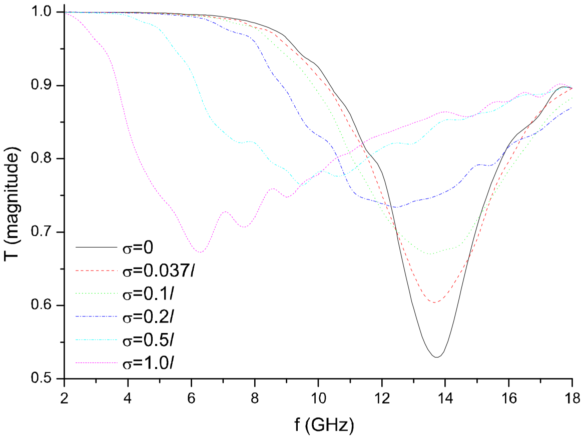

Figure 5-18: Frequency dependence of the magnitude of transmission coefficient of Cu fiber composites at with different length standard deviation. ($\bar{l} = 9.98\,\mathrm{mm}$, $\phi = 0.1\,\mathrm{mm}$, $n_c = 1.25\,\mathrm{cm}^{-2}$)

contribute to the low transmission coefficient in this frequency range is short-circuited out and replaced by larger clusters.

Cu-3 fibers with and without insulation coating are used to fabricate these samples. Three samples are measured in two orthogonal polarizations and the averaged results with respect to the two polarizations are presented. The solid line in Fig. 5-19 represents the transmission coefficient of the first sample prepared with coated Cu fibers. The fibers are electrically insulated from each other by the thin layer of coating. The results agree well with the calculated results for non-electrical contact case. The dashed line in Fig. 5-19 represents the results for another sample prepared with bare Cu fibers. These fibers can have electrical contacts but with varying contact resistance. Comparing with the solid line, which represents the isolated fibers case, the results do not differ much from each other. It means that the electrical contact in the sample with bare fibers is not contributing much to modify the properties of the composite material. In order to obtain a significant effect, a third sample is fabricated in the same way as the second one but with pressures applied on the surface of the sample in order

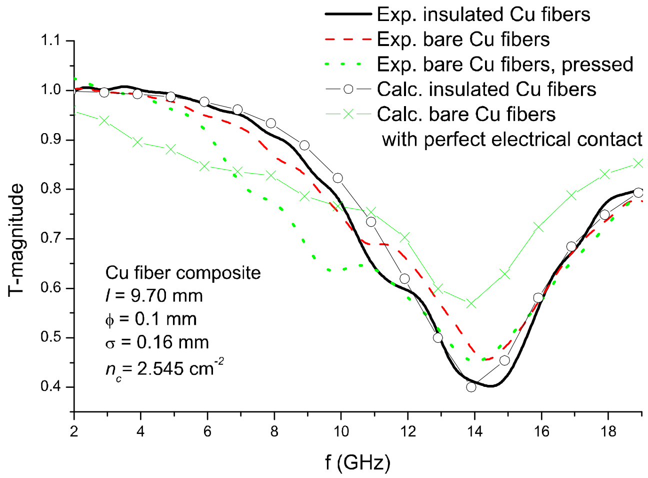

Figure 5-19: Transmission coefficient magnitude of Cu fiber composite. ($\bar{l} = 9.7\,\mathrm{mm}$, $\phi = 0.1\,\mathrm{mm}$, $\sigma_l = 0.017\bar{l}$, $n_c = 2.5450\,\mathrm{cm}^{-2}$)

to decrease the contact resistance. The measurement result for this sample is represented by the dotted curve in Fig. 5-19. A significant change in the shape of the curve can be observed. The transmission coefficient in the frequency range $5 - 11\,\mathrm{GHz}$ drops substantially as compared to the solid or dashed curves. This phenomenon can be attributed exclusively to electrical contacts. When two or more fibers have good electrical contacts, the path for electric current to flow is effectively longer than any single fiber. As a result, the resonance frequency of the composite is spread to lower frequency values. The transmission coefficient at lower frequency is therefore decreased. Fibers with electrical contact form clusters that are larger than a singe fiber and have lower resonance frequency. For a fixed fiber dimension and concentration, the size of the clusters depends on how good the electrical contact is. The better the electrical contact, the larger the cluster is. The limit of the cluster size is determined by the fiber dimension and concentration.

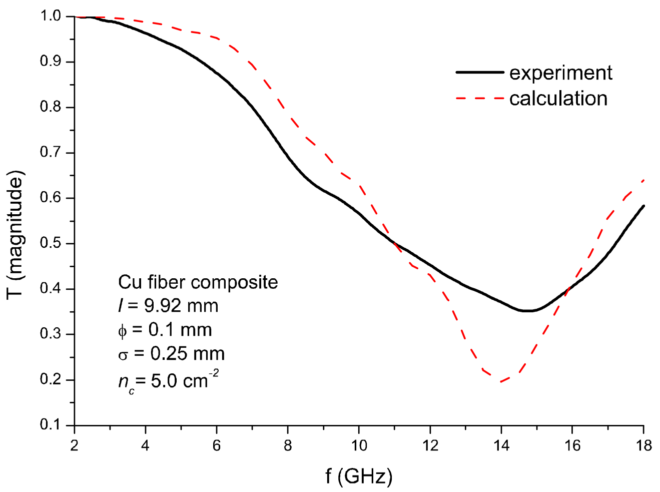

Figure 5-20: Transmission coefficient magnitude of Cu fiber composite. ($\bar{l} = 9.924\,\mathrm{mm}$, $\phi = 0.1\,\mathrm{mm}$, $\sigma_l = 0.025\bar{l}$, $n_c = 5.0000\,\mathrm{cm}^{-2}$)

5.5.3 Effect of Concentration

Cu fiber composites with two concentration values have been simulated in the previous examples as shown in Figs. 5-15, 5-16 and 5-19. Good agreements have been obtained. Now, composites with even higher concentration (number concentration $5.0\,\mathrm{cm}^{-2}$) of Cu-1 fibers are simulated. The corresponding sample is also fabricated and measured. The results are plotted in Fig. 5-20. The simulation shows stronger resonance than experiment. The agreement in this case is not as good as those presented above. At such a high concentration, many fibers are very close to each other. The method of moment with thin wire approximation yields larger error as the concentration goes even higher. The details of the near interaction between wires cannot be captured precisely using thin wire approximation. Removal of thin wire approximation from the method of moment may solve the problem but it is not practical because the computation will be too heavy to be carried out. Other methods are needed to simulate high concentration fiber composites.

More numerical simulations are carried out to study the effect of concentration on the effective properties of composite materials. The results are shown in Figs. 5-21 and 5-22. Cu fiber composites are simulated. The Cu fibers are of identical length, $l = 10\,\mathrm{mm}$, and diameter, $\phi = 0.1\,\mathrm{mm}$. It is assumed that there are no electrical contacts between fibers. With increasing concentration, the resonance dip shown in Fig. 5-21 becomes wider and deeper and the vacillation in the corresponding phase value becomes stronger. The shapes of the transmission curves at different concentration cuts look the same. However, it should be noted that the change of transmission coefficients with respect to concentration at fixed frequency is nonlinear especially near the resonance frequency as shown by Fig. 5-23. This is cause by the interactions among fibers. At very low concentration where the interactions can be neglected, simulation can be carried out by simulating only one fiber. The relation between transmission coefficient and concentration is linear. As the concentration increases, single fiber approximation no longer holds. More fibers have to be used to simulate the effect of interactions between them. The complicated interactions between fibers cause the nonlinear dependence of transmission coefficients on fiber concentration.

5.5.4 Effect of Conductivity

Composites with low conductivity fibers are important due to the loss mechanisms they introduce. Commonly used less conductive fibers are C fibers. Two groups of C fiber composites with different length, 5 mm and 15 mm, are simulated and the results are presented in Figs. 5-24 and 5-25. Each group consists of 3 samples with different number concentration: $15\,\mathrm{cm}^{-2}$, $22\,\mathrm{cm}^{-2}$ and $30\,\mathrm{cm}^{-2}$. No significant resonance can be observed due to the low conductivity of C fibers. The transmission coefficient curves are more spread out evenly in the frequency range $2 - 18\,\mathrm{GHz}$ as compared to those obtained for Cu fiber composites.

C fiber composites are also fabricated and measured in order to compare with simulation results. C-1 fibers are used for the first group and C-2 the second. Reasonable agreements have been obtained for both groups. Since the C fibers

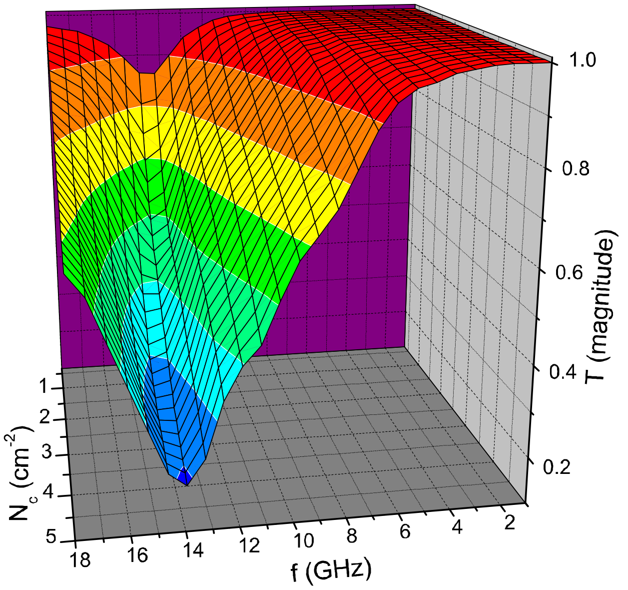

Figure 5-21: The effect of concentration and frequency on the effective transmission coefficient magnitude of composites with Cu fibers. ($\bar{l}$ = 10 mm, $\phi = 0.1$ mm)

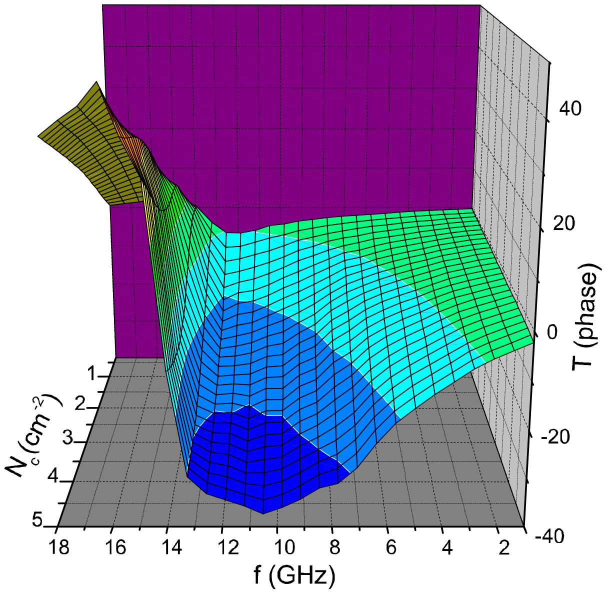

Figure 5-22: The effect of concentration and frequency on the effective transmission coefficient phase of composites with Cu fibers. ($\bar{l} = 10$ mm, $\phi = 0.1$ mm)

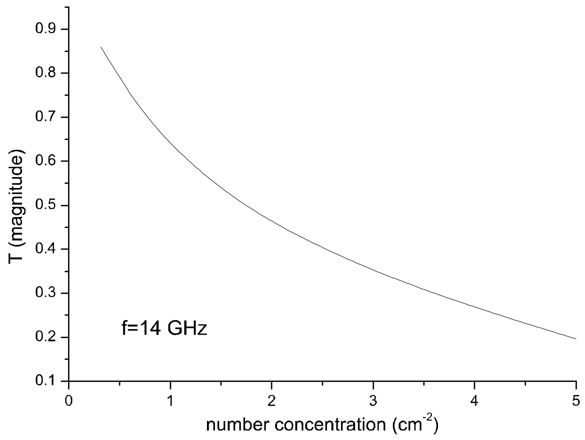

Figure 5-23: Relation between the transmission coefficient magnitude and the number concentration of Cu fiber composites at 14 GHz. ($\bar{l} = 10\,\text{mm}$, $\phi = 0.1\,\text{mm}$)

have no insulation coating, electrical contacts may have some effect on the shape of the transmission coefficient curves. However, numerical simulation results, which are not presented here, for C fiber composites with and without perfect electrical contact show little difference. It suggests that the electrical contacts do not affect composite materials with less conductive fibers so significantly as it does to those with highly conductive fibers.

5.5.5 Considering Stratified Medium

Composite with stratified medium is simulated here. The structure is shown in the inset of Fig. 5-26. It consists of a perfect electrical conducting (PEC) ground, a dielectric layer with thickness $d = 6\,\text{mm}$, relative permittivity 1.05, and a lossy fiber array layer. The array parameters are $D_x = 15\,\text{mm}$ and $D_y = 10\,\text{mm}$. The length of the fibers is $l = 14\,\text{mm}$. In computation, we assume the conductivity is $\sigma = 6 \times 10^{-3}\,(\Omega\,\text{m})^{-1}$. The results are given by the dotted lines in Figs. 5-26 and 5-27. This structure can be easily simulated with the vector spectral-domain method (VSM) [96] which is a well developed and tested method to simulate

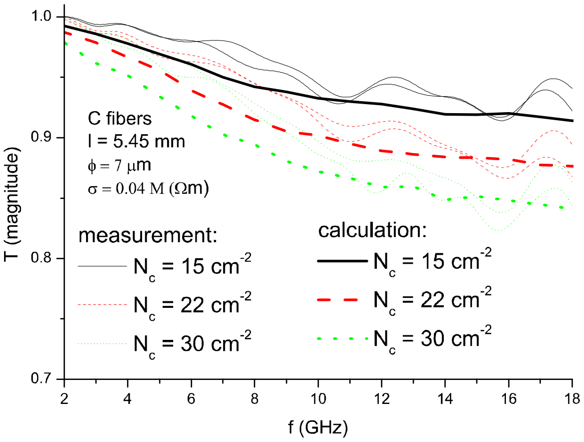

Figure 5-24: Transmission coefficient magnitude of C fiber composite. ($\bar{l} = 5.45\,\mathrm{mm}$, $\phi = 0.007\,\mathrm{mm}$, $\sigma = 0.04 \times 10^6\,(\Omega\,\mathrm{m})^{-1}$)

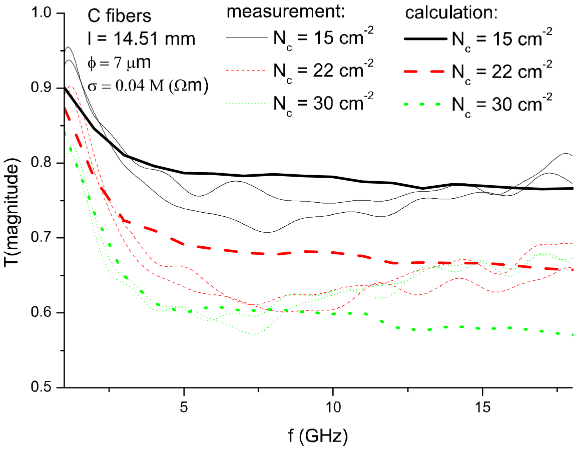

Figure 5-25: Transmission coefficient magnitude of C fiber composite. ($\bar{l} = 14.51\,\mathrm{mm}$, $\phi = 0.007\,\mathrm{mm}$, $\sigma = 0.04 \times 10^6\,(\Omega\,\mathrm{m})^{-1}$)

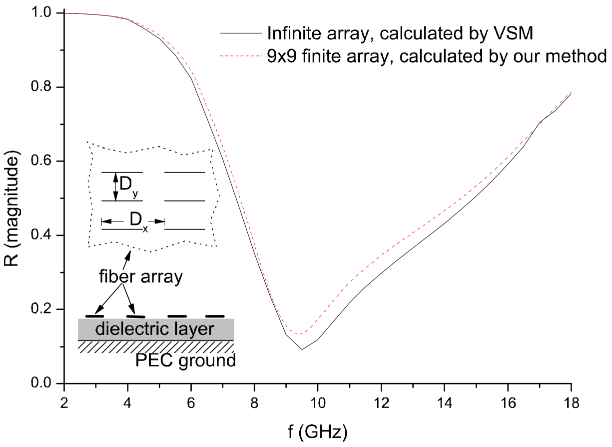

Figure 5-26: Transmission coefficient magnitude of lossy fiber array. ($D_x = 15\,\text{mm}$, $D_y = 10\,\text{mm}$, $\bar{l} = 14\,\text{mm}$, $\phi = 0.1\,\text{mm}$)

frequency selective surfaces. The simulated results are shown by the solid lines in Figs. 5-26 and 5-27. The two results agree with each other with little error. VSM simulates infinite array, while our method simulate finite array on infinite structure. The error between the two methods should vanish as the number of array elements in our finite array increases.

5.6 Conclusions

MoM and Monte Carlo simulation with configurational averaging technique and stationary phase integral method is proposed to calculate the transmission and reflection coefficients of fiber composite material slabs. Results for composite materials with low concentration of small spherical inclusions agree well with those obtained by the Maxwell-Garnett theory. The numerical method is further validated with the measured results for fiber composites with different concentration, electrical contact and fiber inclusion properties. The properties of some types of fiber composite slabs are studied numerically and experimentally.

The minimal sample size is very important for efficient numerical computa-

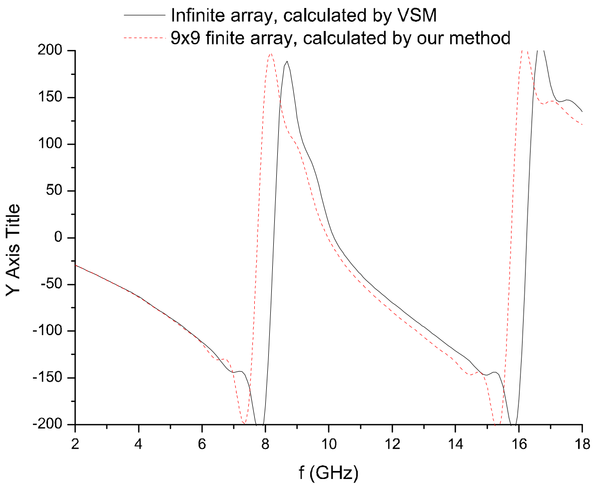

Figure 5-27: Transmission coefficient phase of lossy fiber array. ($D_x = 15\,\text{mm}$, $D_y = 10\,\text{mm}$, $\bar{l} = 14\,\text{mm}$, $\phi = 0.1\,\text{mm}$)

tion. It is related to but not limited by inclusion's conductivity, concentration, electrical contact, and wave frequency. High conductivity and concentration, good electrical contact and near resonance frequency increase the minimal sample. On the other hand, the minimal sample size for simulating composites with less conductive fibers can stay constant for a large concentration range.

The experimental and numerical results may be used to validate other numerical or theoretical methods or as a guidance for composite materials design.

Chapter 6

Conclusions and Future Work

6.1 Conclusions

Efficient methods for simulating the electromagnetic properties of artificial composite materials are developed and validated. The efficiency of solving the equations obtained by TCQ method and the accuracy of the solution are improved by applying a global optimizer, DES. A new numerical method that combines MoM, Monte Carlo and configurational averaging technique is proposed to simulate fiber composites. With these methods, composites with spherical, spheroidal and fiber inclusions are simulated and the following results are obtained.

1. For composites with spherical and spheroidal inclusions, the imaginary part of the effective propagation constant, which characterizes the attenuation of the composite, increases and then decreases as the volume concentration increases. The existence of attenuation peak is numerically confirmed. The attenuation is stronger as the inclusion particles become larger.

2. Different anisotropy is observed for the first time for composite materials with aligned spheroidal inclusion with inclusions of different sizes. Composite materials with smaller aligned spheroidal inclusion particles behave like uniaxial material, while those with larger aligned spheroidal inclusion particles have two separate propagation modes even if the wave propagates

along the particle symmetry axis. In addition, both modes are propagation direction dependent and the dependence relations look similar. This agrees well with the propagation characteristics of plane waves in a general nonmagnetic anisotropic material. The anisotropic properties disappear if the spheroidal inclusions are randomly oriented.

3. It is also observed that the anisotropy becomes stronger as the aspect ratio increases. No other causes of the anisotropy are observed in the simulation. It implies that the shape anisotropy is the main reason for the anisotropy of the composite material.

4. In a fiber composite, electrical contacts between highly conductive fibers modify the shape of the effective transmission coefficient curves by widening the resonance peak and shifting it to lower frequency. The electrical contact has little effect on composites with less conductive fiber inclusions, such as C fibers.

5. The conductivity of fibers can affect the properties of composites significantly. While composites with highly conductive fiber inclusions show strong resonance peaks, composites with less conductive fiber inclusions show no resonance. The transmission coefficients are more uniform in the concerned frequency range.

6. Samples with simple configuration and well controlled fiber distribution are fabricated and measured. These samples are free from many uncertainties, such as complicated host materials, the non-homogeneous distribution of the fibers and the broken or crooked fibers. The measured results are used to validate our numerical results and they can also be used to validate numerical results obtained by other methods.

The simple inclusion shapes, namely, spheres, spheroids and fibers, are good model for many practical arbitrarily shaped inclusions. The method proposed in this thesis can be used more widely to simulate other composites with inclusions of similar shapes. Hopefully, the numerical simulation can help to expedite the design process of new composite materials.

6.2 Future Work

The current methods are still in their primitive stage. There are still much work need to be carried out in order to extend the applicability of these methods.

1. A proper pair correlation functions is essential to the TCQ method. When TCQ method is applied to simulate other inclusion shapes, the corresponding pair correlation function has to be found. It is so hard to find a proper pair correlation function for a given system that the pair correlation function itself is a hot and involved subject that is under study by many dedicated researchers.

2. It is more practically useful to simulate composites with multiple inclusions using the TCQ method. These inclusions may differ in orientation, size, shape or intrinsic properties. It is straight forward to extend the presented TCQ method for composite materials with single inclusion to address composite materials with multiple inclusions. In this case, the eigen equation obtained becomes

   $$\mathbf{Y} = \mathbf{T} \cdot \mathbf{V}' \cdot \mathbf{Y}.$$

   where

   $$\mathbf{T} = \begin{bmatrix} \mathbf{T}^1 & 0 & 0 & 0 \\ 0 & \ddots & 0 & 0 \\ 0 & 0 & \mathbf{T}^i & 0 \\ 0 & 0 & 0 & \ddots \end{bmatrix}$$

and

$$\mathbf{V}' = \begin{bmatrix} \mathbf{V}'^{11} & \cdots & \mathbf{V}'^{1i} & \cdots \\ \vdots & \ddots & & \vdots \\ \mathbf{V}'^{i1} & & \mathbf{V}'^{ii} & \\ \vdots & \cdots & & \ddots \end{bmatrix}.$$

Each inclusion is represented by its T-matrix, $\mathbf{T}^i$. The internal multiple scattering within the ith inclusion is represented by the matrix $\mathbf{V}'^{ii}$, while the mutual coupling between the ith inclusion and the jth inclusion is given by $\mathbf{V}'^{ij}$ $(i \neq j)$.

However, implementing it is never easy. Many challenges show up. For example, the matrices $\mathbf{V}'^{ii}$ and $\mathbf{V}'^{ij}$ $(i \neq j)$ involve pair correlation functions for the same and different inclusions, which are not readily available and hard to be figured out. Further more, the order of matrix $\mathbf{T} \cdot \mathbf{V}'$ is proportional to the number of inclusions. As the number of inclusions increase, finding the eigen values of matrix $\mathbf{T} \cdot \mathbf{V}'$ becomes more and more computationally prohibitive.

3. The thin wire approximation used in the MoM simulation of thin fibers has limited the precision of the method, but simply remove the thin wire approximation will make the computation too complicated to be carried out. Therefore, better approximation or alternative methods other than MoM have to be found.

Bibliography

[1] V. K. Varadan, V. V. Varadan, and Y. H. Pao, “Multiple scattering of elastic waves by cylinders of arbitrary cross section. i. sh waves,” *J. Acoust. Soc. Am.*, vol. 63, no. 5, pp. 1310–1319, 1978.

[2] S. P. Rea, D. Wylie, D. L. E. Orr, and J. McConnell, “Emi shielding of woven carbon fibre composites,” *High Frequency Postgraduate Student Colloquium*, pp. 205–210, Sept. 2004.

[3] K. B. Cheng, S. Ramakrishna, and K. C. Lee, “Electro magnetic shielding effectiveness of copper/glass fiber knitted fabric reinforced poly-propylene composites,” *Composites Part A*, vol. 31, pp. 1039–1045, 2000.

[4] A. Ishimaru and Y. Kuga, “Attenuation constant of a coherent field in a dense distribution of particles,” *J. Opt. Soc. Am.*, vol. 72, no. 10, pp. 1317–1320, 1982.

[5] C. Brosseau and A. Beroual, “Computational electromagnetics and the rational design of new dielectric heterostructures,” *Progress in Materials Science*, vol. 48, no. 5, pp. 373–456, 2003.

[6] A. N. Lagarkov and A. K. Sarychev, “Electromagnetic properties of composites containing elongated conducting inclusions,” *Phys. Rev. B*, vol. 53, no. 10, p. 6318, Mar 1996.

[7] W. Chew, J. Lin, and X. Yang, “An fft t-matrix method for 3d microwave scattering solution from random discrete scatterers,” *Microw. Opt. Tech. Lett.*, vol. 9, no. 4, pp. 194–196, 1995.

[8] M. I. Mishchenko, J. W. Hovenier, and L. D. Travis, Eds., *Light Scattering by nonspherical particles: Theory, Measurements, and Applications.* San Diego: Academic Press, 2000.

[9] L. Tsang, J. A. Kong, K. H. Ding, and C. O. Ao, *Scattering of Electromagnetic Waves - Theories and Applications.* New York: Wiley, 2001.

[10] ——, *Scattering of Electromagnetic Waves - Numerical Simulations.* New York: Wiley, 2001.

[11] T. C. Choy, *Effective Medium Theory-Principles and Applications.* Oxford : Clarendo Press, 1999.

[12] P. Chýlek and V. Srivastava, “Dielectric constant of a composite inhomogeneous medium,” *Phys. Rev. B*, vol. 27, no. 8, pp. 5098–5106, 1983.

[13] V. I. Tatarskii, *The Effects of the Turbulent Atmosphere on Wave Propagation.* US Department of Commerce, Springfield, VA, 1971.

[14] M. A. Suniga and J. A. Kong, “Active remote sensing of random media,” *J. Appl. Phys.*, vol. 51, no. 1, pp. 74–79, 1980.

[15] L. Tsang and J. A. Kong, *Radio Sci.*, vol. 6, p. 303, 1981.

[16] L. Tsang, J. A. Kong, and R. W. Newton, *IEEE Trans. Antennas Propagat.*, vol. 30, p. 292, 1982.

[17] Y. Q. Jin and J. A. Kong, “Strong fluctuation theory for electromagnetic wave scattering by a layer of random discrete scatterers,” *J. Appl. Phys.*, vol. 55, no. 5, p. 1364, 1984.

[18] M. Lax, “Multiple scattering of waves,” *Revs. Modern Phys.*, vol. 23, no. 4, pp. 287–310, 1951.

[19] F. J. H. Roussel, W. C. Chew and W. Tabbara, "Electromagnetic scattering from dielectric and magnetic gratings of fibers - a t-matrix solution," *J. Electromag. Waves Appli.*, vol. 10, no. 1, pp. 109–127, 1996.

[20] F. Wu and K. W. Whites, "Computation of effective permittivity of a 2-d periodic structure by t-matrix algorithm," *Southeastcon '99. Proceedings. IEEE*, pp. 329–332, 1999.

[21] P. R. Siqueira and K. Sarabandi, "T-matrix determination of effective permittivity for three-dimensional dense random media," *IEEE Trans. Antennas Propagat.*, vol. 48, no. 2, pp. 317–327, 2000.

[22] K. K. Karkkainen, A. H. Sihvola, and K. I. Nikoskinen, "Effective permeability of mixtures: numerical validation by fdtd method," *IEEE Trans. Geosci. Remote Sens.*, vol. 38, no. 3, pp. 1303–1308, 2000.

[23] H. Waki, H. Igarashi, and T. Honma, "Estimation of effective permeability of magnetic composite materials," *IEEE Trans. Magn.*, vol. 41, no. 5, pp. 1520–1523, 2005.

[24] L. Liu, S. M. Matitsine, Y. B. Gan, and K. N. Rozanov, "Effective permittivity of planar composites with randomly or periodically distributed conducting fibers," *J. Appl. Phys.*, vol. 98, no. 6, pp. 63 512–63 518, 2005.

[25] K. W. Whites, "Full-wave computation of constitutive parameters for lossless composite chiral materials," *IEEE Trans. Antennas Propagat.*, vol. 43, p. 376, 1995.

[26] T. T. Nguyen and M. M. Geneviève, "Microwave characterization of 2-d random materials: numerical simulations and experiments," *IEEE Trans. Microwave Theory Tech.*, vol. 46, no. 10, pp. 1478–1483, 1998.

[27] W. S. Jou, "The high electromagnetic shielding of woven carbon fiber composites applied to optoelectronic devices," *The 5th Pacific Rim Conference*

on Lasers and Electro-Optics, 2003. CLEO/Pacific Rim 2003., vol. 2, p. 755, 15-19 Dec. 2003.

[28] Y. Ramadin, S. A. Jawad, S. M. Musameh, M. Ahmad, A. M. Zihlif, A. Paesano, E. Martuscelli, and G. Ragosta, "Electrical and electromagnetic shielding behavior of laminated epoxy-carbon fiber composite," *Polymer Int.*, vol. 34, pp. 145–150, 1994.

[29] J. R. Gaier, "Intercalated graphite fiber composites as emi shields in aerospace structures," *IEEE Trans. Electromagn. Compat.*, vol. 34, no. 3, pp. 351–356, 1992.

[30] O. Reynet, A. L. Adenot, S. Deprot, O. Acher, and M. Latrach, "Effect of the magnetic properties of the inclusions on the high-frequency dielectric response of diluted composites," *Phys. Rev. B*, vol. 66, no. 9, pp. 94 412–9420, 2002.

[31] D. P. Makhnovskiy and L. V. Pania, *J. Appl. Phys.*, vol. 93, p. 4120, 2003.

[32] L. V. Panina, S. I. Sandacci, and D. P. Makhnovskiy, *J. Appl. Phys.*, vol. 97, 2005.

[33] H. Gao, W. Yang, K. Min, L. Zha, C. Wang, and S. Fu, "Thermosensitive poly(n-isopropylacrylamide) nanocapsule with controlled permeability," *Polymer*, vol. 46, pp. 1087–1093, 2005.

[34] M. J. Escuti, J. Qi, and G. P. Crawford, "Tunable face-centered-cubic photonic crystal formed in holographic polymer dispersed liquid crystals," *Opt. Lett.*, vol. 28, no. 7, pp. 522–524, 2003.

[35] J. Pendry, A. Holden, D. Robbins, and W. Stewart, *IEEE Trans. Microwave Theory Tech.*, vol. 47, p. 2075, 1999.

[36] J. Pendry, *Phys. Rev. Lett.*, vol. 85, p. 3966, 2000.

[37] ——, *Phys. World*, vol. 14, p. 47, 2001.

[38] D. Smith, W. Padilla, D. Vier, S. Nemat-Nasser, and S. Schultz, *Phys. Rev. Lett.*, vol. 84, p. 4184, 2000.

[39] M. Wiltshire2001, *Science*, vol. 292, p. 60, 2001.

[40] A. Lagarkov and V. Kisel, *Kisel. Phys*, vol. 46, p. 163, 2001.

[41] J. H. Oh, K. S. Oh, C. G. Kim, and C. S. Hong, "Design of radar absorbing structures using glass/epoxy composite containing carbon black in x-band frequency ranges," *Composites, Part B*, vol. 35, pp. 49–56, 2004.

[42] R. C. R. N. M. S. Pinho, M. L. Gregori and B. G. Soares, "Performance of radar absorbing materials by waveguide measurements for x and ku-band frequencies," *European Polymer Journal*, vol. 38, pp. 2321–2327, 2002.

[43] G. Li, G. G. Hu, H. D. Zhou, X. J. Fan, and X. G. Li, "Absorption of microwaves in laixsrxmno3 manganese powders over a wide bandwidth," *J. Appl. Phys.*, vol. 90, pp. 5512–5514, 2001.

[44] S. A. Tretyakov and S. I. Maslovski, "Thin absorbing structure for all incidence angles based on the use of a high-impedance surface," *Microw. Opt. Tech. Lett.*, vol. 38, pp. 175–178, 2003.

[45] K. Matous and G. J. Dvorak, "Optimization of electromagnetic absorption in laminated composite plates," *IEEE Trans. Magn.*, vol. 39, pp. 1827–1835, 2003.

[46] J. Soller, "Weave definitions," *http://www.sollercomposites.com/Weave Definitions.doc.*

[47] J. Baker-Jarvis, E. J. Vanzura, and W. A. Kissick, "Improved technique for determining complex permittivity with the transmission/reflection method," *IEEE Trans. Microwave Theory Tech.*, vol. 38, no. 8, pp. 1096–1103, 1990.

[48] E. Salahun, P. Queffelec, M. L. Floch, and P. Gelin, “A broadband permeameter for ‘in situ’ measurements of rectangular samples,” *IEEE Trans. Magn.*, vol. 37, no. 4, pp. 2743–2747, 2001.

[49] J. D. Jackson, *Classical Electrodynamics*, 3rd ed. New York: John Wiley, 1998.

[50] J. C. Maxwell-Garnett, “Colours in metal glasses and in metal films,” *Phil. Trans. R. Soc. London*, vol. 203, pp. 385–420, 1904.

[51] D. Stroud and F. P. Pan, “Self-consistent approach to electromagnetic wave propagation in composite media: Application to model granular metals,” *Phys. Rev. B*, vol. 17, no. 4, pp. 1602–1610, 1978.

[52] C. F. Bohren and D. R. Huffman, *Absorption and Scattering of Light by Small Particles.* New York: John Wiley, 1983.

[53] A. N. Lagarkov, S. M. Matytsin, K. N. Rozanov, and A. K. Sarychev, “Dielectric properties of fiber-filled composites,” *J. Appl. Phys.*, vol. 84, no. 7, p. 3806, Oct 1998.

[54] A. Sihvola, *Electromagnetic mixing formulas and applications.* London: IEE, 1999.

[55] L. Tsang, J. A. Kong, and R. T. Shin, Eds., *Theory of Microwave Remote Sensing.* New York: John Wiley & Sons, 1985.

[56] L. Tsang, K. H. Ding, S. E. Shih, and J. A. Kong, “Scattering of electromagnetic waves from dense distributions of spheroidal particles based on monte carlo simulations,” *J. Opt. Soc. Am. A*, vol. 15, no. 10, pp. 2660–2669, 1998.

[57] V. V. Varadan, V. K. Varadan, Y. Ma, and W. A. Steele, “Effects of nonspherical statistics on em wave propagation in discrete random media,” *Radio Sci.*, vol. 22, no. 4, pp. 491–498, 1987.

[58] P. C. Waterman, “Matrix formulation of electromagnetic scattering,” *Proc. IEEE*, vol. 53, no. 8, pp. 805–812, 1965.

[59] ——, “Symmetry, unitarity, and geometry in electromagnetic scattering,” *Phys. Rev. D*, vol. 3, no. 4, pp. 825–839, 1971.

[60] R. F. Harrington, *Field Computation by Moment Methods.* New York: IEEE Press, 1993.

[61] J. H. Richmond, “Radiation and scattering by thin-wire structures in a homogeneous conducting medium,” *IEEE Trans. Antennas Propagat.*, vol. 22, p. 365, 1974.

[62] N. P. check, “http://www.nec2.org.”

[63] B. A. Baker and E. T. Copson, *The Mathematical Theory of HuygensŠ Principle*, 2nd ed. Oxford University Press, 1950.

[64] R. F. Harrington, *Time-harmonic Electromagnetic Fields*, 2nd ed. New York: McGraw-Hill, 1961.

[65] A. F. Peterson, S. L. Ray, and R. Mittra, *Computational Methods for Electromagnetics.* New York: IEEE Press, 1998.

[66] R. Storn and K. Price, “Differential evolution - a simple and efficient adaptive scheme for global optimization over continuous spaces,” International Computer Science Insitute, Tech. Rep. TR-95-012, Mar 1995.

[67] A. Qing, “Electromagnetic inverse scattering of multiple two-dimensional perfectly conducting objects by the differential evolution strategy,” *IEEE Trans. Antennas Propagat.*, 2003.

[68] K. A. Michalski, “Electromagnetic imaging of circular-cylindrical conductors and tunnels using a differential evolution algorithm,” *Microw. Opt. Tech. Lett.*, vol. 27, no. 5, pp. 330–334, 2000.

[69] ——, “Electromagnetic imaging of elliptical-cylindrical conductors and tunnels using a differential evolution algorithm,” *Microw. Opt. Tech. Lett.*, vol. 28, no. 3, pp. 164–169, 2001.

[70] A. Qing, X. Xu, and Y. B. Gan, “Anisotropy of composite materials with inclusion with orientation preference,” *IEEE Trans. Antennas Propagat.*, vol. 53, no. 2, pp. 737–744, 2005.

[71] S. Yang, Y. B. Gan, and A. Qing, “Sideband suppression in time modulated linear arrays by the differential evolution algorithm,” vol. 1, no. 9, pp. 173–175, 2002.

[72] J. J. H. Wang, *Generalized Moment Methods in Electromagnetics.* New York: Wiley, 1991.

[73] B. D. Popović, M. B. Dragović, and A. R. Djordjević, *Analysis and Synthesis of Wire Antennas.* New York: Research Studies Press, 1982.

[74] J. Moore and M. A. West, “Simplified analysis of coated wire antennas and scatterers,” *IEE Proc. Microw. Antennas Propag.*, vol. 142, no. 1, 1995.

[75] A. P. check, “http://home.att.net/ ray.l.cross/asap/.”

[76] S. A. Schelkunoff and H. T. Friis, *Antennas-Theory and Practice.* John Wiley: New York, 1952.

[77] L. L. Foldy, “The multiple scattering of waves,” *Phys. Rev.*, vol. 67, no. 3 & 4, pp. 107–119, 1945.

[78] V. V. Varadan and V. K. Varadan, “Multiple scattering of electromagnetic waves by randomly distributed and oriented dielectric scatterers,” *Phys. Rev. D*, vol. 21, no. 2, pp. 388–394, 1980.

[79] D. A. McQuarrie, *Statistical Mechanics.* Sausalito, California: University Science Books, 2000.

[80] O. R. Cruzan, “Translational addition theorems for spherical vector wave functions,” *Q. Appl. Math.*, vol. 20, no. 1, pp. 33–40, 1962.

[81] A. Qing, X. Xu, and Y. B. Gan, “Scalar and vector spherical wave functions translational addition theorems and applications,” Temasek Laboratories, National University of Singapore, Tech. Rep., August 2002.

[82] J. A. Stratton, *Electromagnetic Theory.* New York: McGRAW-HILL, 1941.

[83] P. C. Waterman, “Scattering by periodic surfaces,” *J. Acoust. Soc. Am.*, vol. 57, pp. 791–802, 1975.

[84] W. H. Press, S. A. Teukolsky, W. T. Vetterling, and B. P. Flannery. Cambridge University Press, 1992.

[85] J. K. Percus and G. J. Yevick, “Analysis of classical statistical mechanics by means of collective coordinates,” *Phys. Rev.*, vol. 110, no. 1, pp. 1–13, 1958.

[86] M. S. Wertheim, “Exact solution of the percius-yevick integral equation for hard spheres,” *Phys. Rev. Lett.*, vol. 10, no. 8, pp. 321–323, 1963.

[87] G. J. Throop and R. J. Bearman, “Numerical solution of the percus-yevick equation for the hard-sphere potential,” *J. Chem. Phys.*, vol. 42, no. 7, pp. 2408–2411, 1965.

[88] J. S. Rowlinson, “Self-consistent approximation for molecular distribution function,” *Mol. Phys.*, vol. 9, pp. 217–227, 1965.

[89] A. R. Edmonds, *Angular Momentum in Quantum Mechanics.* Princeton, New Jersey: Princeton University Press, 1960.

[90] M. Born and E. Wolf, *Principles of Optics*, 6th ed. Cambridge: Cambridge University Press, 1997.

[91] W. C. Chew, "A derivation of the vector addition theorem," *Microw. Opt. Tech. Lett.*, vol. 3, no. 7, pp. 256–260, 1990.

[92] R. F. Harrington, *Time-harmonic Electromagnetic Fields.* New York: Wiley-Interscience, 2001.

[93] W. C. Chew and S. Chen, "Response of a point source embedded in a layered medium," *IEEE Trans. Antennas Wireless Propagat. Lett.*, vol. 2, pp. 254–258, 2003.

[94] X. Xu, A. Qing, Y. B. Gan, and Y. P. Feng, "Effective properties of fiber composite materials," *J. Electromag. Waves Appli.*, vol. 18, no. 5, pp. 649–662, 2004.

[95] S. M. Matitsine, K. M. Hock, L. Liu, Y. B. Gan, A. N. Lagarkov, and K. N. Rozanov, *J. Appl. Phys.*, vol. 94, p. 1146, 2003.

[96] A. Qing, "Vector spectral-domain method for the analysis of frequency selective surfaces," *IEEE Trans. Antennas Propagat.*, vol. submitted, 2006.

[97] C. T. Tai, *Dyadic Green's Functions in Electromagnetic Theory.* Scranton: Intext, 1971.

[98] W. C. Chew, Ed., *Waves and Fields in Inhomogeneous Media.* New York: IEEE Press, 1995.

[99] R. E. Collin, "The dyadic green's function as an inverse operator," *Radio Sci.*, vol. 21, no. 6, pp. 883–890, 1986.

[100] P. W. Barber, "Differential-scattering of electromagnetic waves by homogeneous isotropic dielectric bodies," Ph.D. dissertation, University of California, Los Angeles, 1973.

[101] P. W. Barber and S. C. Hill, *Light Scattering by Particles: Computational Methods.* Singapore: World Scientific, 1990.

[102] B. Friedman and J. Russek, "Addition theorems for spherical waves," *Q. Appl. Math.*, vol. 12, no. 1, pp. 13–23, 1954.

[103] S. Stein, "Addition theorems for spherical wave functions," *Q. Appl. Math.*, vol. 19, no. 1, pp. 15–24, 1961.

[104] L. Tsang and J. A. Kong, "Effective propagation constants for coherent electromagnetic wave propagation in media embedded with dielectric scatterers," *J. Appl. Phys.*, vol. 53, no. 11, pp. 7162–7173, 1982.

[105] D. A. Vashalovich, A. N. Moskalev, and V. K. Khersonskii, *Quantum Theory of Angulary Momentum*. Singapore: World Scientific, 1988.

Appendix A

Scalar and Vector Spherical Wave Functions

A.1 Definition

The vector spherical wave functions $\mathbf{M}_{mn}(\mathbf{r})$ and $\mathbf{N}_{mn}(\mathbf{r})$ are the divergentless solutions of the vector Helmholtz equation in spherical coordinates [49, 80],

$$\nabla^2 \mathbf{E}(\mathbf{r}) + k^2 \mathbf{E}(\mathbf{r}) = 0, \tag{A.1}$$

where k is the propagation constant,

$$\mathbf{M}_{mn}(\mathbf{r}) = \nabla \times [\mathbf{r}\psi_{mn}(\mathbf{r})], \tag{A.2}$$

$$\mathbf{N}_{mn}(\mathbf{r}) = \frac{1}{k}\nabla \times \mathbf{M}_{mn}(\mathbf{r}). \tag{A.3}$$

where

$$\psi_{mn}(\mathbf{r}) = z_n(kr)\, P_n^m(\cos\theta)\, e^{im\phi} \tag{A.4}$$

is the solution to the scalar wave equation. The explicit expressions of the vector spherical wave functions are [52, 80]

$$\mathbf{M}_{mn}(\mathbf{r}) = \frac{im}{\sin\theta} z_n(kr) P_n^m(\cos\theta) e^{im\phi}\hat{\theta} - z_n(kr) \frac{dP_n^m(\cos\theta)}{d\theta} e^{im\phi}\hat{\phi}, \tag{A.5}$$

$$\begin{aligned} \mathbf{N}_{mn}(\mathbf{r}) = \ & n(n+1)\frac{z_n(kr)}{kr} P_n^m(\cos\theta) e^{im\phi}\hat{r} \\ & + \frac{1}{kr}\frac{d\left[(kr) z_n(kr)\right]}{d(kr)} \frac{dP_n^m(\cos\theta)}{d\theta} e^{im\phi}\hat{\theta} \\ & + \frac{im}{\sin\theta}\frac{1}{kr}\frac{d\left[(kr) z_n(kr)\right]}{d(kr)} P_n^m(\cos\theta) e^{im\phi}\hat{\phi} \end{aligned} , \tag{A.6}$$

where $\left(\hat{r}, \hat{\theta}, \hat{\phi}\right)$ is the set of spherical unit vectors.

In the above formulation, the spherical radial function $z_n(\cdot)$ can be any of the spherical Bessel functions $j_n(x)$, the spherical Neumann functions $y_n(x)$, and the spherical Hankel functions of the first and second kind, $h_n^{(1,2)}(x)$. However, from now on, we will specify the spherical radial function as $h_n^{(1)}(x)$ unless stated otherwise. The scalar and vector spherical wave functions are specified accordingly as the outgoing scalar and vector spherical wave functions.

By means of vector identities, Eq. (A.2) can be put in the alternative form,

$$\mathbf{M}_{mn}(\mathbf{r}) = \nabla\psi_{mn}(\mathbf{r}) \times \mathbf{r}, \tag{A.7}$$

It can be shown that

$$\mathbf{M}_{mn}(\mathbf{r}) = \frac{1}{k}\nabla \times \mathbf{N}_{mn}(\mathbf{r}), \tag{A.8}$$

$$\mathbf{M}_{-m,n}(\mathbf{r}) = (\ -1)^m \frac{(n-m)!}{(n+m)!}\tilde{\mathbf{M}}_{mn}(\mathbf{r}), \tag{A.9}$$

$$\mathbf{N}_{-m,n}(\mathbf{r}) = (\ -1)^m \frac{(n-m)!}{(n+m)!}\tilde{\mathbf{N}}_{mn}(\mathbf{r}), \tag{A.10}$$

where the overhead tilde symbol $\sim$ implies complex conjugate on the angular functions only.

Some authors prefer to decompose the scalar and vector spherical wave functions into even and odd components,

$$\psi_{mn}(\mathbf{r}) = \psi_{emn}(\mathbf{r}) + i\psi_{omn}(\mathbf{r})$$

$$\mathbf{M}_{mn}(\mathbf{r}) = \mathbf{M}_{emn}(\mathbf{r}) + i\mathbf{M}_{omn}(\mathbf{r}) \tag{A.11}$$

$$\mathbf{N}_{mn}(\mathbf{r}) = \mathbf{N}_{emn}(\mathbf{r}) + i\mathbf{N}_{omn}(\mathbf{r}), \tag{A.12}$$

where [82, 97]

$$\psi_{\substack{e\\o}mn}(\mathbf{r}) = \begin{matrix}\cos(m\phi)\\ \sin(m\phi)\end{matrix} P_n^m(\cos\theta)\, z_n(kr) \tag{A.13}$$

$$\mathbf{M}_{\substack{e\\o}mn}(\mathbf{r}) = \mp\frac{m}{\sin\theta} z_n(kr)\, P_n^m(\cos\theta) \begin{matrix}\sin(m\phi)\\ \cos(m\phi)\end{matrix}\, \hat{\theta} - z_n(kr)\,\frac{dP_n^m(\cos\theta)}{d\theta} \begin{matrix}\cos(m\phi)\\ \sin(m\phi)\end{matrix}\, \hat{\phi}, \tag{A.14}$$

$$\begin{aligned}\mathbf{N}_{\substack{e\\o}mn}(\mathbf{r}) = \quad & n(n+1)\frac{z_n(kr)}{kr} P_n^m(\cos\theta) \begin{matrix}\cos(m\phi)\\ \sin(m\phi)\end{matrix}\, \hat{r} \\ & + \tfrac{1}{kr}\frac{d\left[(kr)\, z_n(kr)\right]}{d(kr)}\frac{dP_n^m(\cos\theta)}{d\theta} \begin{matrix}\cos(m\phi)\\ \sin(m\phi)\end{matrix}\, \hat{\theta} \qquad , \\ & \mp\frac{m}{\sin\theta}\frac{1}{kr}\frac{d\left[(kr)\, z_n(kr)\right]}{d(kr)} P_n^m(\cos\theta) \begin{matrix}\sin(m\phi)\\ \cos(m\phi)\end{matrix}\, \hat{\phi}\end{aligned} \tag{A.15}$$

The even and odd components of the vector spherical wave functions also obey the relations

$$\mathbf{M}_{\substack{e\\o}mn}(\mathbf{r}) = \nabla \times \left[\mathbf{r}\psi_{\substack{e\\o}mn}(\mathbf{r})\right] \tag{A.16}$$

$$\mathbf{N}_{\substack{e\\o}mn}\left(\mathbf{r}\right) = \frac{1}{k}\nabla \times \mathbf{M}_{\substack{e\\o}mn}\left(\mathbf{r}\right) \tag{A.17}$$

It can be shown that

$$\tilde{\mathbf{M}}_{mn}\left(\mathbf{r}\right) = \mathbf{M}_{emn}\left(\mathbf{r}\right) - i\mathbf{M}_{omn}\left(\mathbf{r}\right), \tag{A.18}$$

$$\tilde{\mathbf{N}}_{mn}\left(\mathbf{r}\right) = \mathbf{N}_{emn}\left(\mathbf{r}\right) - i\mathbf{N}_{omn}\left(\mathbf{r}\right). \tag{A.19}$$

Using the orthogonality relations of even and odd components of vector spherical wave functions [91, 97, 98], various vector and dyadic functions can be expanded into vector spherical wave functions.

A.2 Eigenfunction Expansion of the Free Space Dyadic Green's Function

The free space dyadic Green's functions is [97–99]

$$\bar{\bar{\mathbf{G}}}\left(\mathbf{r},\mathbf{r}'\right) = \left[\bar{\bar{\mathbf{I}}} + \frac{\nabla\nabla}{k^2}\right] G\left(\mathbf{r},\mathbf{r}'\right), \tag{A.20}$$

where

$$G(\mathbf{r},\mathbf{r}') = \frac{\exp(ik\left|\mathbf{r}-\mathbf{r}'\right|)}{4\pi\left|\mathbf{r}-\mathbf{r}'\right|}. \tag{A.21}$$

According to [97, 100], we have

$$\begin{aligned}\bar{\bar{\mathbf{G}}}(\mathbf{r},\mathbf{r}') &= \frac{ik}{\pi}\sum_{n=1}^{\infty}\sum_{m=0}^{n} D_{mn}\left[\mathbf{M}_{\substack{e\\o}mn}\left(\mathbf{r}_>\right) Rg\mathbf{M}_{\substack{e\\o}mn}\left(\mathbf{r}_<\right) + \mathbf{N}_{\substack{e\\o}mn}\left(\mathbf{r}_>\right) Rg\mathbf{N}_{\substack{e\\o}mn}\left(\mathbf{r}_<\right)\right]\\ &= \frac{ik}{\pi}\sum_{n=1}^{\infty}\sum_{m=0}^{n} D_{mn}\left[Rg\mathbf{M}_{\substack{e\\o}mn}\left(\mathbf{r}_<\right)\mathbf{M}_{\substack{e\\o}mn}\left(\mathbf{r}_>\right) + Rg\mathbf{N}_{\substack{e\\o}mn}\left(\mathbf{r}_<\right)\mathbf{N}_{\substack{e\\o}mn}\left(\mathbf{r}_>\right)\right]\end{aligned}, \tag{A.22}$$

where $\mathbf{r}_>$ and $\mathbf{r}_<$ are, respectively, the greater and less of $\mathbf{r}$ and $\mathbf{r}'$, D_{mn} is the normalization constant,

$$D_{mn} = \left(2 - \delta_{m0}\right) \frac{(2n+1)}{4n\,(n+1)} \frac{(n-m)!}{(n+m)!} = \left(2 - \delta_{m0}\right) \sigma_{mn}, \tag{A.23}$$

the symbol Rg refers to the regular part and n starts with unity, since $n = 0$ and $m = 0$ corresponds to a null set, i.e.,

$$\mathbf{M}_{\substack{e\\o}00}\left(\mathbf{r}\right) = \mathbf{N}_{\substack{e\\o}00}\left(\mathbf{r}\right) = 0. \tag{A.24}$$

Using Eqs. (A.11), (A.12), (A.18) and (A.19), Eq. (A.22) can be written as

$$\begin{aligned} \bar{\bar{\mathbf{G}}}(\mathbf{r},\mathbf{r}') = \frac{ik}{\pi} \sum_{n=1}^{\infty} \sum_{m=0}^{n} \frac{D_{mn}}{2} \left[\mathbf{M}_{mn}\left(\mathbf{r}_{>}\right) Rg\tilde{\mathbf{M}}_{mn}\left(\mathbf{r}_{<}\right) + \tilde{\mathbf{M}}_{mn}\left(\mathbf{r}_{>}\right) Rg\mathbf{M}_{mn}\left(\mathbf{r}_{<}\right) \right] \\ + \frac{ik}{\pi} \sum_{n=1}^{\infty} \sum_{m=0}^{n} \frac{D_{mn}}{2} \left[\mathbf{N}_{mn}\left(\mathbf{r}_{>}\right) Rg\tilde{\mathbf{N}}_{mn}\left(\mathbf{r}_{<}\right) + \tilde{\mathbf{N}}_{mn}\left(\mathbf{r}_{>}\right) Rg\mathbf{N}_{mn}\left(\mathbf{r}_{<}\right) \right] \end{aligned} . \tag{A.25}$$

Using Eqs. (A.9) and (A.10) in Eq. (A.25), it gives

$$\begin{aligned} \bar{\bar{\mathbf{G}}}(\mathbf{r},\mathbf{r}') = \frac{ik}{\pi} \sum_{n=1}^{\infty} D_{0n} \mathbf{M}_{0n}\left(\mathbf{r}_{>}\right) Rg\tilde{\mathbf{M}}_{0n}\left(\mathbf{r}_{<}\right) + \frac{ik}{\pi} \sum_{n=1}^{\infty} \sum_{m=1}^{n} \frac{D_{mn}}{2} \mathbf{M}_{mn}\left(\mathbf{r}_{>}\right) Rg\tilde{\mathbf{M}}_{mn}\left(\mathbf{r}_{<}\right) \\ + \frac{ik}{\pi} \sum_{n=1}^{\infty} \sum_{m=-1}^{-n} \frac{D_{-m,n}}{2} \frac{(n-m)!}{(n+m)!} \frac{(n-m)!}{(n+m)!} \mathbf{M}_{mn}\left(\mathbf{r}_{>}\right) Rg\tilde{\mathbf{M}}_{mn}\left(\mathbf{r}_{<}\right) \\ + \frac{ik}{\pi} \sum_{n=1}^{\infty} D_{0n} \mathbf{N}_{0n}\left(\mathbf{r}_{>}\right) Rg\tilde{\mathbf{N}}_{0n}\left(\mathbf{r}_{<}\right) + \frac{ik}{\pi} \sum_{n=1}^{\infty} \sum_{m=1}^{n} \frac{D_{mn}}{2} \mathbf{N}_{mn}\left(\mathbf{r}_{>}\right) Rg\tilde{\mathbf{N}}_{mn}\left(\mathbf{r}_{<}\right) \\ + \frac{ik}{\pi} \sum_{n=1}^{\infty} \sum_{m=-1}^{-n} \frac{D_{-m,n}}{2} \frac{(n-m)!}{(n+m)!} \frac{(n-m)!}{(n+m)!} \mathbf{N}_{mn}\left(\mathbf{r}_{>}\right) Rg\tilde{\mathbf{N}}_{mn}\left(\mathbf{r}_{<}\right) \end{aligned} . \tag{A.26}$$

Since

$$D_{-m,n} \frac{(n-m)!}{(n+m)!} \frac{(n-m)!}{(n+m)!} = \left(2 - \delta_{m0}\right) \frac{(2n+1)}{4n\,(n+1)} \frac{(n-m)!}{(n+m)!} = D_{mn}. \tag{A.27}$$

Therefore,

$$\begin{aligned}\bar{\bar{\mathbf{G}}}(\mathbf{r},\mathbf{r}') &= \frac{ik}{\pi}\sum_{n=1}^{\infty}\sum_{m=-n}^{n}\frac{D_{mn}}{2-\delta_{m0}}\left[\mathbf{M}_{mn}\left(\mathbf{r}_>\right)Rg\tilde{\mathbf{M}}_{mn}\left(\mathbf{r}_<\right)+\mathbf{N}_{mn}\left(\mathbf{r}_>\right)Rg\tilde{\mathbf{N}}_{mn}\left(\mathbf{r}_<\right)\right] \\ &= \frac{ik}{\pi}\sum_{n=1}^{\infty}\sum_{m=-n}^{n}\sigma_{mn}\left[Rg\tilde{\mathbf{M}}_{mn}\left(\mathbf{r}_<\right)\mathbf{M}_{mn}\left(\mathbf{r}_>\right)+Rg\tilde{\mathbf{N}}_{mn}\left(\mathbf{r}_<\right)\mathbf{N}_{mn}\left(\mathbf{r}_>\right)\right]\end{aligned}, \tag{A.28}$$

where $\sigma_{mn} = \dfrac{D_{mn}}{2-\delta_{m0}}$.

A.3 Eigenfunction Expansion of Plane Waves

Barber and Hill [101] have given the eigenfunction expansion of plane waves into even and odd components of the vector spherical wave functions:

$$\begin{aligned}\hat{e}_0 e^{i\mathbf{k}\cdot\mathbf{r}} &= \sum_{n=1}^{\infty}\sum_{m=0}^{n}D_{mn}\left[a_{emn}Rg\mathbf{M}_{emn}(\mathbf{r})+a_{omn}Rg\mathbf{M}_{omn}(\mathbf{r})\right] \\ &+\sum_{n=1}^{\infty}\sum_{m=0}^{n}D_{mn}\left[b_{emn}Rg\mathbf{N}_{emn}(\mathbf{r})+b_{omn}Rg\mathbf{N}_{omn}(\mathbf{r})\right]\end{aligned}, \tag{A.29}$$

where $\hat{e}_0$ is the unit polarization vector and $\mathbf{k}\left(\theta^{inc},\phi^{inc}\right)$ is the propagation vector, $a_{\substack{e\\o}mn}$ and $b_{\substack{e\\o}mn}$, are the incident field expansion coefficients,

$$a_{emn} = 4i^n\hat{e}_0\cdot\left[-\hat{\theta}\sin\left(m\phi\right)m\frac{P_n^m\left(\cos\theta\right)}{\sin\theta}-\hat{\phi}\cos\left(m\phi\right)\frac{dP_n^m\left(\cos\theta\right)}{d\theta}\right]_{\theta=\theta^{inc},\phi=\phi^{inc}}, \tag{A.30}$$

$$a_{omn} = 4i^n\hat{e}_0\cdot\left[\hat{\theta}\cos\left(m\phi\right)m\frac{P_n^m\left(\cos\theta\right)}{\sin\theta}-\hat{\phi}\sin\left(m\phi\right)\frac{dP_n^m\left(\cos\theta\right)}{d\theta}\right]_{\theta=\theta^{inc},\phi=\phi^{inc}}, \tag{A.31}$$

$$b_{emn} = -4i^{n+1}\hat{e}_0\cdot\left[\hat{\theta}\cos\left(m\phi\right)\frac{dP_n^m\left(\cos\theta\right)}{d\theta}-\hat{\phi}\sin\left(m\phi\right)m\frac{P_n^m\left(\cos\theta\right)}{\sin\theta}\right]_{\theta=\theta^{inc},\phi=\phi^{inc}}, \tag{A.32}$$

$$b_{omn} = -4i^{n+1}\hat{e}_0\cdot\left[\hat{\theta}\sin\left(m\phi\right)\frac{dP_n^m\left(\cos\theta\right)}{d\theta} + \hat{\phi}\cos\left(m\phi\right)m\frac{P_n^m\left(\cos\theta\right)}{\sin\theta}\right]_{\theta=\theta^{inc},\phi=\phi^{inc}}. \tag{A.33}$$

For the convenience of our future applications, it is more desirable to expand the plane waves in vector spherical wave functions as

$$\hat{e}_0 e^{i\mathbf{k}\cdot\mathbf{r}} = \sum_{n=1}^{\infty}\sum_{m=-n}^{n} a_{mn}Rg\mathbf{M}_{mn}(\mathbf{r}) + b_{mn}Rg\mathbf{N}_{mn}(\mathbf{r}). \tag{A.34}$$

Using Eqs. (A.9)-(A.12), (A.18) and (A.19), it can be shown that

$$\begin{aligned} a_{mn} &= \sigma_{mn}\left[a_{emn} - ia_{omn}\right] \\ &= \sigma_{mn}4i^n\hat{e}_0\cdot\left[\hat{\theta}\frac{-imP_n^m\left(\cos\theta\right)}{\sin\theta} - \hat{\phi}\frac{dP_n^m\left(\cos\theta\right)}{d\theta}\right]e^{-im\phi}\left.\right|_{\theta=\theta^{inc},\phi=\phi^{inc}}, \end{aligned} \tag{A.35}$$

$$\begin{aligned} b_{mn} &= \sigma_{mn}\left[b_{emn} - ib_{omn}\right] \\ &= \sigma_{mn}4i^{n+1}\hat{e}_0\cdot\left[-\hat{\theta}\frac{dP_n^m\left(\cos\theta\right)}{d\theta} + \hat{\phi}\frac{imP_n^m\left(\cos\theta\right)}{\sin\theta}\right]e^{-im\phi}\left.\right|_{\theta=\theta^{inc},\phi=\phi^{inc}}. \end{aligned} \tag{A.36}$$

Appendix B

Translational Addition Theorems

B.1 Scalar Spherical Wave Functions Translational Addition Theorems

Friedman and Russek [102] gave the first derivation of the scalar spherical wave functions translational addition theorems. In 1961, Stein [103] corrected the mistakes in [102] and made further extension to the scalar spherical wave functions translational addition theorems. Here, we follow the same process in [103] to derive the scalar spherical wave functions translational addition theorems.

The configuration of the coordinate translation is depicted in Fig. B-1.

$$\mathbf{r} = \mathbf{r}' + \mathbf{r}_0, \tag{B.1}$$

where $\mathbf{r}\,(r, \theta, \phi)$ is the field point in the original spherical coordinates with origin at O, $\mathbf{r}'\,(r', \theta', \phi')$ is the field point in the translated spherical coordinates with origin at O', $\mathbf{r}_0\,(r_0, \theta_0, \phi_0)$ is the translation vector in the original spherical coordinates,

$$\mathbf{r}_0 = r_0 \left(\sin\theta_0 \cos\phi_0 \hat{x} + \sin\theta_0 \sin\phi_0 \hat{y} + \cos\theta_0 \hat{z}\right), \tag{B.2}$$

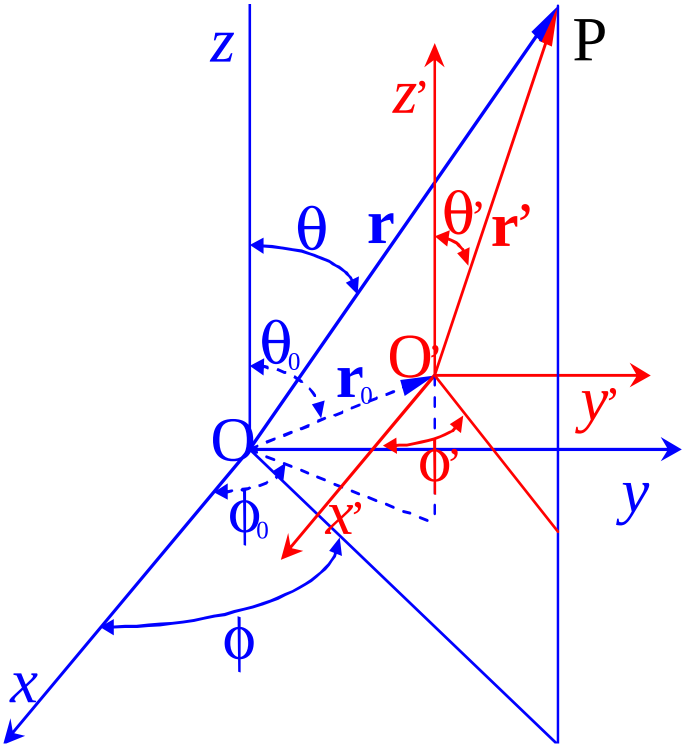

Figure B-1: Coordinate Translation

$(\hat{x}, \hat{y}, \hat{z})$ is the set of unit vectors in the corresponding Cartesian coordinates (since there is no coordinate rotation, the set of Cartesian unit vectors applies to both the original and the translated spherical coordinates).

Spherical wave functions under coordinate translation can be obtained conceptually in three steps. Firstly, expand the spherical wave into plane waves. Then perform coordinate translation on plane waves. Finally, expand plane waves into spherical waves expressed in the translated coordinates. Therefore, we need the expression for expanding spherical waves into plane waves and that for expanding plane waves into spherical waves.

Consider a point P whose position vector with respect to the origin O is $\mathbf{r}\,(r, \theta, \phi)$. A plane wave coming in along the direction $\mathbf{k}\,(\alpha, \beta)$ can be expressed in terms of spherical waves with center at O as follows,

$$e^{ikr\cos\gamma} = \sum_{n=0}^{\infty} \sum_{m=-n}^{n} i^n (2n+1) \frac{(n-m)!}{(n+m)!} j_n(kr)\, P_n^m(\cos\alpha)\, P_n^m(\cos\theta)\, e^{\pm im(\beta-\phi)}. \tag{B.3}$$

The plane wave expansion of standing spherical wave function is an integral representation of standing spherical wave function given by

$$j_n(kr)\, P_n^m(\cos\theta)\, e^{im\phi} = \frac{i^{(-n)}}{4\pi} \int_0^{2\pi} \int_0^{\pi} e^{ikr\cos\gamma} P_n^m(\cos\alpha)\, e^{im\beta} \sin\alpha\, d\alpha\, d\beta, \tag{B.4}$$

Similarly, the plane wave expansion of outgoing spherical wave function is given by

$$h_n^{(1)}(kr)\, P_n^m(\cos\theta)\, e^{im\phi} = \frac{i^{(-n)}}{2\pi} \int_0^{2\pi} \int_0^{\pi/2-i\infty} e^{ikr\cos\gamma} P_n^m(\cos\alpha)\, e^{im\beta} \sin\alpha\, d\alpha\, d\beta, \tag{B.5}$$

The translation of a plane wave with wave vector $\mathbf{k}(\alpha,\beta)$ is simply the change in the expression of its phase term

$$\begin{aligned} &\mathbf{k}\cdot\mathbf{r} = kr\cos\gamma = \mathbf{k}\cdot(\mathbf{r}'+\mathbf{r}_0) \\ &= kr'\left[\cos\alpha\cos\theta' + \sin\alpha\sin\theta'\cos(\beta-\phi')\right] \\ &\quad + kr_0\left[\cos\alpha\cos\theta_0 + \sin\alpha\sin\theta_0\cos(\beta-\phi_0)\right] \\ &= kr'\cos\gamma' + kr_0\cos\gamma_0 \end{aligned}, \tag{B.6}$$

where γ' is the angle between the propagation vector $\mathbf{k}(\alpha,\beta)$ and the position vector $\mathbf{r}'(r',\theta',\phi')$, while γ_0 is the angle between the propagation vector $\mathbf{k}(\alpha,\beta)$ and the translation vector $\mathbf{r}_0(r_0,\theta_0,\phi_0)$.

B.1.1 Translational Addition Theorems for Standing Spherical Wave Functions

Substituting Eq. (B.6) into Eq. (B.4), we have

$$j_n\left(kr\right)P_n^m\left(\cos\theta\right)e^{im\phi} = \frac{i^{(-n)}}{4\pi}\int\limits_0^{2\pi}\int\limits_0^{\pi} e^{ikr'\cos\gamma'}e^{ikr_0\cos\gamma_0}P_n^m\left(\cos\alpha\right)e^{im\beta}\sin\alpha d\alpha d\beta. \tag{B.7}$$

For the term $e^{e^{ikr'\cos\gamma'}}$, we use the expansion corresponding to Eq. (B.3)

$$e^{ikr'\cos\gamma'} = \sum_{\nu=0}^{\infty}\sum_{\mu=-\nu}^{\nu} i^{\nu}(2\nu+1)\frac{(\nu-\mu)!}{(\nu+\mu)!}j_{\nu}\left(kr'\right)P_{\nu}^{\mu}\left(\cos\alpha\right)P_{\nu}^{\mu}\left(\cos\theta'\right)e^{-i\mu(\phi'-\beta)}. \tag{B.8}$$

Substitute Eq. (B.8) into Eq. (B.7) and exchange the order of summation and integration, we have

$$\begin{array}{c} j_n\left(kr\right)P_n^m\left(\cos\theta\right)e^{im\phi} = \dfrac{i^{(-n)}}{4\pi}\sum\limits_{\nu=0}^{\infty}\sum\limits_{\mu=-\nu}^{\nu} i^{\nu}(2\nu+1)\dfrac{(\nu-\mu)!}{(\nu+\mu)!}j_{\nu}\left(kr'\right)P_{\nu}^{\mu}\left(\cos\theta'\right)e^{-i\mu\phi'} \\ \cdot\int\limits_0^{2\pi}\int\limits_0^{\pi} e^{ikr_0\cos\gamma_0}P_n^m\left(\cos\alpha\right)P_{\nu}^{\mu}\left(\cos\alpha\right)e^{i(m+\mu)\beta}\sin\alpha d\alpha d\beta \end{array}. \tag{B.9}$$

Using the addition theorem for associated Legendre functions, we have

$$\begin{array}{c} j_n\left(kr\right)P_n^m\left(\cos\theta\right)e^{im\phi} = \dfrac{i^{(-n)}}{4\pi}\sum\limits_{\nu=0}^{\infty}\sum\limits_{\mu=-\nu}^{\nu}\sum\limits_{p} i^{\nu}(2\nu+1)\dfrac{(\nu-\mu)!}{(\nu+\mu)!}a\left(m,n\left|\mu,\nu\right|p\right)I_p^{m,\mu} \\ \times j_{\nu}\left(kr'\right)P_{\nu}^{\mu}\left(\cos\theta'\right)e^{-i\mu\phi'} \end{array}, \tag{B.10}$$

where

$$\begin{aligned} I_p^{m,\mu} &= \int\limits_0^{2\pi}\int\limits_0^{\pi} e^{ikr_0\cos\gamma_0}P_p^{m+\mu}\left(\cos\alpha\right)e^{i(m+\mu)\beta}\sin\alpha d\alpha d\beta \qquad \text{(B.11)} \\ &= 4\pi i^p j_p\left(kr_0\right)P_p^{m+\mu}\left(\cos\theta_0\right)e^{i(m+\mu)\phi_0}, \end{aligned}$$

Substitute Eq. (B.11) into Eq. (B.10), we have the formula for the expansion of a standing spherical wave $j_n(kr)\,P_n^m(\cos\theta)\,e^{im\phi}$, with respect to the original O, in terms of the standing spherical waves $j_\nu(kr')\,P_\nu^\mu(\cos\theta')\,e^{i\mu\phi'}$, with respect to the translated O',

$$\begin{aligned}
j_n(kr)\,P_n^m(\cos\theta)\,e^{im\phi} &= \sum_{\nu=0}^{\infty}\sum_{\mu=-\nu}^{\nu}\sum_{p} i^{\nu+p-n}(2\nu+1)\frac{(\nu-\mu)!}{(\nu+\mu)!}a\,(m,n\,|\mu,\nu\,|p) \\
&\quad\times j_p(kr_0)\,P_p^{m+\mu}(\cos\theta_0)\,e^{i(m+\mu)\phi_0}j_\nu(kr')\,\bar{P}_\nu^{\mu}(\cos\theta')\,e^{-i\mu\phi'} \\
&= \sum_{\nu=0}^{\infty}\sum_{\mu=-\nu}^{\nu}\sum_{p} i^{\nu+p-n}(2\nu+1)\frac{(\nu+\mu)!}{(\nu-\mu)!}a\,(m,n\,|-\mu,\nu\,|p) \\
&\quad\times j_p(kr_0)\,\bar{P}_p^{m-\mu}(\cos\theta_0)\,e^{i(m-\mu)\phi_0}j_\nu(kr')\,P_\nu^{-\mu}(\cos\theta')\,e^{i\mu\phi'}
\end{aligned} \quad . \tag{B.12}$$

Using the properties of associated Legendre function, we get

$$\begin{aligned}
j_n(kr)\,P_n^m(\cos\theta)\,e^{im\phi} &= \sum_{\nu=0}^{\infty}\sum_{\mu=-\nu}^{\nu}\sum_{p}(-1)^{\mu}\,i^{\nu+p-n}(2\nu+1)a\,(m,n\,|-\mu,\nu\,|p) \\
&\quad\times j_p(kr_0)\,P_p^{m-\mu}(\cos\theta_0)\,e^{i(m-\mu)\phi_0}j_\nu(kr')\,P_\nu^{\mu}(\cos\theta')\,e^{i\mu\phi'}
\end{aligned} \quad . \tag{B.13}$$

Similarly, we have

$$\begin{aligned}
j_n(kr)\,P_n^m(\cos\theta)\,e^{im\phi} &= \sum_{\nu=0}^{\infty}\sum_{\mu=-\nu}^{\nu}\sum_{p}(-1)^{\mu}\,i^{\nu+p-n}(2\nu+1)a\,(m,n\,|-\mu,\nu\,|p) \\
&\quad\times j_\nu(kr_0)\,P_\nu^{\mu}(\cos\theta_0)\,e^{i\mu\phi_0}j_p(kr')\,P_p^{m-\mu}(\cos\theta')\,e^{i(m-\mu)\phi'}
\end{aligned} \quad . \tag{B.14}$$

B.1.2 Translational Addition Theorems for Other Spherical Wave Functions

The translational addition theorems for outgoing spherical wave functions can be obtained in a similar manner:

$$h_n^{(1)}(kr)\,P_n^m(\cos\theta)\,e^{im\phi} = \sum_{\nu=0}^{\infty}\sum_{\mu=-\nu}^{\nu}\sum_{p}(\,-1)^{\mu}\,i^{\nu+p-n}(2\nu+1)a\,(m,n\,|\,-\mu,\nu\,|p) \\ \times h_p^{(1)}(kr_0)\,P_p^{m-\mu}(\cos\theta_0)\,e^{i(m-\mu)\phi_0}j_\nu(kr')\,P_\nu^{\mu}(\cos\theta')\,e^{i\mu\phi'}, \tag{B.15}$$

for $r' < r_0$, and

$$h_n^{(1)}(kr)\,P_n^m(\cos\theta)\,e^{im\phi} = \sum_{\nu=0}^{\infty}\sum_{\mu=-\nu}^{\nu}\sum_{p}(\,-1)^{\mu}\,i^{\nu+p-n}(2\nu+1)a\,(m,n\,|\,-\mu,\nu\,|p) \\ \times j_\nu(kr_0)\,P_\nu^{\mu}(\cos\theta_0)\,e^{i\mu\phi_0}h_p^{(1)}(kr')\,P_p^{m-\mu}(\cos\theta')\,e^{i(m-\mu)\phi'}, \tag{B.16}$$

For $r' > r_0$.

The translational addition theorems for incoming spherical wave functions can be obtained using the relationship between spherical Bessel functions, and spherical Hankel functions of the first and second kind,

$$h_n^{(1)}(kr) + h_n^{(2)}(kr) = 2j_n(kr)\,.$$

The results are

$$h_n^{(2)}(kr)\,P_n^m(\cos\theta)\,e^{im\phi} = \sum_{\nu=0}^{\infty}\sum_{\mu=-\nu}^{\nu}\sum_{p}(\,-1)^{\mu}\,i^{\nu+p-n}(2\nu+1)a\,(m,n\,|\,-\mu,\nu\,|p) \\ \times h_p^{(2)}(kr_0)\,P_p^{m-\mu}(\cos\theta_0)\,e^{i(m-\mu)\phi_0}j_\nu(kr')\,P_\nu^{\mu}(\cos\theta')\,e^{i\mu\phi'}, \tag{B.17}$$

for $r' < r_0$, and

$$h_n^{(2)}(kr)\,P_n^m(\cos\theta)\,e^{im\phi} = \sum_{\nu=0}^{\infty}\sum_{\mu=-\nu}^{\nu}\sum_{p}(\,-1)^{\mu}\,i^{\nu+p-n}(2\nu+1)a\,(m,n\,|\,-\mu,\nu\,|p) \\ \times h_p^{(2)}(kr')\,P_p^{m-\mu}(\cos\theta')\,e^{i(m-\mu)\phi'}j_\nu(kr_0)\,P_\nu^{\mu}(\cos\theta_0)\,e^{i\mu\phi_0}, \tag{B.18}$$

for $r' > r_0$.

Considering Eqs. (B.13)-(B.18), we have the general translational addition theorems for scalar spherical wave functions

$$\begin{aligned}\psi_{mn}\left(r,\theta,\phi\right)=\sum_{\nu=0}^{\infty}\sum_{\mu=-\nu}^{\nu}\sum_{p}\left(-1\right)^{\mu}i^{\nu+p-n}(2\nu+1)a\left(m,n\left|-\mu,\nu\right|p\right)\\ \times\psi_{m-\mu,p}\left(r_{>},\theta_{>},\phi_{>}\right)Rg\psi_{\mu\nu}\left(r_{<},\theta_{<},\phi_{<}\right)\end{aligned}, \quad \text{(B.19)}$$

where

$$\left\{\begin{array}{ll} r_{>}=r_0 & r_{<}=r' \\ \theta_{>}=\theta_0 & \theta_{<}=\theta' \\ \phi_{>}=\phi_0 & \phi_{<}=\phi' \end{array}\right\} \text{ when } r'\le r_0, \quad \text{(B.20)}$$

and

$$\left\{\begin{array}{ll} r_{>}=r' & r_{<}=r_0 \\ \theta_{>}=\theta' & \theta_{<}=\theta_0 \\ \phi_{>}=\phi' & \phi_{<}=\phi_0 \end{array}\right\} \text{ when } r'\ge r_0. \quad \text{(B.21)}$$

B.1.3 Extended Scalar Spherical Wave Functions Translational Addition Theorems

For convenience of the derivation of the vector spherical wave functions translational addition theorems, it is desirable to have the scalar spherical wave functions translational addition theorems in the form

$$\psi_{mn}\left(r,\theta,\phi\right)=\left\{\begin{array}{ll}\sum\limits_{\nu=0}^{\infty}\sum\limits_{\mu=-\nu}^{\nu}a\left(m,n\left|\mu,\nu\right.\right)Rg\psi_{\mu\nu}\left(r',\theta',\phi'\right) & r'\le r_0\\ \sum\limits_{\nu=0}^{\infty}\sum\limits_{\mu=-\nu}^{\nu}Rga\left(m,n\left|\mu,\nu\right.\right)\psi_{\mu\nu}\left(r',\theta',\phi'\right) & r'>r_0\end{array}\right., \quad \text{(B.22)}$$

where

$$a\left(m,n\left|\mu,\nu\right.\right)=\left(\,-1\right)^{\mu}i^{\nu-n}(2\nu+1)\sum_{p}i^{p}a\left(m,n\left|\,-\mu,\nu\right|p\right)\psi_{m-\mu,p}\left(r_0,\theta_0,\phi_0\right), \tag{B.23}$$

regardless the values of r' and r_0.

For the case $r'\leq r_0$, we have exactly such a form

$$\psi_{mn}\left(r,\theta,\phi\right)=\sum_{\nu=0}^{\infty}\sum_{\mu=-\nu}^{\nu}a_{<}\left(m,n\left|\mu,\nu\right.\right)Rg\psi_{\mu\nu}\left(r',\theta',\phi'\right)\quad r'\leq r_0, \tag{B.24}$$

where

$$a_{<}\left(m,n\left|\mu,\nu\right.\right)=\left(\,-1\right)^{\mu}i^{\nu-n}(2\nu+1)\sum_{p}i^{p}a\left(m,n\left|\,-\mu,\nu\right|p\right)\psi_{m-\mu,p}\left(r_0,\theta_0,\phi_0\right), \tag{B.25}$$

However, for $r'\geq r_0$, the scalar spherical wave functions translational addition theorems are

$$\begin{array}{r}\psi_{mn}\left(r,\theta,\phi\right)=\sum\limits_{\nu=0}^{\infty}\sum\limits_{\mu=-\nu}^{\nu}\sum\limits_{p}\left(\,-1\right)^{\mu}i^{\nu+p-n}(2\nu+1)a\left(m,n\left|\,-\mu,\nu\right|p\right)\\ \times Rg\psi_{\mu\nu}\left(r_0,\theta_0,\phi_0\right)\psi_{m-\mu,p}\left(r',\theta',\phi'\right)\end{array}. \tag{B.26}$$

The r' variations in Eq. (B.26) go into the term $\psi_{m-\mu,p}\left(r',\theta',\phi'\right)$, and in order to obtain a form like Eq. (B.24), it is necessary to interchange the orders of summation. That such an interchanged form must be available is obvious, since the result is then exactly the one expected from the usual technique of expanding an arbitrary function of (r,θ,ϕ) in terms of a new coordinate origin and new coordinate set.

We accomplish the interchange by noting that in Eq. (B.26), p eventually takes on all values between 0 and ∞. Further more, the formal extension of the inner sum to $0 < p < \infty$ can be made since the $a\left(m,n\left|\mu,\nu\right|p\right)$ will vanish for all the added terms. We can also extend the sum on μ to $(-\infty,\infty)$ since P_ν^μ vanishes for all the added terms.

Interchange the p- and ν-summations in Eq. (B.26), we have

$$\begin{aligned}\psi_{mn}\left(r,\theta,\phi\right) = \sum_{p=0}^{\infty}\sum_{\mu=-\infty}^{\infty}\sum_{\nu=0}^{\infty}\left(\,-1\right)^{\mu} i^{\nu+p-n}(2\nu+1)a\left(m,n\left|\,-\mu,\nu\right|p\right)\\ \times Rg\psi_{\mu\nu}\left(r_0,\theta_0,\phi_0\right)\psi_{m-\mu,p}\left(r',\theta',\phi'\right)\end{aligned}. \quad (B.27)$$

Substitute a new index $t = m - \mu$, we have

$$\begin{aligned}\psi_{mn}\left(r,\theta,\phi\right) = i^{-n}\sum_{p=0}^{\infty}\sum_{t=-\infty}^{\infty}\sum_{\nu=0}^{\infty}\left(\,-1\right)^{m-t} i^{\nu+p}(2\nu+1)a\left(m,n\left|t-m,\nu\right|p\right)\\ \times Rg\psi_{m-t,\nu}\left(r_0,\theta_0,\phi_0\right)\psi_{tp}\left(r',\theta',\phi'\right)\end{aligned}. \quad (B.28)$$

Interchange the p- and ν notations in Eq. (B.28), we have

$$\begin{aligned}\psi_{mn}\left(r,\theta,\phi\right) = i^{-n}\sum_{\nu=0}^{\infty}\sum_{t=-\infty}^{\infty}\sum_{p=0}^{\infty}\left(\,-1\right)^{m-t} i^{\nu+p}(2p+1)a\left(m,n\left|t-m,p\right|\nu\right)\\ \times Rg\psi_{m-t,p}\left(r_0,\theta_0,\phi_0\right)\psi_{t\nu}\left(r',\theta',\phi'\right)\end{aligned}. \quad (B.29)$$

Write μ for t in Eq. (B.29),

$$\begin{aligned}\psi_{mn}\left(r,\theta,\phi\right) = i^{-n}\sum_{\nu=0}^{\infty}\sum_{\mu=-\infty}^{\infty}\sum_{p=0}^{\infty}\left(\,-1\right)^{m-\mu} i^{\nu+p}(2p+1)a\left(m,n\left|\mu-m,p\right|\nu\right)\\ \times\psi_{\mu\nu}\left(r',\theta',\phi'\right)Rg\psi_{m-\mu,p}\left(r_0,\theta_0,\phi_0\right)\end{aligned}. \quad (B.30)$$

Note that $P_\nu^\mu = 0$ whenever $|\mu| > \nu$, we can rewrite the above as

$$\begin{aligned}\psi_{mn}\left(r,\theta,\phi\right) = i^{-n}\sum_{\nu=0}^{\infty}\sum_{\mu=-\nu}^{\nu}\sum_{p=0}^{\infty}&\left(\,-1\right)^{m-\mu}i^{\nu+p}(2p+1)a\left(m,n\left|\mu-m,p\right|\nu\right) \\ &\times Rg\psi_{m-\mu,p}\left(r_0,\theta_0,\phi_0\right)\psi_{\mu\nu}\left(r',\theta',\phi'\right)\end{aligned} \quad . \tag{B.31}$$

It is readily confirmed that the coefficient in this last equation also vanishes unless at least, $n+\nu \geq p \geq |n-\nu|$, so that it is even more in a form similar to Eq. (B.24),

$$\psi_{mn}\left(r,\theta,\phi\right) = \sum_{\nu=0}^{\infty}\sum_{\mu=-\nu}^{\nu}\alpha_{>}\left(m,n\left|\mu,\nu\right.\right)\psi_{\mu\nu}\left(r',\theta',\phi'\right) \quad r' \geq r_0, \tag{B.32}$$

where

$$\begin{aligned}&\alpha_{>}\left(m,n\left|\mu,\nu\right.\right) \\ &= \left(\,-1\right)^{m-\mu}i^{-n+\nu}\sum_{p}i^{p}(2p+1)a\left(m,n\left|\mu-m,p\right|\nu\right)Rg\psi_{m-\mu,p}\left(r_0,\theta_0,\phi_0\right).\end{aligned} \tag{B.33}$$

Although this result in Eq. (B.33) appears to be different from the form in Eq. (B.25), one expects on the basis of continuity of the two expansions across the surface $r' = r_0$ that they should be equivalent. It has been proven true.

B.2 Vector Spherical Wave Functions Translational Addition Theorems

In 1961, Stein [103] gave the vector spherical wave functions translational addition theorems with very brief intermediate derivation for the first time. Later, Cruzan [80] followed the idea of Stein to present a more detailed derivation of the vector spherical wave functions translational addition theorems.

In [80], to derive the vector spherical wave functions translational addition theorems, the translation vector is first written in the form of Cartesian coordinate components. It is then substituted into the original definition of the vector spherical wave functions to expand the original vector spherical wave functions into four terms, of which one involves the translated position vector, and the other three involve the three unity Cartesian vectors. Applying the extended scalar spherical wave functions translational addition theorems to the above expansion leads to the expansion of the original spherical wave functions into vector products of the gradients of the scalar spherical wave functions in the translated coordinates, with both the translated position vector and unity Cartesian vectors. The term involving the translated position vector is easily written in the form of vector spherical wave functions in the translated coordinate. The other three terms involving the three unity Cartesian vectors are also written as the expansion by vector spherical wave functions in the translated coordinates. Cartesian-spherical unity vector transformation, vector operations and a lot of recursive relations of spherical radial functions and associated Legendre functions are used to obtain the expansion coefficients. The expansion coefficients related to **N** vector spherical wave functions in the translated coordinates for each term are obtained first by using the property that the **M** vector spherical wave functions do not have radial component. The expansion coefficients related to **M** vector spherical wave functions in the translated coordinate are then derived.

The vector spherical wave functions translational addition theorems given by Cruzan are commonly referenced by this community soon after they were published. However, Cruzan's vector spherical wave functions translational addition theorems is incorrect. Later, Tsang, Kong, Shin, and Chew [55, 98, 104] pointed out that there is a sign error in Cruzan's expression for $b\left(n,\nu,p\right)$. The sign correction was accepted and the corrected vector spherical wave functions translational addition theorems are commonly referenced by this community.

Here, we follow the idea in [80] to re-derive the vector spherical wave functions translational addition theorems. Comparing our derivations and the results by

Cruzan, mistakes in the previous formulations have been observed.

B.2.1 Vector Spherical Wave Functions under Coordinate Translation

The coordinate translation is identical to that shown in Fig. B-1. Substitute Eqs. (B.1) and (B.2) into Eq. (A.7), we have

$$\begin{aligned}\mathbf{M}_{mn}(\mathbf{r}) = r_0 [&\sin\theta_0\cos\phi_0\nabla\psi_{mn}(\mathbf{r})\times\hat{x} + \sin\theta_0\sin\phi_0\nabla\psi_{mn}(\mathbf{r})\times\hat{y} \\ &+\cos\theta_0\nabla\psi_{mn}(\mathbf{r})\times\hat{z}] + \nabla\psi_{mn}(\mathbf{r})\times\mathbf{r}'\end{aligned}. \quad \text{(B.34)}$$

Since the gradient of a scalar quantity is invariant to a transformation of the coordinate system, then we may regard $\nabla\psi_{mn}(\mathbf{r})$ as being expressed in terms of the translated (primed) coordinate. Consequently, for the case $r' < r_0$, making use of the scalar spherical wave functions translational addition theorems in Eq. (B.24), we have

$$\nabla\psi_{mn}(\mathbf{r}) = \sum_{\nu=1}^{\infty}\sum_{\mu=-\nu}^{\nu} a(m,n\,|\mu,\nu)\, Rg\nabla'\psi'_{\mu\nu}(\mathbf{r}'). \quad \text{(B.35)}$$

ν here starts with unity because $\nabla\psi_{00}(\mathbf{r}) = 0$. Therefore,

$$\nabla\psi_{mn}(\mathbf{r})\times\mathbf{r}' = \sum_{\nu=1}^{\infty}\sum_{\mu=-\nu}^{\nu} a(m,n\,|\mu,\nu)\, Rg\mathbf{M}'_{\mu\nu}(\mathbf{r}'). \quad \text{(B.36)}$$

One would expect that the other terms on the right hand side of Eq. (B.34) can also be written in a form similar to Eq. (B.36), namely,

$$\nabla\psi_{mn}(\mathbf{r})\times\hat{x} = \sum_{\nu=1}^{\infty}\sum_{\mu=-\nu}^{\nu} a^{x}_{\mu\nu}(\mathbf{r}_0)\, Rg\mathbf{M}'_{\mu\nu}(\mathbf{r}') + b^{x}_{\mu\nu}(\mathbf{r}_0)\, Rg\mathbf{N}'_{\mu\nu}(\mathbf{r}'), \quad \text{(B.37)}$$

$$\nabla\psi_{mn}\left(\mathbf{r}\right)\times\hat{y}=\sum_{\nu=1}^{\infty}\sum_{\mu=-\nu}^{\nu}a_{\mu\nu}^{y}\left(\mathbf{r}_0\right)Rg\mathbf{M'}_{\mu\nu}\left(\mathbf{r'}\right)+b_{\mu\nu}^{y}\left(\mathbf{r}_0\right)Rg\mathbf{N'}_{\mu\nu}\left(\mathbf{r'}\right),\tag{B.38}$$

$$\nabla\psi_{mn}\left(\mathbf{r}\right)\times\hat{z}=\sum_{\nu=1}^{\infty}\sum_{\mu=-\nu}^{\nu}a_{\mu\nu}^{z}\left(\mathbf{r}_0\right)Rg\mathbf{M'}_{\mu\nu}\left(\mathbf{r'}\right)+b_{\mu\nu}^{z}\left(\mathbf{r}_0\right)Rg\mathbf{N'}_{\mu\nu}\left(\mathbf{r'}\right).\tag{B.39}$$

The tough and tedious part of the derivation is to obtain the expansion coefficients in Eqs. (B.37)-(B.39), where the properties of Bessel and Legendre functions are frequently used to rewrite and reduce the expressions. Without going into the details, the expanssion coefficients in Eqs. (B.37)-(B.39) are given here:

$$\begin{aligned}a_{\mu\nu}^{x}=\frac{-k}{2\left(\nu+1\right)}\quad&\left\{\frac{\nu+1}{\nu\left(2\nu-1\right)}\left[a\left(m,n\left|\mu-1,\nu-1\right.\right)\right.\right.\\&\qquad\left.-\left(\nu-\mu\right)\left(\nu-\mu-1\right)a\left(m,n\left|\mu+1,\nu-1\right.\right)\right]\\&+\frac{1}{2\nu+3}\left[\left(\nu+\mu+2\right)\left(\nu+\mu+1\right)a\left(m,n\left|\mu+1,\nu+1\right.\right)\right.\\&\qquad\left.\left.-a\left(m,n\left|\mu-1,\nu+1\right.\right)\right]\right\}\end{aligned}\tag{B.40}$$

$$b_{\mu\nu}^{x}\left(\mathbf{r}_0\right)=\frac{ik}{2\nu\left(\nu+1\right)}\left[\left(\nu-\mu\right)\left(\nu+\mu+1\right)a\left(m,n,\mu+1,\nu\right)+a\left(m,n,\mu-1,\nu\right)\right],\tag{B.41}$$

$$\begin{aligned}a_{\mu\nu}^{y}\left(\mathbf{r}_0\right)=\frac{ik}{2\left(\nu+1\right)}\quad&\left\{\frac{\nu+1}{\nu\left(2\nu-1\right)}\left[a\left(m,n\left|\mu-1,\nu-1\right.\right)\right.\right.\\&\qquad\left.+\left(\nu-\mu\right)\left(\nu-\mu-1\right)a\left(m,n\left|\mu+1,\nu-1\right.\right)\right]\\&-\frac{1}{2\nu+3}\left[\left(\nu+\mu+2\right)\left(\nu+\mu+1\right)a\left(m,n\left|\mu+1,\nu+1\right.\right)\right.\\&\qquad\left.\left.+a\left(m,n\left|\mu-1,\nu+1\right.\right)\right]\right\}\end{aligned}\tag{B.42}$$

$$b_{\mu\nu}^{y}\left(\mathbf{r}_0\right)=\frac{-k}{2\nu\left(\nu+1\right)}\left[\left(\nu-\mu\right)\left(\nu+\mu+1\right)a\left(m,n\left|\mu+1,\nu\right.\right)-a\left(m,n\left|\mu-1,\nu\right.\right)\right],\tag{B.43}$$

$$a_{\mu\nu}^{z}\left(\mathbf{r}_0\right)=\frac{k}{\nu\left(\nu+1\right)}\left[\frac{\left(\nu+1\right)\left(\nu-\mu\right)}{2\nu-1}a\left(m,n\left|\mu,\nu-1\right.\right)+\frac{\nu\left(\nu+\mu+1\right)}{2\nu+3}a\left(m,n\left|\mu,\nu+1\right.\right)\right], \tag{B.44}$$

$$b_{\mu\nu}^{z}\left(\mathbf{r}_0\right)=\frac{ik\mu}{\nu\left(\nu+1\right)}a\left(m,n\left|\mu,\nu\right.\right). \tag{B.45}$$

In addition, we have

$$\mathbf{M'}_{00}\left(\mathbf{r'}\right)=0, \tag{B.46}$$

$$\mathbf{N'}_{00}\left(\mathbf{r'}\right)=0. \tag{B.47}$$

It should be highlighted that the expansion coefficient $b_{\mu\nu}^{x}$ given in [80] is correct, while the expansion coefficient $a_{\mu\nu}^{x}$ given in [80] is incorrect. The expansion coefficient $a_{\mu\nu}^{x}\left(\mathbf{r}_0\right)$ given in [80] is

$$\begin{aligned}a'_{\mu\nu}=\frac{\nu}{2\nu\left(\nu+1\right)}&\left\{\frac{\nu+1}{2\nu-1}\left[A\left(\mu-1,\nu-1\right)-\left(\nu-\mu\right)\left(\nu-\mu-1\right)A\left(\mu+1,\nu-1\right)\right]\right.\\&\left.+\frac{\nu}{2\nu+3}\left[\left(\nu+\mu+2\right)\left(\nu+\mu+1\right)A\left(\mu+1,\nu+1\right)-A\left(\mu-1,\nu+1\right)\right]\right\}.\end{aligned} \tag{B.48}$$

B.2.2 Vector Spherical Wave Functions Translational Addition Theorems

Substitute Eqs. (B.36)-(B.39) into Eq. (B.34), we have

$$\mathbf{M}_{mn}\left(\mathbf{r}\right)=\sum_{\nu=1}^{\infty}\sum_{\mu=-\nu}^{\nu}A_{\mu\nu}^{mn}\left(\mathbf{r}_0\right)Rg\mathbf{M'}_{\mu\nu}\left(\mathbf{r'}\right)+B_{\mu\nu}^{mn}\left(\mathbf{r}_0\right)Rg\mathbf{N'}_{\mu\nu}\left(\mathbf{r'}\right), \tag{B.49}$$

where

$$A_{\mu\nu}^{mn}\left(\mathbf{r}_0\right)=A_{\mu\nu}\left(\mathbf{r}_0\right)+a\left(m,n\left|\mu,\nu\right.\right), \tag{B.50}$$

$$B_{\mu\nu}^{mn}\left(\mathbf{r}_0\right)=B_{\mu\nu}\left(\mathbf{r}_0\right), \tag{B.51}$$

$$A_{\mu\nu}\left(\mathbf{r}_0\right)=r_0\sin\theta_0\cos\phi_0 a_{\mu\nu}^{x}\left(\mathbf{r}_0\right)+r_0\sin\theta_0\sin\phi_0 a_{\mu\nu}^{y}\left(\mathbf{r}_0\right)+r_0\cos\theta_0 a_{\mu\nu}^{z}\left(\mathbf{r}_0\right), \tag{B.52}$$

$$B_{\mu\nu}=r_0\sin\theta_0\cos\phi_0 b_{\mu\nu}^{x}\left(\mathbf{r}_0\right)+r_0\sin\theta_0\sin\phi_0 b_{\mu\nu}^{y}\left(\mathbf{r}_0\right)+r_0\cos\theta_0 b_{\mu\nu}^{z}\left(\mathbf{r}_0\right), \tag{B.53}$$

Using Eq. (A.3), we have

$$\mathbf{N}_{mn}\left(\mathbf{r}\right)=\sum_{\nu=1}^{\infty}\sum_{\mu=-\nu}^{\nu}A_{\mu\nu}^{mn}\left(\mathbf{r}_0\right)Rg\mathbf{N'}_{\mu\nu}\left(\mathbf{r'}\right)+B_{\mu\nu}^{mn}\left(\mathbf{r}_0\right)Rg\mathbf{M'}_{\mu\nu}\left(\mathbf{r'}\right). \tag{B.54}$$

The vector spherical wave functions translational addition theorem for $r' > r_0$ can be written as

$$\mathbf{M}_{mn}\left(\mathbf{r}\right)=\sum_{\nu=1}^{\infty}\sum_{\mu=-\nu}^{\nu}RgA_{\mu\nu}^{mn}\left(\mathbf{r}_0\right)\mathbf{M'}_{\mu\nu}\left(\mathbf{r'}\right)+RgB_{\mu\nu}^{mn}\left(\mathbf{r}_0\right)\mathbf{N'}_{\mu\nu}\left(\mathbf{r'}\right), \tag{B.55}$$

$$\mathbf{N}_{mn}\left(\mathbf{r}\right)=\sum_{\nu=1}^{\infty}\sum_{\mu=-\nu}^{\nu}RgA_{\mu\nu}^{mn}\left(\mathbf{r}_0\right)\mathbf{N'}_{\mu\nu}\left(\mathbf{r'}\right)+RgB_{\mu\nu}^{mn}\left(\mathbf{r}_0\right)\mathbf{M'}_{\mu\nu}\left(\mathbf{r'}\right). \tag{B.56}$$

The original scalar spherical wave functions translational addition theorems, the extended scalar spherical wave functions translational addition theorems, and the vector spherical wave functions translational addition theorems have been numerically validated. It is observed that the extended scalar wave functions translational addition theorems are numerically unstable.

The vector spherical wave functions translational addition theorems have been applied to solve the electromagnetic scattering of multiple scatterers using the T-matrix method. Numerical results show good agreement with the results obtained using the method of moment. It therefore further confirms the correction to vector spherical wave functions translational addition theorems, and demonstrates the potential applications of the vector spherical wave functions translational addition theorems in solving multiple scattering problems rigorously.

Appendix C

Rotational Addition Theorems

C.1 The Euler Angles

The general displacement of a rigid body due to a rotation about a fixed point may be obtained by performing three rotations about two of three mutually perpendicular axes fixed in the body. Several conventions exist to define these three angles. Here we follow that used by Edmonds [89]. Any rotation about a given axis in the direction following the right-handed rule is defined as positive rotation. The three Euler angles (α, β, γ) are defined as follows:

1. The first rotation is by an angle α about the z-axis as shown in Fig. C-1. x-and y-axis are moved to ξ-and η-axis.

2. The second rotation is by an angle β about the y-axis as shown in Fig. C-2. For this time, ξ-and z-axis are moved to ξ'-and z'-axis.

3. The third rotation is by an angle γ about the z-axis, again, as shown in Fig. C-3. ξ'-and η-axis are moved to x'-and y'-axis.

As a result, the (x, y, z) axis are rotated to (x', y', z') axis.

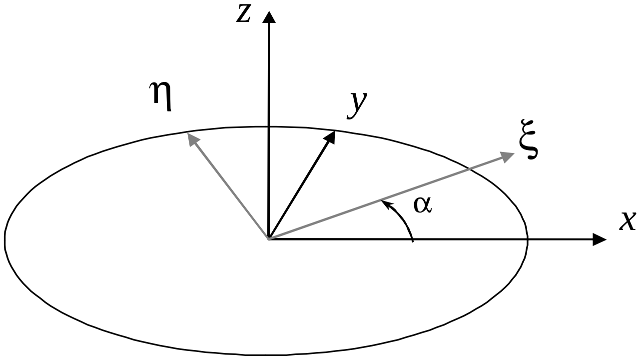

Figure C-1: Euler angle α.

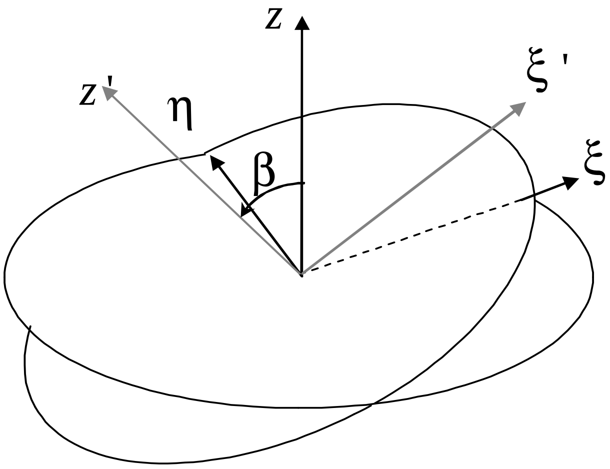

Figure C-2: Euler angle β.

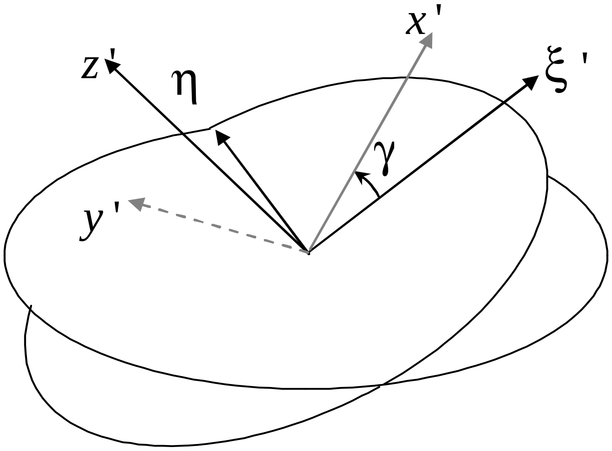

Figure C-3: Euler angle γ.

C.2 Spherical Harmonics Rotational Addition Theorems

The coordinates rotation defined by Euler angles (α, β, γ), the addition theorems for spherical harmonics is [89, 103, 105]

$$Y_{m'n}\left(\theta', \phi'\right) = \sum_{m=-n}^{n} D_{mm'}^{(n)}\left(\alpha\beta\gamma\right) Y_{mn}\left(\theta, \phi\right), \tag{C.1}$$

where [49, 89, 105]

$$Y_{mn}\left(\theta, \phi\right) = \sqrt{\frac{2n+1}{4\pi}\frac{(n-m)!}{(n+m)!}} P_n^m\left(\cos\theta\right) e^{jm\phi}. \tag{C.2}$$

$D_{mm'}^{(n)}\left(\alpha\beta\gamma\right)$is the Wigner D-functions [8, 89, 103, 105] given by

$$D_{mm'}^{(n)}\left(\alpha\beta\gamma\right) = e^{jm\alpha} d_{mm'}^{(n)}\left(\beta\right) e^{jm'\gamma}, \tag{C.3}$$

where

$$\begin{aligned} d_{m'm}^{(n)}(\beta) = & \sqrt{\frac{(n+m')!}{(n+m)!}\frac{(n-m')!}{(n-m)!}} \sum_{\sigma} \begin{pmatrix} n+m \\ n-m'-\sigma \end{pmatrix} \begin{pmatrix} n-m \\ \sigma \end{pmatrix} \\ & \times (-1)^{n-m'-\sigma} \left(\cos\frac{\beta}{2}\right)^{2\sigma+m'+m} \left(\sin\frac{\beta}{2}\right)^{2n-2\sigma-m'-m} \end{aligned} . \quad \text{(C.4)}$$

It can be alternatively written as [89, 103]

$$\begin{aligned} d_{m'm}^{(n)}(\beta) = & \sqrt{\frac{(n+m')!}{(n+m)!}\frac{(n-m')!}{(n-m)!}} \left(\cos\frac{\beta}{2}\right)^{m'+m} \left(\sin\frac{\beta}{2}\right)^{m'-m} \\ & \times P_{n-m'}^{(m'-m,m'-m)}(\cos\beta) \end{aligned} , \quad \text{(C.5)}$$

where $P_n^{(\alpha,\beta)}$ is the Jacobi polynomial which can be expressed in terms of associated Legendre polynomials [103],

From Eq. (C.1), we have

$$Y_{mn}(\theta,\phi) = \sum_{m'=-n}^{n} D_{m'm}^{(n)}(\,-\gamma - \beta - \alpha)\, Y_{m'n}(\theta',\phi'). \quad \text{(C.6)}$$

From Eq. (C.3), we have

$$D_{m'm}^{(n)}(-\gamma - \beta - \alpha) = e^{-jm'\gamma} d_{m'm}^{(n)}(-\beta)\, e^{-jm\alpha}. \quad \text{(C.7)}$$

It is shown in [89] that

$$d_{m'm}^{(n)}(\,-\beta) = d_{mm'}^{(n)}(\beta)\,. \quad \text{(C.8)}$$

Therefore,

$$\begin{aligned} D_{m'm}^{(n)}(-\gamma - \beta - \alpha) = e^{-jm'\gamma} d_{m'm}^{(n)}(-\beta)\, e^{-jm\alpha} = e^{-jm'\gamma} d_{mm'}^{(n)}(\beta)\, e^{-jm\alpha} \\ = \left[e^{jm\alpha} d_{mm'}^{(n)}(\beta)\, e^{jm'\gamma}\right]^{*} = \left[D_{mm'}^{(n)}(\alpha\beta\gamma)\right]^{*} \end{aligned} . \quad \text{(C.9)}$$

Accordingly,

$$Y_{mn}(\theta,\phi) = \sum_{m'=-n}^{n} \left[D_{mm'}^{(n)}(\alpha\beta\gamma) \right]^{*} Y_{m'n}(\theta',\phi'). \tag{C.10}$$

C.3 Scalar and Vector Spherical Wave Functions Rotational Addition Theorems

The modified scalar spherical wave function is

$$\begin{aligned} \bar{\psi}_{mn}(\mathbf{r}) &= z_n(kr)\, Y_{mn}(\theta,\phi) && \text{(C.11)} \\ &= \sqrt{\frac{2n+1}{4\pi}\frac{(n-m)!}{(n+m)!}}\psi_{mn}(\mathbf{r}) && \text{(C.12)} \\ &= \lambda_{mn}\psi_{mn}(\mathbf{r}), && \text{(C.13)} \end{aligned}$$

where $\psi_{mn}(\mathbf{r})$ is the scalar spherical wave function. From Eqs. (C.2), (C.10) and (C.11), we have

$$\bar{\psi}_{mn}(\mathbf{r}) = \sum_{m'=-n}^{n} \left[D_{mm'}^{(n)}(\alpha\beta\gamma) \right]^{*} \bar{\psi}_{m'n}(\mathbf{r}'), \tag{C.14}$$

where the superscript asterisk means complex conjugate.

The vector spherical wave functions and the modified vector spherical wave functions are defined as

$$\mathbf{M}_{mn}(\mathbf{r}) = \nabla \times [\mathbf{r}\psi_{mn}(\mathbf{r})], \tag{C.15}$$

$$\mathbf{N}_{mn}(\mathbf{r}) = \frac{1}{k}\nabla \times \mathbf{M}_{mn}(\mathbf{r}), \tag{C.16}$$

$$\bar{\mathbf{M}}_{mn}(\mathbf{r}) = \nabla \times \left[\mathbf{r}\bar{\psi}_{mn}(\mathbf{r})\right] = \lambda_{mn}\mathbf{M}_{mn}(\mathbf{r}), \tag{C.17}$$

$$\bar{\mathbf{N}}_{mn}\left(\mathbf{r}\right) = \frac{1}{k}\nabla \times \bar{\mathbf{M}}_{mn}\left(\mathbf{r}\right) = \lambda_{mn}\mathbf{N}_{mn}\left(\mathbf{r}\right). \tag{C.18}$$

Accordingly,

$$\bar{\mathbf{M}}_{mn}\left(\mathbf{r}\right) = \sum_{m'=-n}^{n}\left[D_{mm'}^{(n)}\left(\alpha\beta\gamma\right)\right]^{*}\bar{\mathbf{M}}_{m'n}\left(\mathbf{r}'\right), \tag{C.19}$$

$$\bar{\mathbf{N}}_{mn}\left(\mathbf{r}\right) = \sum_{m'=-n}^{n}\left[D_{mm'}^{(n)}\left(\alpha\beta\gamma\right)\right]^{*}\bar{\mathbf{N}}_{m'n}\left(\mathbf{r}'\right). \tag{C.20}$$